UNIVERSITY OF BASEL

MASTER THESIS

Edge passivation of vicinal surfaces for controlled growth and substrate transfer of graphene nanoribbons

Author:
Dominik LÜTHI

Assessors:
Prof. Dr. Thomas JUNG,
Prof. Dr. Roman FASEL

Supervisors:
Dr. Gabriela BORIN BARIN,
Rimah DARAWISH

A thesis submitted in fulfillment of the requirements for the degree of Master of Nanosciences

in the

Nanotech@surfaces lab
Swiss Federal Laboratories for Materials Science and Technology EMPA

December 19, 2021

UNIVERSITY OF BASEL

Abstract

Swiss Federal Laboratories for Materials Science and Technology EMPA
Nanotech@surfaces lab

Master of Nanosciences

Edge passivation of vicinal surfaces for controlled growth and substrate transfer of graphene nanoribbons

by Dominik LÜTHI

Atomically-precise graphene nanoribbons (GNRs) have gained increasing interest over the recent years due to their tuneable band gap dependent on the width of the GNRs. With the aim to integrate 9-armchair graphene nanoribbons (9-AGNRs) grown at low density on Au(788) into switching devices, it is required to transfer them from the catalytic gold surface to the insulating device substrate, generally leading to a low device yield and defects within the GNRs.
In this work, the growth of Poly(para-phenylene) (PPP) on Au(788) is studied with scanning tunneling microscopy (STM) and Raman spectroscopy, showing a promising potential for edge-passivation on vicinal surfaces due to its preferential growth along the Au(788) step-edges. Our study shows that it is possible to grow 9-AGNRs on Au(788) edge-passivated with PPP by gradual deposition and growth of the precursors. Investigating the growth statistics of low surface coverage 9-AGNRs grown on both PPP-passivated and unpassivated surfaces, we observe that the presence of PPP promotes the growth of GNRs away from the step-edge with an increased average length. Preliminary investigations on the transfer of these samples point towards increased alignment for 9-AGNRs grown together with PPP, even though the observed broadening in the Raman spectra point towards non-uniform transfer. Optimization of the edge-passivation process on vicinal surfaces could be the gateway to achieve improved transfer of highly aligned 9-AGNRs grown at low density, ultimately leading to an enhancement in the performance of GNR-based devices.

Acknowledgements

Throughout the thesis I was provided a lot of help and assistance to improve both my work in the lab and my writing.

First and foremost, I am profoundly grateful to have had the possibility to work with my supervisors Dr. Gabriela Borin Barin and Rimah Darawish, who did not hesitate to help me if needed with great effort and commitment. Furthermore, I would like to thank Prof. Roman Fasel for the opportunity to join his lab for this thesis, allowing me to gain insight into an exciting field of research, and the support I was given. I also would like to thank Prof. Thomas Jung for the regular inputs towards the advancement of my research and his engagement to assess my thesis. My sincere thanks also to Dr. Pascal Ruffieux, who aided by giving feedback to the progress of the thesis to guide us in the right direction.
Last but not least, I am grateful for the entire research group Lab 205 of the EMPA because everyone gave me invaluable help without hesitation whenever problems in the lab were occurring.

Contents

List of Figures

Chapter 1

Introduction

1.1 Graphene and its properties

Over the last two decades, the discoveries of the outstanding properties of graphene generated huge interest towards its research and applications. The subsequent advancements in science and technology lead to the pioneers of the field, Andre Geim and Konstantin Novoselov, winning the Nobel Prize in physics for their exceptional research. [1]
Graphene consists of an extended sp^2-system of carbon atoms first synthesized and characterized in 2004. [2] Due to the confinement of electrons within the resulting planar sheet of graphene, its dimensionality reduces to 2D, yielding exciting electronic properties. [3] Graphene is a transparent conductor [4] with extraordinarily high thermal and electrical conductivity. On this basis, graphene represents a promising material for implementations in technology. [5] Moreover, the strechability and ultimate tensile strength (considerably stronger than steel) make it an exciting material for applications in the construction industry. [6, 7, 8]
Graphene is closely related to the most abundant form of carbon, graphite, consisting of stacked sheets of graphene. Even though the isolation of a single sheet of graphene was thought to be impossible initially, eventually the isolation of a single sheet was achieved by the mechanical exfoliation of graphite which in turn allowed the investigation of graphene's electrical properties. [9] The electronic structure of graphene is very distinct from three-dimensional materials. The 2D hexagonal periodic lattice modifies the band structure such that the Fermi surface is characterized by six double cones as seen in Figure 1.1. [10]
In graphene, it is considered that 2s orbital and two 2p orbitals of each carbon atom are hybridized to form an s-band filled by 3/4 of valence electrons of the carbon

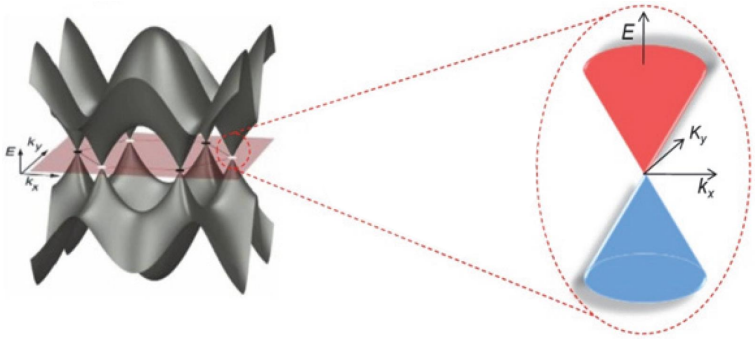

FIGURE 1.1: Energy dispersion relations of graphene. Inset shows the energy dispersion relations along the high symmetry axes near the Dirac point. [10]

atoms. The remaining valence electrons fill the orthogonal p_z orbitals. Thus, the occupied electronic states with the highest energy (Fermi energy) in graphene are thus well described by the p_z orbitals interacting with each other in the honeycomb lattice. [11] The energy of the π-band E of graphene is obtained by the diagonalization of the Hamiltonian of the system $\hat{H}$.

$$\hat{H} = \begin{pmatrix} 0 & H^*(\overrightarrow{k}) \\ H(\overrightarrow{k}) & 0 \end{pmatrix} \tag{1.1}$$

where $H(\overrightarrow{k}) = -\gamma_0 g(\overrightarrow{k})$. γ_0 is a resonance integral representing the electronic interaction between nearest neighbor carbon atoms in graphene and $g(\overrightarrow{k})$ is a resonance integral depending on the lattice potential of graphene, the atomic potential of a carbon atom and the location of the electrons. [11] One obtains for the energy of the π-band:

$$E_{C,V}(\overrightarrow{k}) = \pm\gamma_0 |g(\overrightarrow{k})| \tag{1.2}$$

determining the energy of the conduction and valance band by the change in the sign. [11, 12]
Figure 1.1 shows a three-dimensional plot of the π-band energies. As highlighted in the figure, there are 6 points in the unit cell where the valence and conduction band meet. This point is denoted the *Dirac point*. Consequently, graphene is called a *zero gap* semiconductor.
In addition, the dispersion relation for electrons and holes is linear around the Dirac point. Since the effective masses are given by the curvature of the energy bands, this corresponds to zero effective mass. [13]

1.2 Graphene nanoribbons (GNRs) and its properties

Although the high carrier mobility of graphene makes it a promising material for electronic applications, the absence of a band gap impedes its use for switching applications such as field effect transistors (FETs) . [14, 15] Thus, modifications of graphene towards opening a band gap have achieved increasing attention.
The presence of the band gap permits devices to operate at higher temperature, voltages and frequencies. In respect to the integration in transistors, an increase in the band gap allows for a more powerful and energy-efficient performance. [16]
Graphene nanoribbons (GNRs) are thin strips of graphene. Due to the lateral termination of the periodic lattice, the increased confinement results in a quasi one dimensional ribbon like structure. [17] Electron-electron (e-e) interactions play a dominant role in GNRs due to their quasi-1D nature and the weak screening, giving rise to an energy gap. [18]
To visualize the origin of the band gap, we refer to the Fermi energy as a linear dispersion relation around the Dirac point as follows

$$E = \hbar v_F k \tag{1.3}$$

with v_F the Fermi velocity and k the wave vector. If we assume the GNR in the xy-plane with the long axis oriented along x, k is discretized in y due to the confinement, where

$$k_y = \frac{n\pi}{w} \quad n = \pm 1, \pm 2, ... \tag{1.4}$$

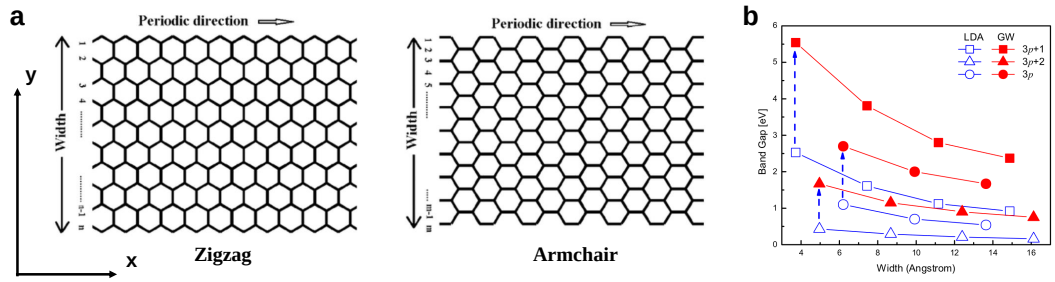

FIGURE 1.2: **a** Distinct edge structures of GNRs. Left: structure of zigzag GNRs (ZGNRs). Right: structure of armchair GNRs (AGNRs) [20] **b**: Variation of the band gap of GNR as a function of the width obtained from first-principles Green's function calculation within the *GW* approximation. [22]

with w the width of the ribbon.
Therefore, using the relation $k = \sqrt{{k_x}^2 + {k_y}^2}$, we obtain the dispersion relation of GNRs described as

$$E = \pm\hbar v_F \sqrt{{k_x}^2 + \frac{n\pi^2}{w}} \,. \tag{1.5}$$

and consequently a band gap $E_g = \frac{2\pi\hbar v_F}{w}$ is obtained due to the lateral confinement. [19]

GNRs occur in two possible edge geometries (see Figure 1.2 **a**), zigzag GNRs (ZGNRs) and armchair GNRs (AGNRs), yielding very different electronic properties arising from the altering boundary conditions. [20, 21].
The width dependence of the GNRs with respect to the band gap however is more complicated than described in equation 1.5. More precisely for AGNRs, the band gap scales inversely with the ribbon width. AGNRs of the groups of $N = 3p + 1$ (n is an integer) and $N = 3p$ (N here is the width of a particular AGNR) are predicted to have a stronger dependence on the width than AGNRs of the group of $N = 3p + 2$. [22, 23] According to Figure 1.2 **b**, we see that the order of the band gap energies follow $\Delta 3p + 1 > \Delta 3p > \Delta 3p + 2$. Moreover, in the case of $N = 3p$ and $3p + 2$ AGNRs, both HOMO and LUMO show orbital delocalizations along the ribbon length. Therefore, the band gap changes significantly with increase in ribbon length. [24, 25]

On the other hand, charge-carrier mobilities of AGNRs are predicted to decrease with the increasing band gap and thus the width has to be fine-tuned accordingly to achieve an optimal trade-off between the mobility and band gap for the targeted applications. [26]
Moreover, since the electronic properties of GNRs are strongly reliant on the edge geometries, defects can dramatically affect the electronic features of the ribbons. [23, 27]

1.3 Fabrication of graphene nanoribbons (GNRs)

1.3.1 Top-down approaches to the synthesis of GNRs

The synthesis of GNRs from graphene was first investigated based on top-down methods.

A popular method for the production of GNRs potentially scalable is *e-beam lithography* (EBL), where GNRs are lithographically patterned out of graphene (see Figure 1.3 **a**). [28] Different kinds of lithographic methods are known such as helium ion beam lithography, [29] meniscus mask lithography, [30] block copolymer lithography, [31] graphene edge lithography, [32] and scanning tunneling microscopy (STM) lithography. [33] In general, lithographic patterning lacks atomic resolution, inducing edge disorder, dangling bonds and results in high line-edge roughness.
A second approach is the top-down cutting of graphene, graphite or carbon nanotubes (CNTs). Figure 1.3 **b** depicts the synthesis of GNRs directly from cutting graphene catalyzed by nanoparticles. [34] Other methods incorporate the sonochemical unzipping of graphite [35] or the synthesis of GNRs out of CNTs by solution- or plasma-mediated unzipping, as shown in Figure 1.3 **c**. [36]
Among the disadvantages of these approaches are the lack of control over the width, decreased alignment due to the uncertainty of the trajectory along which the nanoparticles etch. [28]

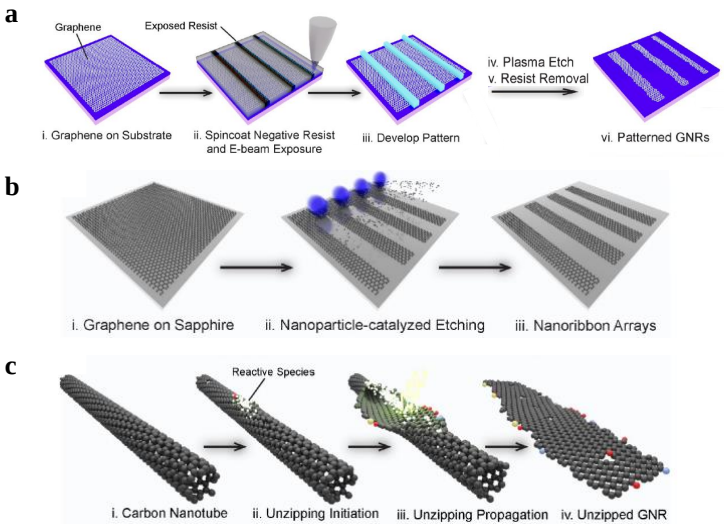

FIGURE 1.3: GNR fabrication via top-down nanocutting techniques. **a** Overview of the main steps to produce GNRs by electron-beam lithography. **b** Creation of GNR arrays using nanoparticle-catalyzed etching of graphene. **c** Scheme of unzipping CNTs to produce GNRs. Unzipping can be initiated by catalytic nanoparticles, oxidizing agents, or plasma. [28]

1.3.2 Bottom-up approaches to the synthesis of GNRs

To reliably use GNRs for applications, it is necessary to have the ability to tailor the edge geometry and width of the ribbons precisely. It is therefore often advantageous to perform a bottom-up synthesis, starting from a precursor polymerizing on a surface. In this respect, solution-mediated or surface-assisted synthesis of GNRs has gained significant attention in recent times.

Solution-mediated polymerization is a fairly accessible tool to synthesize ribbons reaching lengths over 500 nm [37] and enabling the uniform deposition of GNR films. [38] However, due to the agglomeration of GNRs occurring during the synthesis,

isolation of the GNRs is a strenuous task. [39] A recent discovery to overcome this problem is the incorporation of functional groups at the edges of the GNRs. Since this edge alteration significantly influences the electronic properties of the GNR, it is questionable whether these GNRs can be used without compromises in performance. [40] In addition, while a reversible attachment of functional groups at the edges could be exploited to retrieve the unfunctionalized ribbon after isolation, these functional groups are difficult to remove, further hindering this strategy.

Atomically-precise synthesis of GNRs catalyzed by surfaces is the pioneering method to achieve selective GNRs. [41] This method exploits the surface-assisted synthesis of GNRs from a particular precursor. Thus, the structure of the molecular precursor precisely defines the width and edge structure of the synthesized GNRs, allowing for an unmatched control of their synthesis. The high reliability and precision of this method opens up possibilities in terms of synthesis of materials with novel electronic properties by a smart choice of precursors. [43] A common property of all precursors are the halogenated ends on both sidse of the precursor, which are essential for the polymerization. The problem of the GNR synthesis essentially breaks down to an organochemical challenge tailoring the monomer unit as desired. Additionally, this method allows exact control over possible heteroatoms within the GNR by design of the precursor. [44, 45, 46] However, an upper limit for the size of the precursors exists, since the molecule has to evaporate upon annealing of the crucible as opposed to decomposition on the surface. [42]

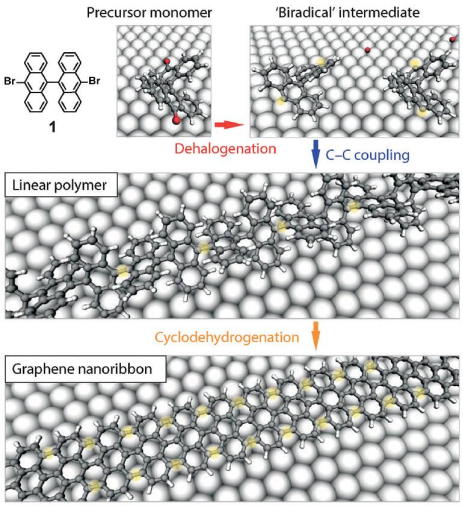

FIGURE 1.4: On-surface synthesis of N = 7 armchair graphene nanoribbons (7-AGNRs). Synthesis steps including surface-assisted dehalogenation of DBBA monomers, polymer growth by radical addition at temperature T_1, and surface-assisted cyclodehydrogenation at temperature $T_2 > T_1$ [41, 42]

The polymerization is induced by a dehalogenation catalyzed by the metal surface. The temperature for dehalogenation of the precursor is determined by an interplay of the used metal substrate [47] and the attached halogen [42, 48]. As an example, on Au(111) no dehalogenation of the carbon-bromine occurs at room temperature [49], while Cu(111) shows bond cleavage under these conditions. [50] Additionally, due to the difference in bonding strength, the halogens of the precursor cleave at higher temperatures with decreasing size of the ion ($T_{1_I} < T_{1_{Br}}$). [47, 48]

To optimize the length of the resulting GNRs, the substrate and the precursor has to be adjusted such that the dehalogenation temperature T_1 is in a desirable range. At T_1 the precursors are fully dehalogenated and diffuse freely on the surface while remaining bound to the surface. Once two of these radicals share the same metal atom as bonding partner, the coupling of radicals is found to be practically free of barriers and they polymerize. [51, 52]

Initially, the length increases dramatically with the annealing temperature. However, the yield of GNR does not linearly increase. At a certain temperature (specific to the precursor) the length decreases, pointing towards a competitive reaction occurring on the surface, inducing the premature termination of the ribbons. It is assumed to originate from the cyclodehydrogenation starting at around 200 $^{\circ}C$. [53]

As a result, spare hydrogen diffusing on the surface might passivate the precursors, prohibiting further polymerization of these moieties. [54]
Increase in temperature to the cyclodehydrogenation temperature T_2 induces dehydrogenation of the polymerized precursors. [41] Similarly to T_1, T_2 depends on the choice of substrate and the chosen precursor. [52, 55] On Au(111) the dehydrogenation temperature usually is around 400 $°C$, while it is lower on Cu(111). [53, 56] To increase the average length of the synthesized ribbons, it is of central importance that T_1 and T_2 are well separated such that the polymerization of the precursors is not prematurely terminated. [42, 54] The interplay between all these factors shows that the optimization of surface-assisted GNR growth is a complex task.

1.4 Characterization techniques of graphene nanoribbons (GNRs)

A multitude of characterization techniques aid to study GNRs both in-situ and ex-situ. The methods used for this thesis are scanning tunneling microscopy (STM) for characterization of the GNRs synthesized in ultra-high vacuum (UHV) and Raman spectroscopy for the characterization of GNRs on both conducting and insulating substrates. In the following, we will first lay out a theoretical description of the employed methods, following by specific examples on the study of GNRs.

1.4.1 Theoretical aspects of the instrumental methods

Scanning tunneling microscopy

The invention of scanning probe microscopy (SPM) [57] lead to outstanding progress in a variety of fields from biology, medicine, engineering to physics and chemistry. SPM enables characterization and manipulation on the atomic scale through near-field interactions between the investigated sample and the tip of the microscope.
Especially today, with the increasing interest in the development of devices spanning over just a few nanometers, SPM is an indispensable tool for a thorough characterization of their properties. Allowing for an atomically precise mapping of solid surfaces in UHV, SPM can be used to examine the behaviour of molecular structures and thus may facilitate to monitor for example on-surface chemical reactions, which further improves the understanding of molecular orbitals and bonding.
The pioneering instrument in this regard was the scanning tunneling microscope (STM), invented in 1982 by G. Binnig and H. Rohrer. [58] An STM incorporates a tip, which rasters the surface in a nanometer-sized square. The distance of the tip to the surface is controlled over the tunneling current, which is a quantum mechanical effect arising due to ability of particles to diffuse through a potential too steep to climb classically. In the case of the STM, this potential is induced by the vacuum gap between the tip and the sample. Hence, the tunneling current flows from the very last atom of the tip apex to single atoms at the surface, providing atomic resolution. [59]
The tunneling current is described as

$$I(d) = eV \cdot exp(-2\frac{\sqrt{2m\Phi}}{\hbar}d) \tag{1.6}$$

where Φ is the work function of the metal, V is the applied voltage, e the elementary charge, m the electron mass, $\hbar$ the reduced Planck's constant and d the tip-sample distance. [60] This exponential dependence of the tunneling current in regard to the

tip-sample distance is the origin of the high sensitivity in STM towards imaging of single atoms. The experimental setup of an STM will further be discussed in Section 2.1.1.
Even though STM provides a detailed understanding of investigated surface, it is a very local measurement. It is therefore beneficial to combine it with characterization methods that provide a more global picture of the sample. Moreover, a method is required that supplements the STM for measurements on insulating surfaces, which are inaccessible for STM. In this case, Raman spectroscopy can especially be helpful.

Raman spectroscopy

Raman spectroscopy is an optical characterization method to detect vibrations in atoms or molecules, providing information on chemical structures. [61] It is named after one of its discoverers, C. V. Raman, who together with K. S. Krishnan observed a "new type of radiation" in 1928 [61, 62]. Raman's discovery was awarded the Nobel Prize in Physics in 1930. [63] In a Raman spectrometer, a sample is irradiated with a single wavelength light. When the photons of the light ray interact with the sample, they either get absorbed or scattered. Each photon carries an energy

$$E = hf = \frac{hc}{\lambda} \tag{1.7}$$

with h is Planck's constant, c is the speed of light and λ the wavelength.
When interacting with the sample, the electron cloud of the nuclei of get distorted to form a short-lived *virtual state*. Accompanied with the relaxation of the molecule back to the ground state, the photon re-emitted and might be directed towards the detector. [64] If nuclear motion (i.e. vibrations) is induced during this scattering process, energy will be transferred either from the incident photon to the molecule or from the molecule to the scattered photon. This represents an inelastic scattering process, causing the energy of the re-emitted photon to differ by one vibrational quantum (phonon), generally referred to as *Raman scattering* [1]. [65]

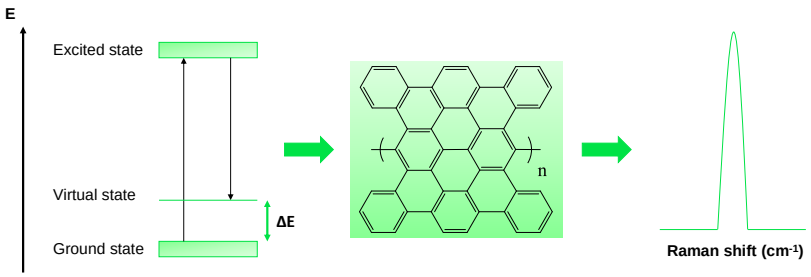

FIGURE 1.5: Principle of Raman spectroscopy. A light ray leads to excitation, followed by a decay to a virtual state. The energy difference between the two states is established as a Raman shift. (Figure adapted from [66])

Raman scattering only is detectable for vibrations which cause a change in the polarizability of the electron cloud, mostly through symmetric vibrations. The characteristic energy shifts for certain vibrations can be derived from a classical system, where two neighbouring atoms bonded together in analogy to a "ball and spring" model.

[1] Details on the origin of this scattering process are discussed in the Appendix (Section A.1.1)

While the spring represents the bonds between the atoms, the balls represent the atoms. The stronger the bonds are, the higher the frequency of vibration and the heavier the atoms are, the lower the frequency of vibration. Thus, the frequency of vibration obeys Hooke's law

$$\nu = \frac{1}{2\pi c}\sqrt{\frac{K}{\mu}} \ . \tag{1.8}$$

Here, ν is the frequency of vibration, c is the speed of light, K is the force constant of the bond between two neighbouring atoms and μ the reduced mass. [64, 67] The characteristic vibrations are mainly reflected through these specific combinations of bond strength K and the masses of the atoms involved in the vibrations. Since every bond has a specific frequency of vibration, backbones of molecules can be easily determined with Raman spectroscopy.

1.4.2 Characterization of GNRs

A variety of techniques are used to characterize the GNRs. Generally, multiple methods (transmission electron microscopy (TEM) [68, 69], scanning tunneling microscopy (STM) [58], ultraviolet–visible spectroscopy (UV-VIS) [70], Raman spectroscopy [62]) can be employed to get a profound assessment of the length and possible defects within the GNR lattice. Other methods are used to determine more fundamental physical properties of the GNRs (angle-resolved photoemission spectroscopy (ARPES), scanning tunneling spectroscopy (STS)).
Figure 1.6 **a** and **b** depict the scanning tunneling microscopy (STM) and non-contact atomic force microscopy (nc-AFM) images of 9-AGNRs synthesized with on-surface synthesis starting from the precursor 3,6-dibromo-1,1:2,1- terphenyl (DBTP). [43] While AFM manages to resolve individual phenyl rings within the framework of the 9-AGNRs, the STM image represents these ribbons as an extended band of finite width. Due to the delocalization of the electrons throughout the whole molecule, the STM can generally not highlight individual phenyl rings. However, defects such as a missing phenyl rings at the edges are easily recognizable (see Section 3.2.1). Studies on the height of the GNRs relative to the substrate revealed that they undergo a planarization after annealing over 350 $^{\circ}C$, inducing cyclodehydrogenation. Moreover, since radicals would form organometallic bonds with the surface [71], yielding a slight downward curvature towards the edges, the images show that these radicals get passivated with hydrogen. In-situ surface-sensitive characterization with STM allows to probe such chemical reactions and reaction steps by identifying the chemical bonds and structures formed on the substrate and provides an unmatched understanding of mechanisms on the molecular scale. [72]
Other methods such as scanning tunneling spectroscopy (STS) [73] or angle-resolved photoemission spectroscopy (ARPES) [74] are practical tools to gain insights into the electronic structure of molecules. ARPES measures the energies and emission angles of the electrons for 9-AGNRs parallely grown on a vicinal surface [21]. Figure 1.6 **c** shows the ARPES intensity plot as a function of energy (E - E_F) and k vector parallel to the ribbons. Consequently, the dispersion of the valance band (VB) of the GNRs is obtained along the axis of the GNRs. Since electron (or hole) energies can be approximated with a parabolic fit in k-space $E = E_0 \pm \frac{\hbar^2}{2m*}k^2$, the effective mass and VB maximum of the molecule can be determined unambiguously with ARPES. For 9-AGNRS the VB maximum as $E_0 = 0.25 \pm 0.04eV$ and an effective mass of $m^* = 0.09 \pm 0.02m_e$. [43]
STS allows to access occupied and unoccupied electronic states by measuring the

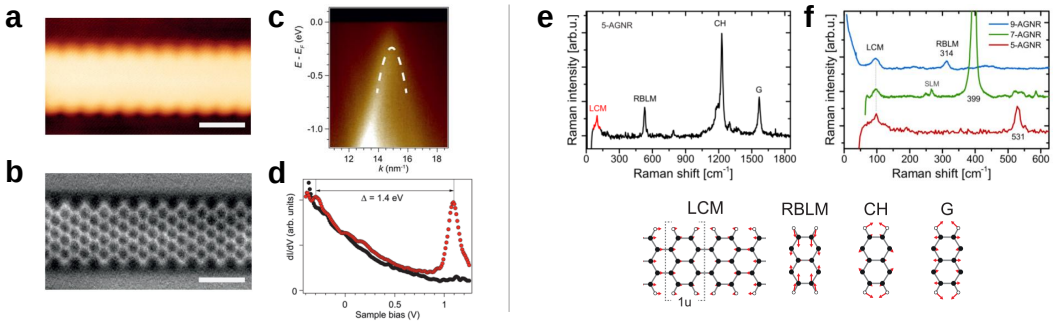

FIGURE 1.6: **a**: STM and **b**: nc-AFM topography of 9-AGNRs on Au(111). **c**: ARPES intensity plot as a function of energy (E – E_F) and k vector parallel to the ribbons. The dashed line represents the fit of the valence band around the maximum. **d**: dI/dV spectra recorded on the edge of a 9-AGNR (red) and on the Au(111) substrate (black). **e**: Raman spectrum of 5-AGNRs, highlighting the dominant modes. **f**: Low-energy Raman spectra of 5-, 7-, and 9-AGNRs indicating the dependence of the RBLM on the ribbon width. (adapted from [43], [76])

local density of electron states (which is a function of both position and energy). [75] Figure 1.6 **d** shows the STS spectrum for individual 9-AGNRs adsorbed on Au(111). Ribbon related peaks at +1.1 V (empty states) and 0.3 V (occupied states) were found, yielding a band gap of 1.4 eV for 9-AGNRs.

Raman spectroscopy is advantageous because of its ease of use and ability to measure on both conducting and insulating substrates. While measurements in-situ with SPM provide an excellent picture of the molecular structures locally, Raman spectroscopy succeeds in characterizing composites on the surface over a larger scale with a single spectrum, given the peak shifts are well-known for the investigated molecules.
A spectrum characteristic for graphene nanoribbons is depicted in Figure 1.6. Four peaks appear in the spectrum, namely the LCM, RBLM, C-H mode overlapping the D mode, and lastly the G mode [77]. These modes are named in analogy to the terminology used in graphite, graphene, and carbon nanotubes (CNTs). [78, 79] The G mode around 1590 cm^{-1} is present in all sp^2-based materials. [80] In the case of GNRs, it corresponds to an in-plane vibration of all carbon atoms within the framework. [81, 82] The symmetry of the G mode at edge points towards obvious polarization dependence. [83] Consequently, the intensity of the G mode is usually a useful measure when determining the polarization dependence to quantify the alignment of the ribbons (see Section 2.1.2). The C-H mode correlates strongly with the edge conformation of the GNRs, as it represents the bending modes of the H-passivated C atoms at the edges. [78, 80] The longitudinal vibrational radial breathing-like mode (RBLM) aids to determine the width of the GNR. [79, 84, 85] Due to its symmetry, a change in width of the structure directly correlates with a shift in its Raman peak. Therefore, since each GNR at a certain width has a unique shift in RBLM [86], the determination of the Raman shift of this mode allows to directly identify the GNR, as shown in Figure 1.6 **f**. Finally, the longitudinal compressive mode (LCM) corresponds to a vibration along the ribbon axis. Similarly to the RBLM, this mode can be

used to obtain direct information about the structure of the ribbon. Due to the symmetry properties of this mode, its Raman shift correlates directly with the length of the formed GNRs. [80]

1.5 Materials to devices

The gateway for atomically-precise synthesis of GNRs to attain exciting electronic properties leads to an increasing interest in the integration of these materials to devices. [87]
Building high-performance GNR-based devices not only requires atomically-precise synthesis, but also a reliable, high yield transfer to bridge the on-surface synthesis of the GNRs with the targeted electronic device.
Due to their robustness and ambient stability, armchair GNRs are so far the only class of GNRs that has been transferred and integrated into devices. 5-, 7- and 9-AGNRs were transferred using wet-transfer methods [80, 88] and integrated into devices with both metallic and graphene electrodes. 7-AGNRs integrated between two metallic contacts showed high Schottky barrier at the contacts, on-currents were found to be limited to tens of pA to a few nA due to the large bandgap of the 7-AGNR (2.3 eV measured on Au(111)) [87]. High performance transistors were achieved by Llinas et al. using 9-AGNRs as channel materials (bandgap of 1.4 eV measured on Au(111)), observing currents of up to 1 μA and I_{On}/I_{Off} ratios of 10^5 [89]. Even though high performance devices were fabricated using AGNRs, the device yield is still very limited, around 10 %, due to the lack of alignment of the GNRs when grown on Au(111). In addition, Ohtomo et al. measured current on high coverage GNRs perpendicularly transferred to the source and drain channel [90], suggesting crosstalk between GNRs at high coverage. As the alignment, coverage and length of the synthesized GNRs (among other factors) influence the final device performance, the search for optimized growth and transfer of GNRs remains a challenging task and a thriving field of research.

1.6 Motivation and objectives of this thesis

1.6.1 Motivation of this thesis

When integrating atomically-precise 9-AGNRs synthesized on gold surfaces into devices, the efficiency of the transfer to insulating substrates is crucial towards optimizing the reliability and performance of the device.
Many factors influence the efficiency of a GNR-based device, amongst ribbon length, ribbon alignment and the coverage of 9-AGNRs. In the current state, the sample transfer of the 9-AGNRs has been optimized to provide an optimal template for a maximized amount of ribbons transferred without destroying their structure. [88] The transfer is greatly improved for samples with a high coverage of 9-AGNRs, as the film behaviour in this case is greatly enhanced.
Transport measurements of devices incorporating high coverage 9-AGNRs yield a strong decrease in single GNR-device efficiency. This decrease arises due to hopping in the transverse direction, inducing a leakage current which in return lowers the current between source and drain and thus a low coverage with one (or only few) GNR is expected to improve the device performance. Previous investigations

however have shown that the transfer at low coverage leads to a significant decrease in transfer quality, indicated by the decrease in alignment and increased ribbon damage after the transfer. Since the ribbons at low coverage primarily grow on the step-edge of the vicinal crystal, the transfer is assumed to be worsened due to the strong adhesion forces towards the edges. Consequently, occupying the step-edge with a passivator before the growth of the 9-AGNRs could lead to growth of the 9-AGNRs further away from the step-edge and potentially improve the transfer efficiency.

1.6.2 Objectives of this thesis

The overall goal of this thesis is to evaluate the Poly(para-phenylene) (PPP) as a potential passivator of the Au(788) step-edge to improve the growth and substrate transfer of low density aligned 9-AGNRs. Figure 1.7 summarizes the challenges of transferring GNRs with high (**a**) and low (**b**) coverage and the strategy to towards improving GNR-transfer (**c**) studied in this thesis. Within this context the specific objectives of this thesis are:

- **To explore the growth and effect of annealing on PPP on vicinal surfaces**: A STM study of PPP at varying coverage aids to understand the growth behaviour of PPP. Thermal stability up to the cyclodehydrogenation temperature of 9-AGNRs (400 $^{\circ}C$) is crucial for PPP to be efficient as a passivator, wherefore it is required to investigate PPP samples exposed to increasing annealing temperature.

- **To investigate the transfer of PPP at varying coverage**: As we are working towards the goal of transferring the GNRs grown together with the passivator PPP, it is worth exploring the transfer of sole PPP at high and low coverage in detail with Raman spectroscopy.

- **To examine the growth of 9-AGNRs on vicinal surfaces both with and without the passivator PPP**: Growth of the 9-AGNRs will be explored on vicinal surfaces at different coverage. Combined with the studies on the PPP, this allows to set up a growth protocol of 9-AGNRs grown on Au(788) together with PPP.

- **To establish growth statistics of GNRs grown on both passivated and unpassivated surfaces**: A detailed analysis of the growth of 9-AGNRs with and without PPP the vicinal surface is necessary to understand the influence of PPP on the growth. Both length and alignment of the GNRs are be investigated.

- **To study combined 9-AGNR + PPP samples with Raman spectroscopy before and after transfer**: The GNRs will be explored before and after transfer, focusing on structural integrity and alignment. These studies will be compared to the investigations of sole 9-AGNR, to understand whether PPP affects the transfer quality.

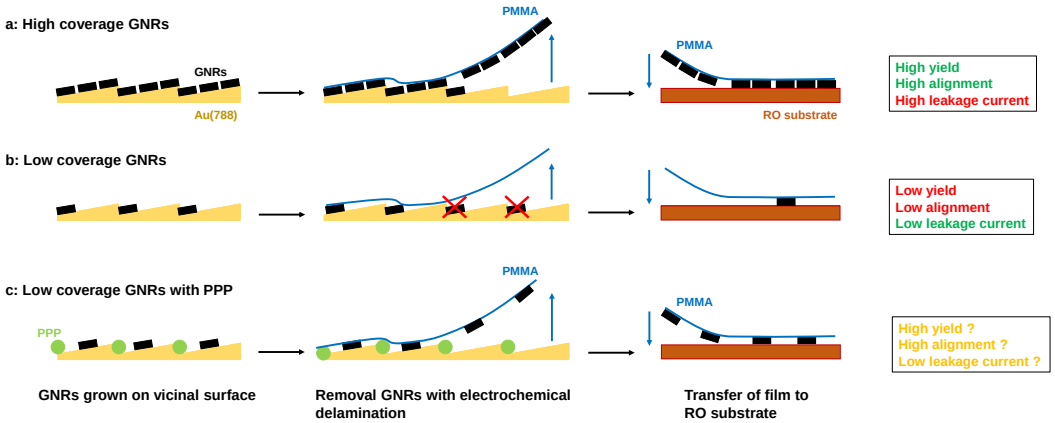

FIGURE 1.7: Transfer of GNRs at varying coverage and the associated challenges. **a**: Transfer of high coverage GNRs yield is favourable in regard to device yield. The device preformance however suffers due to leakage current. **b**: Transfer of low coverage GNRs results in a low yield of GNRs, as they get not transferred reliably. The spacing between the ribbons is however increased, potentially minimising current flow laterally. **c**: Growth of GNRs on surfaces passivated with PPP could solve the issue. The PPP might act as a placeholder, pushing the ribbons outwards. This could in return greatly enhance the device yield after transfer, while maintaining the desired spacing.

Chapter 2

Materials and Methods

2.1 Instruments

2.1.1 Scanning tunneling microscopy in Ultra-high vacuum (UHV)

In the following, we focus on the experimental setup of the STM. First, the basic instrumentation of a conventional STM is discussed. Subsequently, a closer look is taken at the different functionalities of the chambers. The whole system operates in ultra-high vacuum (UHV). A more detailed picture of the principles of a UHV system is provided in the Appendix (see Section A.2.1).

Basic setup of an STM

The standard setup of an STM invokes an atomically sharp tip moving in three dimensions across the surface by a piezoelectric scanner. Since the topography of the surface is obtained by the realization of a constant tunneling current during the scan, feedback electronics are required to process the signal obtained by the tip-sample interactions. The distance is recorded by a computer as a function of the position, yielding the surface topography. A control unit hence always applies the appropriate voltage to the piezodrive for constant tunnel current at constant tunnel voltage. [91]

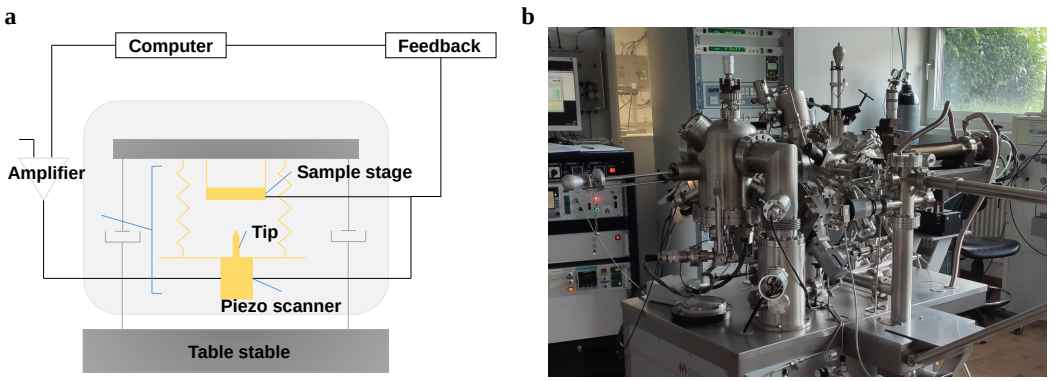

FIGURE 2.1: **a**: Scheme of the basic setup of an STM. The tip is pointing upwards and can be locked-out such that it hangs only supported by springs. The current between the tip and sample is directed towards the feedback electronics and the computer, leading back to the beginning of the circuit through the amplifier with the adjusted voltage. **b**: Photograph of the variable temperature (VT)-STM system employed in the experiments.

The operation of an STM at room temperature requires a high thermal stability to prevent drift during scanning. This extraordinary stability on one hand provided by the *lock out* of the STM, on the other hand due to the whole system being assembled on a *table stable*. The lock out stage allows the tip to hang freely in space, avoiding change of the tip-sample distance due to the external mechanical vibration. The principle of vibrational isolation in this respect is making the two eigenfrequencies of the tunneling assembly and the supporting table very different from each other by letting them oscillate independently. [92] The lock-out is achieved with two stages: The inner stage holds the tip and the sample and it is suspended on three soft springs. The outer stage contains permanent magnets. Copper plates span the space between the two stages. Therefore, vibrations will be damped by the dissipation of the eddy currents that are induced in the copper by the moving magnets. Furthermore, the table stable *AVI-200-M* supporting the STM can provide additional stabilization. The aim of the table stable is to prevent any possible mechanical disturbances from the footing of the instrument, employing passive isolation element (stiff metal springs) and active isolation elements (vibration sensors, control electronics, and actuators). The performance of the springs is augmented and corrected by the active isolation component. The piezo accelerometers convert kinetic vibration energy into electrical signals which are transmitted to the control electronics processing the signal, followed by the sending of a cancellation signal to the actuators. [93] Note that the tip in the system used is mounted pointing upwards, which is not the case in every instrument. While various materials are used for STM tips, the tip used for the measurements of this thesis consists of a Pt-Ir alloy.

Variable Temperature Scanning Tunnelling Microscope (VT-STM)

Figure 2.1 shows the *Scienta Omicron* Variable Temperature Scanning Tunnelling Microscope (VT-STM) used in this thesis. The whole STM is in UHV and thus is operated by avoiding air contact. To illustrate the method of operation in further detail, Figure 2.2 depicts a 2D-scheme of the system, highlighting the major parts of the instrument. In the following, an overview of this particular VT-STM is given by focusing on the functionalities of each of its components.
The system is segmented into three main chambers, namely the analysis chamber (AC), the preparation chamber (PC) and the fast-entry lock chamber (FEL). Gate valves are placed at the connection points of the chambers in order to prevent gas flow across the chambers (see Section A.2.1). The purpose of the FEL is to facilitate the transfer of samples from air into the UHV system, or conversely enable to transfer a sample from inside system to the outside. The preparation chamber is used to prepare samples in UHV, specifically the cleaning of samples, molecule deposition or heating of the surface (see Section 2.3.1). Finally, after preparation the samples can be measured with the STM in the AC. Additionally, it is worth noting that the AC usually is slightly lower in pressure [1] and thus is the desired location for sample storage. Samples are stored in a rotatable 2-levelled carousel with 6 slots, adding up to a total of 12 samples that can be stored simultaneously. Moreover, a gas inlet into the AC can be applied to cool the system with liquid nitrogen or helium. This enables measurements at lower temperatures to damp molecular movement.

[1] The pressure in the PC is slightly higher due to the sample manipulation that are performed. For this reason, the two chambers also must be separated by a gate valve.

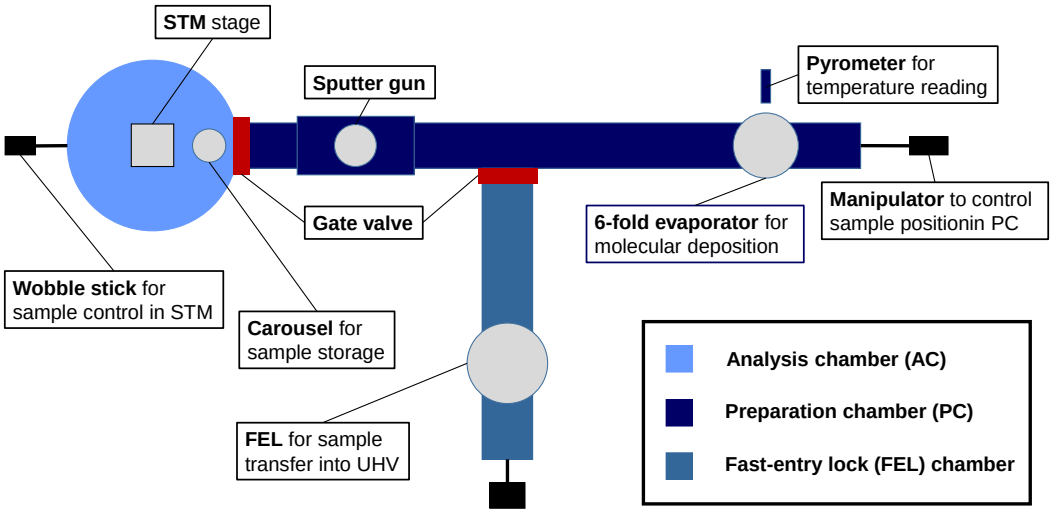

FIGURE 2.2: Scheme of the VT-STM setup. The system is segmented into three chambers: the PC, FEL and AC. Particular parts of use for sample manipulation are labelled.

The preparation in the PC requires a multitude of components working towards reliable and precise production of samples within the system. Therefore, in the following these components are discussed in further detail.

Manipulator The manipulator extends across the PC and is used for movement of the sample in the chamber. The sample is clamped on a sample holder at the end of the manipulator. Since the manipulator can be moved in x, y, z and θ direction, it provides full control of the sample placement and orientation in the PC, essential to attain the different positions for sample preparation. A heating filament is placed below the sample stage, which is required for the heating of surface. The heating current and applied voltage can be adjusted by an external control unit. Temperature reading of the sample is achieved by a *pyrometer* pointing through a window at the end of the PC. A pyrometer allows remote-sensing temperature measurements due to the amount of thermal radiation emitted by the body according to the Stefan-Boltzmann law. [94]

Sputter gun A sputter gun is a tool that generates plasma of argon ions Ar^+ of a gaseous discharge. Accelerated by an electrical field these ions bombard a target leading to the sputtering (i.e. ejection into the gas phase) of the target atoms. [95]

6-fold evaporator For molecular deposition in UHV, the molecules of interest are transferred into a crucible, which subsequently is introduced over the FEL to the Knudsen-type 6-fold evaporator. The 6-fold evaporator is an in-house built component making the study of molecules more efficient by allowing fast switching between the crucibles and simultaneous deposition. Up to six crucibles can be stored in the evaporator. The walls of each crucible holder are perforated with a heating filament, which can be heated to the desired temperature with an external control unit. The evaporator is capped with a rotatable cover, the evaporation shutter, with

a small hole that is used to shut or open the crucible, allowing the molecules to diffuse towards the sample. Proportional-integral-derivative (PID) was used to control the molecule sublimation temperature.

Quartz crystal microbalance The Quartz crystal microbalance (QCM) is located at the end of the manipulator. A QCM consists of a quartz crystal and electrodes. Since quartz experiences the *piezoelectric effect* [96], it generates mechanical stress resulting from an applied electric field. In practice, the application of current induces an oscillation of the quartz crystal. The frequency of oscillation is highly sensitive towards the thickness of the crystal. Consequently, it undergoes a continuous change in frequency as an increasing amount material gets deposited on the surface of the QCM. [97] This conveniently can be used to determine the amount of molecule deposited over time and is thus required to adjust the parameters of molecular deposition to the desired coverage.

2.1.2 Raman spectrometer

Figure 2.3 depicts the *WITec Alpha 300R* Raman spectrometer used in this thesis. The system is coupled with three lasers of different excitation wavelength in the visible and near infrared regime, $\lambda_{ex} = 488\ nm$, 532 nm and 785 nm. The laser power can be tuned to optimize the obtained Raman signal (see Section 2.3.4). The beam path of the 488 nm laser is shown in Figure 2.3, indicating the beam path through the reflecting mirror to the sample on the very bottom, causing the beam to further reflect to the CCDs on top of the tower.

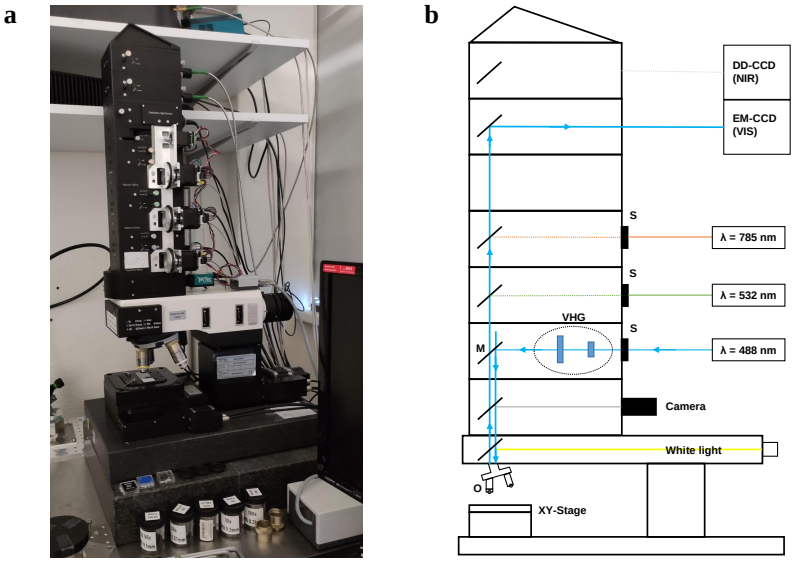

FIGURE 2.3: **a** Photograph of the Raman spectrometer. **b** Scheme of the 488 nm laser path within the Raman spectrometer. Specific components are labelled specifically. (adapted from [88])

The sample is mounted on a motorized xy-stage, allowing to record spatial Raman maps by moving the stage relative to the focal point. All samples are introduced into a vacuum suitcase prior to mounting them on the stage, in order to reduce

noise and photochemical reactions that can potentially damage the GNRs. Scanning of the samples with nanometer resolution is achieved with a piezo stage. When entering the system, each laser passes a shutter (S) that blocks the laser during idle times. Additionally, to tune the polarization of the laser for polarization dependent measurements (see Section 2.3.4), a half-wave plate is used. Wavelength selective optics (VHG) block Rayleigh scattered light, which are designed to transmit most wavelengths with little intensity loss. Mirrors (M) are used to deflect the laser on the vertical path towards the sample. The laser is focused on the sample by passing an objective (O). Different lenses are available, providing a different magnification in the range from 10x to 100x. The light scattered by the sample is collected by the same length and directed back on the vertical path upwards towards the CCD. Note that for the visible wavelength range lasers (excitation with $\lambda_{ex} = 488\ nm$, $532\ nm$) a different CCD is used, as opposed to the near infrared laser (excitation $\lambda_{ex} = 785\ nm$). [88]

2.2 Materials

2.2.1 Single crystals

Au(111) Figure 2.4 shows the surface of a cleaned Au(111) crystal. The surface of an Au(111) crystal is flat, with exception of a pair of channels running over the surface. This is called the *herringbone reconstruction*. It is caused by an energetically favourable reorientation of gold atoms on the surface, resulting in parallel channels of a hexagonal close packed lattice (hcp), spanning over the entire surface, while the bulk Au(111) naturally is fcc reconstructed. [98, 99]

Au(788) Au(788) is an example of a *vicinal* crystal, which in contrast to the flat Au(111) surface consists of *terraces* and *steps*. Such a crystal is fabricated by polishing the Au(111) crystal in an angle relative to the (111)-direction. The terraces are segmented an alternating areas with fcc and hcp reconstruction. Thus, when looking at the surface of Au(788) (see Figure 2.4) pairs of stripes with alternating contrast appear perpendicular to the running direction of the terraces. [100]

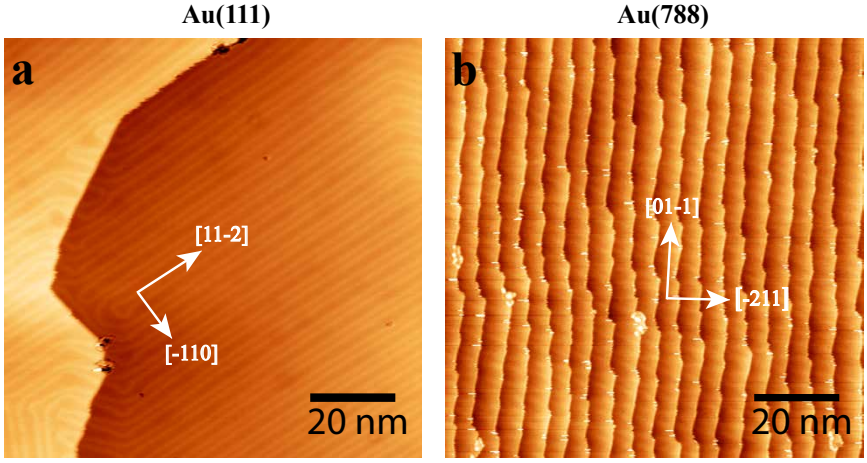

FIGURE 2.4: **a**: Surface of a clean Au(111) on mica substrate. **b**: Surface of a clean Au(788) crystal. The crystalographic on both substrates are indicated. Bias voltage: -1.5 V. Current: 30 pA.

2.2.2 Raman optimized (RO) substrate

To monitor the stability of the GNRs and the quality of the transfer, it is important to be able to perform characterization on the final substrate used for the devices. However, preliminary experiments of GNRs transferred directly to a Si/SiO_2 substrate have shown that the Raman background of the silicon overlaps with the vibrational modes of GNRs crucial for their assessment. A Raman optimized (RO) substrate was developed [88] with the aim to eliminate the silicon background with a particular arrangement of inorganic layers, ultimately enhancing the Raman signal of the GNRs. The RO substrate is fabricated with atomic layer deposition (ALD)-grown Al-oxide layer on 80-90 *nm* thick Ti-Au/Pt source-drain contracting pads on a supporting silicon substrate. Additionally, the silicon might act as an optional gate.
To enhance the interference effect, Raman spectroscopy on a series of substrates with verifying oxide thickness was performed, revealing an oxide thickness of 40 *nm* to be optimal for maximizing the Raman intensity. However, technically the oxide thickness could be adapted to a particular wavelength only according to Bragg's law of interference, which provides even further enhancement as high as 120 with respect to standard Si/SiO_2 substrates. [88]

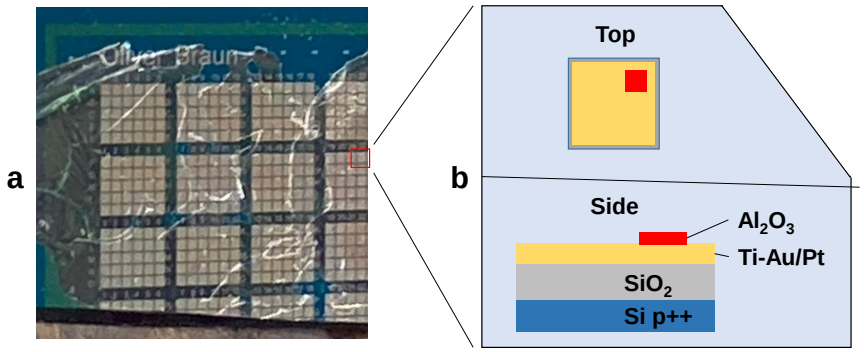

FIGURE 2.5: **a**: Picture of the transferred ribbons with a PMMA layer (see Section 2.3.3). Each pair of adjacent squares represents a device contact for the transport measurements. **b**: Scheme of arrangement of layers RO substrate. Raman spectroscopy is performed on top of the Al_2O_3 layer, providing signal enhancement.

2.2.3 Investigated molecules

Figure 2.6 depicts the two precursors used for this experiment.
The precursor 4,4″-Dibromo-p-terphenyl DBTP **1a** is evaporated onto a gold crystal at a crucible temperature of 102 °C. Upon annealing (see Section 2.3.1) on the gold surface, the molecule polymerizes into Poly(p-phenylene) (PPP) **1b**.
The precursor 3′,6′-diiodo-1,1′:2′,1″-terphenyl DITP **2a** is evaporated onto a gold crystal at a crucible temperature of 67 °C. The target ribbon 9-armchair graphene nanoribbon (9-AGNR) **2c** is formed with a two-step annealing process of the precursors (see Section 2.3.1) over the intermediate **2b**.
The time of deposition for each species is varied to get the desired coverage determined by the QCM and STM measurements.

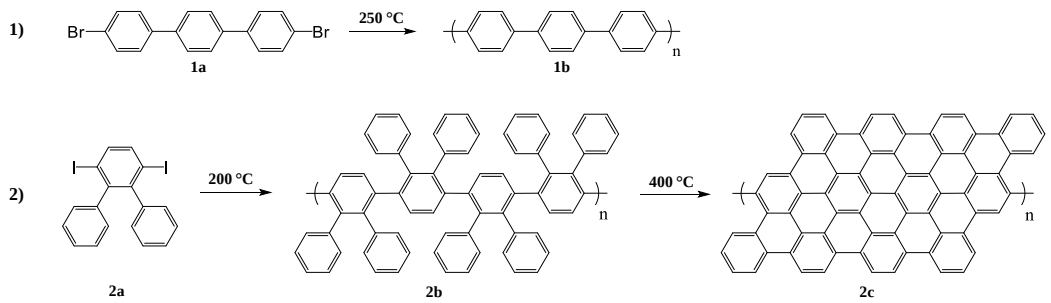

FIGURE 2.6: Molecular precursors and structure of the formed ribbons. Row **1**: The formation of PPP starting from the precursor 4,4″-Dibromo-p-terphenyl with a one-step annealing process on gold. **2**: Synthesis of 9-AGNR using 3′,6′-diiodo-1,1′:2′,1″-terphenyl two-step annealing process on gold.

2.3 Methods

2.3.1 Sample preparation

Sputtering and annealing

A well-cleaned crystal sets the groundwork for sample preparation. The necessity to remove adsorbates and smoothen the surface grants a more uniform and controlled deposition of the investigated molecules. The crystals are cleaned by performing repeated cycles of sputtering and annealing in UHV.
During sputtering, particles on the surface of a solid material are ejected by bombardment of highly energetic argon ions under application of a high voltage. The ejected particles enter their gaseous phase and get absorbed by the molecular pumps. The Ar^+ flow is moderately increased until the pressure in the chamber is in the range of 10^{-6} $mbar$. The sputtering efficiency is optimal if the argon ions are accelerated in a voltage around 650 V, while the current is fixed at 6.6 mA at a sputtering energy of 1.32 kV, as can be tracked by the dedicated control unit.
Remaining adsorbates on the surface are removed by annealing. During annealing, the crystal gets heated to a elevated temperature to cause desorption of molecules and reorientation of the surface atoms of the crystal back to its energetic minimum (i.e. removal of vacancies on the surface). [101] For temperature control, the pyrometer directed to the surface of the sample is used. The voltage is set to 900 V and the current is gradually increased until the desired temperature is reached. A standard annealing cycle for Au(788) is 420 $°C$ for 15 min.

Molecule deposition

Reproducibility and the ability to control the coverage down to the submonolayer regime are key to UHV experiments. Precise deposition is achieved by sublimating the molecules of interest from its crucible in the 6-fold evaporator on the clean crystal. Prior to deposition of a new molecule, the deposition rate is probed with the QCM. The QCM then provides the deposition time necessary to get the desired coverage at a fixed sublimation temperature. In order to stabilize the deposition rate, the crucible is heated at the sublimation temperature for 7 min with a closed shutter, before opening the shutter and initialize the deposition. Since adsorption is

facilitated on cold surfaces, deposition on samples is normally performed at room temperature.

Annealing

The deposited molecules are only precursors, thus requiring an additional step for the formation of ribbons. For these precursors, the polymerization and cyclodehydrogenation is initiated by heat. Thus, subsequent to the deposition, the samples have to be annealed at set temperatures. For the formation of PPP and 9-AGNR, different annealing temperatures are used to form the ribbons (see Section 1.3.2)

- The formation of the PPP is achieved by annealing at 250 $^{\circ}C$ for at least 10 minutes (for dehalogenation and polymerization).
- The formation of 9-AGNR is achieved with a two-step annealing process at 200 $^{\circ}C$ for 10 min (for dehalogenation and polymerization) and 400 $^{\circ}C$ for 10 min (for dehydrogenation and the formation of the ribbons).

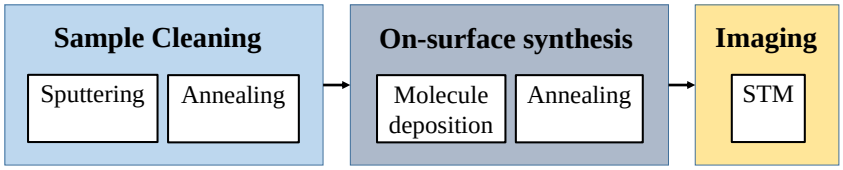

FIGURE 2.7: Scheme of the procedure for sample preparation and measurement in UHV.

2.3.2 Measurement with STM

Prior to the measurement, the sample is clamped upside down on the sample stage because the tip approaches from below. Subsequently, the tip is locked out such that it hangs freely from the supporting springs.
Using a camera, the tip is manually brought close to the sample surface employing a coarse motion control unit. For topological measurements, the *Matrix* SPM software is used. The exact approach is initiated with Matrix, following a stepwise movement of the tip while constantly measuring the current through the feedback electronics. Once the tunneling current between the tip and sample is raised, the approach stops automatically and the measurement can be started.

2.3.3 Transfer to Raman optimized (RO) substrates

The growth substrate Au(788) provides an optimal template for the aligned growth of ribbons. For the ensuing transfer to the RO substrate, the electrochemical delamination method is used. The first step is spin coating (2500 rpm for 40 s, four layers) PMMA on the Au(788) crystal with the synthesized ribbons [102], which acts as a support layer during the transfer. This support layer stabilizes the ribbons just enough to prevent major damage during the delamination but is however not too stiff to impede the delamination. Then, the PMMA is cured in the oven at 80 $^{\circ}C$ for 10 min. To remove the PMMA at the crystal edges, the sample is exposed to UV radiation for 80 min with subsequent development in water/isopropanol for 3 min. This process reduces the delamination time (down to 45 s), thus further minimizing

damaging of the ribbons during the process.
The delamination is performed in an electrochemical cell with a carbon rod anode and the GNR/Au(788) sample as cathode, in a 1 M NaOH bath as electrolyte. A voltage of 5 V is applied at a current of 0.2 A, causing the formation of hydrogen bubbles between the PMMA+GNR/PPP (or PMMA+GNR) layer and the growth substrate. Once the edges of the PMMA+GNR/PPP layer start to peel off, the whole film can be peeled off with a tweezer in a water bath. Subsequently, the film can be transferred onto the RO substrate. In the next step, the transferred sample is annealed at 80 $°C$ for 10 min, followed by 110 $°C$ for 20 min, leading to an increase in adhesion between the substrate and the PMMA+GNR/PPP layer. To remove the PMMA, the sample is dissolved in acetone (15 min). Finally, the remaining GNR/PPP RO substrate is rinsed with ethanol and ultrapure water. [88]

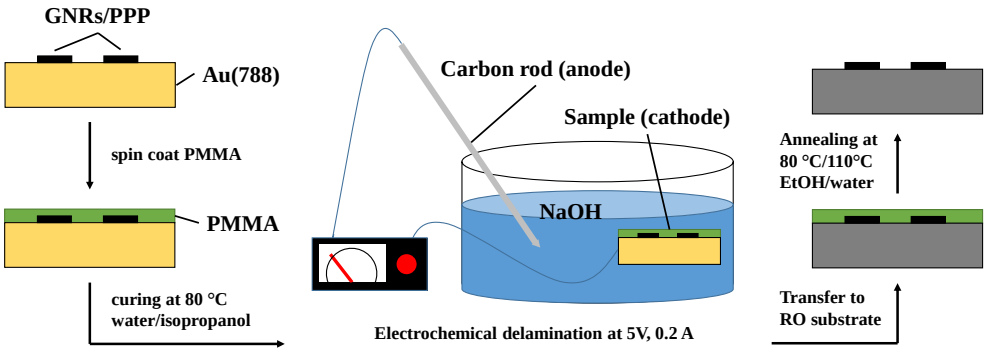

FIGURE 2.8: Scheme of the procedure for the electrochemical delamination method of GNRs from its growth substrate to the Raman optimized substrate.

2.3.4 Characterization of nanoribbons with Raman spectroscopy

Adaptation of measurement parameters

Investigation of novel samples with Raman spectroscopy requires the optimization of the measurement parameters in order to get a favourable signal intensity. Since each sample potentially has highly individual properties it is beneficial to adapt the measurement parameters whenever a new material is investigated or the coverage is altered significantly.

Laser wavelength According to the optical bandgap of the investigated material different lasers could enhance the signal accordingly. In addition, for a given sample certain modes can be highly sensitive to the laser used. Three different lasers are available, namely 488 nm, 532 nm and 785 nm. To ensure that no modes are missed during the characterization, each sample is investigated with all the available lasers.

Z-distance The coarse positioning of the distance between the sample and the lens in the Z-axis during the calibration process generally has to be further optimized. Z-line spectroscopy is an automatic process, during which the system performs a series of scans at different Z-positions altered by 1 μm around the previously set height. This allows the system to be accurately calibrated to the Z-position of highest G-peak

intensity. In the example in Figure 2.9 **a** the signal intensity peaks at ΔZ around 12 μm.

Laser power Often the signal can be further enhanced by increasing the power of the applied laser. However, contrary to the expectation that an increase in laser power always correlates with an increase in signal intensity, the risk of damaging the sample has to be taken into account with high laser powers. This is especially important for the higher energy lasers (488 nm and 532 nm), while the samples usually are less prone to damage with the 785 nm laser. The laser power was optimized for each sample and varied from 5 mW to 10 mW (488 nm laser), 10 mW to 20 mW (532 nm laser) and 40 mW (785 nm laser).

Integration time Similarly to the laser power, the selection of the integration time also requires to find a balance between signal intensity and minimizing the risk of irradiation damage. This parameter reflects the time the CCD collects light. A longer integration time results in increased signal acquisition, inherently increasing the signal intensity. However, as a consequence the sample is constantly exposed to light during the integration time, potentially leading to damaging of the sample. The integration time was optimized for each sample and varied from 1 s to 20 s.

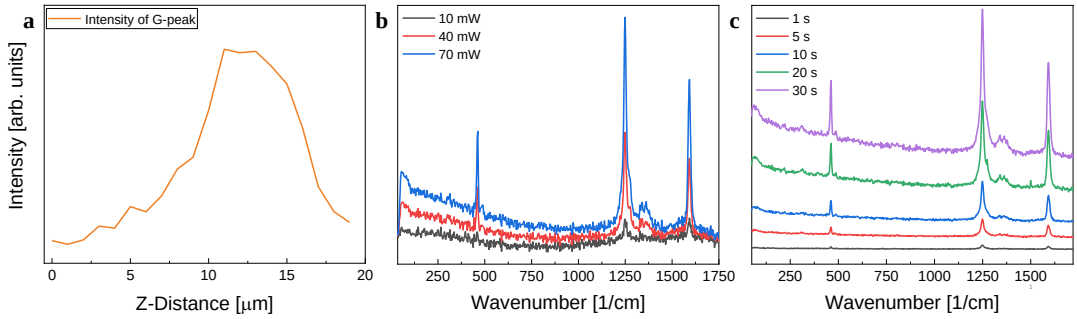

FIGURE 2.9: **a** Z-line spectrum of the sample, recording the intensity of a selected peak (here G-peak of GNRs at 1598 cm^{-1}) as a function of the distance of the sample to the lens. **b** Raman spectra of PPP annealed at 400 $^{\circ}C$ measured with the 785 nm laser at varied laser powers. An increase in intensity with increased laser power is observed, without any broadening of the peaks, pointing towards preserved structural integrity due to the measurement in vacuum. **c** Raman spectra acquired with the 785 nm laser of PPP annealed at 400 $^{\circ}C$ with different integration times. Similarly, an increase in intensity is observed with increasing integration time, without significant broadening.

Raman mapping

An additional approach towards preventing burning of the sample as a consequence of the intense irradiation over time is *Raman mapping*. In order to attain a more elaborate characterization of the available samples, Raman spectra are collected over a multitude of points (usually 5 points per line $\times$ 5 lines per image) across a larger scale area (usually 10 $\mu m \times 10$ μm). The final spectrum therefore is composed of the average of all the recorded spectra spread over the area of interest. This not only provides a more accurate large-scale representation of the sample but also prevents

GNR damage due to the stepwise movement of the laser focus across the sample surface.

Polarization dependent Raman spectroscopy

As previously established the Raman modes are strongly dependent on the symmetry and overall geometry of the investigated molecules. Consequently, the polarization direction light incident to the sample strongly influences the intensity of the observed Raman modes. Moreover, polarization dependent Raman spectroscopy allows to make conclusions about the alignment of the GNRs due to the parallels between growth direction and symmetry of the ribbons.
To provide accurate adjustments of the angles without mechanically interfering with the system by touching the system during the measurements, the polarization direction of the incident light can be automatically changed through control wheels with stepper motors. The step size and interval of angles can be adjusted using the dedicated *LabView* program.

Measurement conditions

The measurements are performed in an in-house built vacuum suitcase lowering the pressure to 10^{-3} *mbar* because all investigated samples incorporate GNRs which might undergo a photochemical reaction at certain photon energies when exposed to air. [103] The samples are measured on a vicinal Au(788) substrate and on a RO substrate after transfer. All measurements are performed at room temperature.

Chapter 3

Results and Discussion

3.1 Poly(para-phenylene) (PPP)

Poly(para-phenylene) (PPP) [104] is a nanowire [105] consisting of an extended chain of conjugated phenyl-rings and can be classified as a GNR wit $N = 3$. To avoid confusion with wider GNRs studied in this thesis, we however refrain from referring the PPP to a GNR and instead refer to a PPP wire. In the following, the growth of PPP on vicinal surfaces will be explored. Additionally, to gain insights on the behaviour of PPP as a passivator, examinations on the behaviour of the PPP at different annealing temperatures will be analyzed.

3.1.1 Growth of PPP on Au(788)

Coverage

The growth of PPP on Au(788) was investigated with samples of varying coverages (i.e. deposition times). The aim is to ultimately gain insights into the growth properties of the PPP.
PPP is grown in a one-step annealing process. After deposition of the precursor DBTP (see Section 2.2.3) annealing between 200 $^{\circ}C$ and 250 $^{\circ}C$ is expected to induce complete debromination of the precursor on Au(111). [106] Since the synthesis of PPP on different substrates yielded comparable debromination temperatures [107], 250 $^{\circ}C$ was used for the synthesis on Au(788). As seen by the low coverage sample (crucible temperature: 100 $^{\circ}C$, deposition time: 5 min, annealing: 250 $^{\circ}C$) in Figure 3.1 **a**, PPP exclusively grows along the step-edges at this coverage, indicating that the precursors preferably diffuse towards the edges of the crystal and subsequently polymerize at that location. Gaps in between the PPP wires on Au(788) are present due to a lack of precursors necessary to further grow and combine into longer nanowires. Based on this, no wires growing towards the center of the terraces are observed at this coverage.
Even though the precursor during the process of annealing diffuses freely on the surface, the formed PPP does not exhibit significant movement at room temperature and can easily be imaged even at low coverage. However, lower annealing temperatures of the sample (see Figure A.1 in Appendix A.3.1) exhibited a lot of movement on the surface, which points towards the diffusion of precursors on the surface. Thus, the formation of the PPP is concluded to be incomplete since the dehalogenation temperature was not yet reached. [106, 107]
A noticeable observation of the PPP grown at low coverage is the high degree of directionality along the terraces because it grows as close to the step-edge as possible if enough space is available. Note that the growth of PPP exclusively at the step edges at such low coverage is an essential property of a passivator since it might act as a

placeholder preventing the growth of other precursors close to the step-edge.

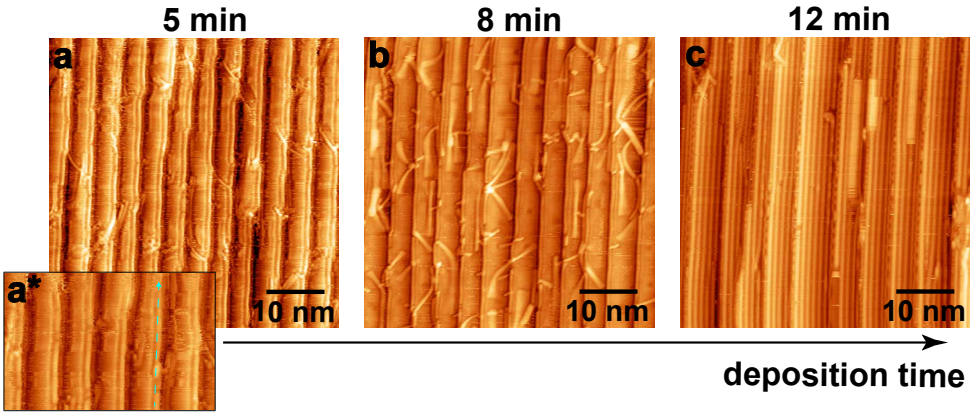

FIGURE 3.1: PPP on Au(788) with increasing coverage. **a**: PPP grown with 5 *min* deposition at 100 °*C*. Bias voltage: -2 *V* Current: 30 *pA*. **a***: Close op of the surface. The blue arrow highlight a PPP wire growing close to the step-edge. **b**: PPP grown with 8 *min* deposition at 100 °*C*. Bias voltage: -1 *V* Current: 30 *pA*. **c**: PPP grown with 12 *min* deposition at 100 °*C*. Bias voltage: 0.2 *V* Current: 30 *pA*.

Slightly higher coverage (crucible temperature: 100 °*C*, deposition time: 8 *min*, annealing: 250 °*C*) results in small wires of PPP growing across the terrace (see Figure 3.1 **b**). This arises due to the lack of space at the step-edge once it is completely filled with PPP. Consequently, the excess of precursors cannot recombine with the PPP at the step-edge and they recombine with other remaining PPP precursors diffusing further towards the center of the terrace, resulting in the formation of additional short PPP wires. These short PPP nanowires however do not preferentially grow in alignment with the steps due to their short length. But wires can also be observed growing aligned and towards the center of the terrace. The short length of these wires mainly arises due to the fact that less precursor is left available on the surface to polymerize with and hence causes significantly shortening the length.
In regard to PPP acting as a step-edge passivator for directing the growth of 9-AGNRs towards the center of the terrace, it is apparent that a coverage of PPP exceeding the coverage of one wire per step might hinder the seamless growth of longer 9-AGNRs towards the center of the terraces. It is thus crucial that the coverage is not exceeding the one PPP wire per step coverage by a large amount.

Figure 3.1 **c** shows PPP grown at high coverage (crucible temperature: 100 °*C*, deposition time: 12 *min*, annealing: 250 °*C*). The terraces are now fully occupied with PPP. A high degree of alignment is observed for this sample, including the wires growing towards the center of the terrace. Similar observations were made on other vicinal surfaces. [108] In contrast to the previous sample, the precursor at high coverage diffuses in large excess on the surface and basically fully occupies the surface. This not only applies for the PPP grown along the step-edge but also the surplus of precursors. The huge abundance of precursors on the surface results in a recombination of the totality of precursors into nanowires while annealing. Therefore, the PPP grows as long as possible with a superior degree of alignment in order to incorporate as many of the precursors as possible. This formation with increased length and maximal alignment is thus energetically favoured.
It is important to note that this coverage is not specific to one deposition time. As

soon as a full monolayer of precursor is deposited on the surface, additional precursors do not dehalogenation to the polymerization. This is due to the fact that the PPP requires the gold surface to catalyze the dehalogenation. Adsorbates on top of the monolayer cannot contribute to the growth of the PPP since they are not located close enough to the surface and will desorb upon annealing.

Annealing temperature

Besides the growth behaviour, the temperature stability of PPP also plays an essential role in the quality of these wires as a passivator. In the following, the behaviour of PPP at temperatures exceeding its polymerization temperature is investigated. The duration of each annealing step is 10 *min*. Both high and low coverage samples were prepared. Stability of PPP at higher temperatures is necessary due to the increased temperature needed to dehydrogenate the 9-AGNRs. Since this process occurs at 400 °*C*, temperature dependence was only examined up to this limit.

High coverage PPP at higher temperatures Figure 3.2 **a** depicts the PPP sample grown with high coverage (crucible temperature: 100 °*C*, deposition time: 10 *min*, annealing: 250 °*C*). Besides the long and highly aligned PPP on top of the terraces as discussed in Figure 3.1 **c**, the steps show a distinct pattern. Figure 3.2 **a*** shows a close up of the steps of the sample annealed at 250 °*C*. A rippled structure appears along the steps. Since vicinal surfaces are not in equilibrium, the motion of the adatoms on the surfaces is strongly influenced by the presence of the steps. [109] Consequently, the observed pattern could arise from the interaction of mobile atoms on the surfaces with the top and bottom of the step-edge. [110]. This process, called *step bunching*, is strongly influenced by height of the steps. [111, 112] However, since the PPP does not diffuse at room temperature according to the STM image shown for example in Figure 3.1 **a**, this points towards the presence of another species on the surface. Considering that bromine remains bound to the gold surface up to a temperature of 300 °*C* [48], it is suggested that the step bunching is caused by the bromine atoms yielded from the dehalogenation diffusing on the surface.

The pattern is not observed anymore once a second annealing at a slightly higher temperature (300 °*C*) is done (Figure 3.2 **b**). Thus, no precursors are left to diffuse on the surface at this temperature, which is in accordance with the experimentally determined desorption temperature of bromine. [48] Small areas of the blank gold surface appear, thus providing enough space for the PPP to laterally diffuse after the bromine desorption. As a result short nanowires appear on the surface, oriented across the terrace induced through the thermal annealing. In Figure 3.2 **b**, indeed a reduction of the degree of alignment compared to Figure 3.2 **a** is observed as expected by the presence of the shorter wires.

The structure of the wires is significantly altered as the temperature is raised to 400 °*C*. Ribbons significantly wider than the PPP appear on the surface. Thus, annealing at 400 °*C* provides enough energy for the surface catalyzed fusion of PPP into wider ribbons, as supported by other investigations [107]. In Section 3.1.2 more elaborate prove for the formation of wider GNRs (and thus fusion of PPP) is provided with Raman spectroscopy. In Figure 3.2 **c** some 9-AGNRs formed on the surface are clearly visible as highlighted. Moreover, large bright islands are present on the terraces, immediately evident due to the impression of increased coverage compared to Figure 3.2 **b**. It is however assumed to be a cause of the tip dragging some shorter

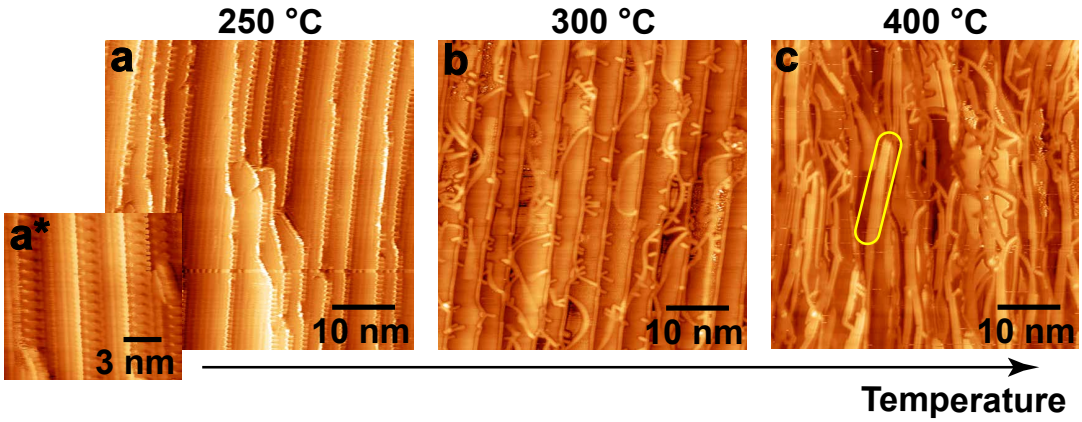

FIGURE 3.2: High coverage PPP grown on Au(788) with gradual increase in annealing temperature. **a**: High coverage PPP annealed 250 $°C$. Bias voltage: -0.2 V Current: 30 pA. **a***: Close up of the pattern at the step-edge of **a**. Bias voltage: -0.5 V Current: 30 pA. **b**: High coverage PPP annealed 300 $°C$. Bias voltage: -2 V Current: 30 pA. **c**: High coverage PPP annealed 400 $°C$. Bias voltage: -1.5 V Current: 30 pA.

structures on certain areas of the surface. Thus, areas with different contrast might in fact be empty.

To determine whether the annealing temperature significantly influences the passivation process, the effect of annealing of a low coverage (one wire of PPP per step) has to be investigated, as this represents the target coverage for the sample with 9-AGNR grown together with PPP.

Low coverage PPP at higher temperatures To achieve complete understanding of the behaviour of PPP at higher temperature, a control sample with a coverage of exactly one PPP per step-edge was prepared. The aim was to simulate the two step annealing process of the 9-AGNRs (see Section 2.3.1) without yet growing ribbons and hence solely analysing the effect of temperature on low coverage PPP.
Figure 3.3 shows identically prepared low coverage samples (crucible temperature: 102 $°C$, deposition time: 2 min 35 sec, annealing: 250 $°C$) exposed to different annealing temperatures. It is important to point out that the sample in Figure 3.3 **a** is different from the sample shown in both Figure 3.3 **b** and **c**. Since the first measurements of the sample were not clear, a second sample depicted in Figure 3.3 **a** was prepared with equal conditions. However, it can be seen that the coverage of PPP in 3.3 **a** is slightly lower compared to the sample depicted in 3.3 **b** and **c** as can be seen by the gaps between the PPP wires growing along the step-edge. The duration of each annealing step amounts to 10 min as before. As shown in Figure 3.3 **b**, an annealing temperature of 200 $°C$ does not significantly influence the composition of the PPP structures on the Au(788) surface. As expected, temperatures below the polymerization temperature of PPP does not facilitate the formation of fused species. Additionally, even though the prolonged total annealing time gives the PPP precursors more time to diffuse, the formation of PPP wires occurs rapidly. The first annealing step (10 min) is sufficient time for the wires to fully recombine and polymerize at the step-edge, wherefore the annealing step at 200 $°C$ is not expected to influence the formation of PPP.

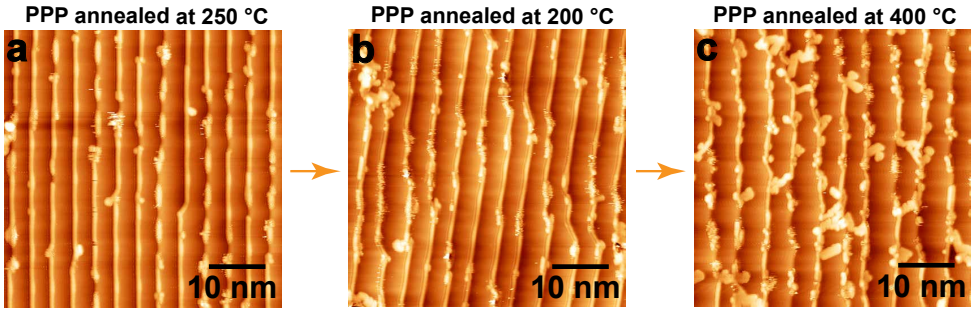

FIGURE 3.3: Low coverage PPP grown on Au(788) with one PPP wire per step coverage at annealed different temperatures. **a**: Low coverage PPP annealed at 250 °C. Bias voltage: -2.1 V Current: 30 pA, **b**: Low coverage PPP annealed at 200 °C. Bias voltage: -2.1 V Current: 30 pA. **c**: Low coverage PPP annealed at 400 °C. Bias voltage: -2.1 V Current: 30 pA.

Annealing of low coverage PPP at 400 °C however causes significant changes on the sample. Comparing Figure 3.3 **c** with **b**, annealing at 400 °C induces the formation of small wires bridging across the terraces. These ribbons appear in varying widths, suggesting lateral fusion of PPP into GNRs at low coverage. Moreover, while the step-edges in Figure 3.3 **b** are completely occupied with PPP, gaps appear within the wires of PPP after annealing, supporting the claim of PPP diffusing at higher temperatures. Even though PPP fuses at 400 °C at this coverage, the majority remains close to the step-edge, wherefore it still might act as a passivator when GNRs are grown.

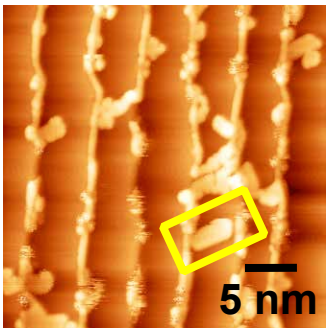

FIGURE 3.4: Close up of the diffused precursors on the low coverage PPP sample in Figure 3.3 **c** after annealing at 400 °C. Bias voltage: -2.1 V Current: 30 pA.

Figure 3.4 shows a close up image after annealing the sample at 400 °C. The structure highlighted with a yellow rectangle may represent a formed 9-AGNR. However, as can be seen by the impurities situated at the edges, the tip notably drag the precursors across the surface. Consequently, some structures could appear a bit wider than their actual size, as manifested by the difference in width of the ribbon towards the left side compared to the right side. On the other hand, this GNR-like structure could originate from multiple wires of PPP bridging the terrace as seen directly above the highlighted structure.

To complement the STM measurements, we use Raman spectroscopy for a larger-scale measurement and to characterize the Raman fingerprints of the PPP annealed at different coverage and temperatures.

3.1.2 Raman spectroscopy of PPP on Au(788)

Raman study of high coverage PPP annealed at high temperatures

In this chapter, the effect of temperature on PPP grown at high coverage on Au(788) was investigated. Understanding the effect of annealing at higher temperature than used for the synthesis of PPP is essential, as the temperature for the growth of 9-AGNRs needs to be raised to 400 °C. Figure 3.5 depicts the three samples that were prepared for this investigation, starting from a sample of PPP at high coverage (deposition at 100 °C for 12 *min*) annealed at 250 °C. The preparation of each sample was modified by altering annealing protocols as follows:

- **a** : High coverage PPP (no further annealing after synthesis at 250 °C)
- **b** : High coverage PPP stepwise annealed [1] to 400 °C
- **c** : High coverage PPP annealed directly to 400 °C in one step

The duration of each annealing step was 10 *min*.

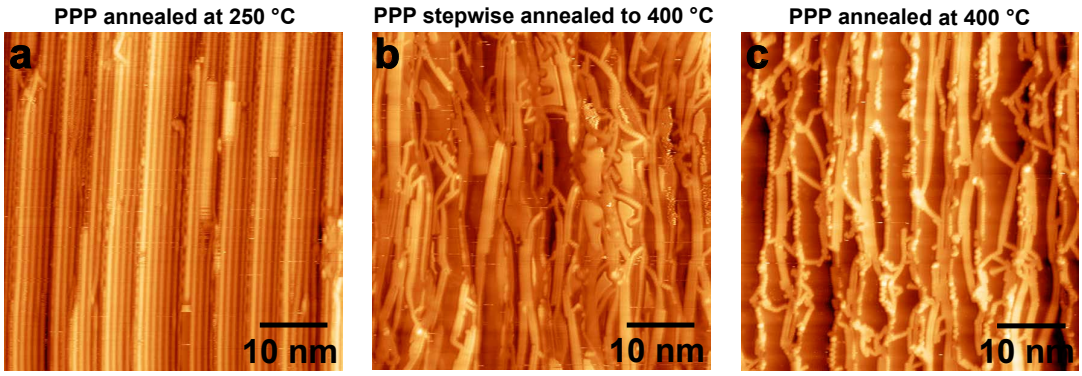

FIGURE 3.5: STM images of three samples prepared for Raman spectroscopy characterization to investigate effect of temperature on PPP structure. **a**: High coverage PPP annealed at 250 °C. Bias voltage: 0.2 *V* Current: 30 *pA*. **b**: High coverage PPP stepwise annealed to 400 °C. -1.5 *V* Current: 30 *pA*. **c**: High coverage PPP directly annealed to 400 °C. Bias voltage: -1 *V* Current: 30 *pA*.

Raman spectra of the samples were collected using three lasers: 488 *nm*, 532 *nm* and 785 *nm*. Optimized measurement parameters (see Section 2.3.4) were used in order to improve the signal-to-noise ratio of the Raman spectra. The recorded spectra for each laser energy are shown in Figure 3.6. As the PPP can be classified as the narrowest GNR with width N = 3, it is expected that similar peaks arise compared to Raman spectroscopy of wider GNRs [88, 113, 114] due to the same symmetry. Therefore, in the following the peaks are referred to the terminology discussed in Section 1.4, as the G, C-H and D modes, and RBLM.

To shorten the nomenclature of the samples, we will in the following refer to the samples annealed at higher temperatures as PPP stepwise annealed to 400 °C for sample **b** in Figure 3.5 and directly annealed at 400 °C for sample **c** in Figure 3.5. These samples include an extra annealing step at 250 °C to form the PPP first, followed by annealing up to 400 °C. The PPP annealed at 250 °C in Figure 3.5 **a** however was not

[1] The temperature thereby was increased gradually in steps of 50 °C (So: 300 °C, 350 °C, 400 °C).

annealed further after its synthesis.

No Raman signal was obtained with the 785 nm laser for the PPP annealed at 250 $°C$. As seen in the STM images for this sample in Figure 3.5, solely PPP is present when annealing at 250 $°C$. The absence of signal for exclusively this sample suggests that this laser is not in resonance with PPP. Since the 785 nm laser has the lowest energy of the three employed lasers with 1.54 eV, its energy is not sufficient to excite the PPP that has an optical band gap at 3.6 eV [115]. Based on that, we understand that the peaks obtained for both samples with PPP annealed to 400 $°C$ correspond to other structures, such as fused ribbons forming wider GNRs probably with a lower band gap. The 9-AGNR for example has an optical band gap of around 1 eV [116] and is in ressonance with the 785 nm laser energy as previously observed by Borin Barin and Overbeck et al. [80, 88]
All samples exhibit a sharp G peak with every laser. The G peak originates from the longitudinal and transversal vibrations of all atoms within the sp^2-framework. [76] All carbon atoms in PPP are sp^2-hybridized, wherefore the presence of a G peak is expected. For the PPP annealed at 250 $°C$ the G mode is oberved at 1600 cm^{-1} for every laser. In contrast, the PPP annealed at 400 $°C$ shows a slight redshift, especially for the 532 nm and 785 nm laser. As a reference, the G peak of 9-AGNR usually is found around 1596 cm^{-1} [76]. The observed redshift could be a first indication on the formation of GNRs for the samples annealed at 400 $°C$. In addition, note that the spectra acquired with the lower energy 785 nm laser cannot originate from the PPP because the sample annealed at only 250 $°C$ does not show any signal. The presence of the G peak for both PPP stepwise and directly annealed to 400 $°C$ show that structures with an sp^2-lattice are formed. Moreover, exclusively for the sample with PPP directly annealed to 400 $°C$, the spectra for the 488 nm laser show a small-scaled peak at 1650 cm^{-1}. Although the origin of this peak in GNRs is not yet understood, Raman spectroscopy of graphene shows parallels with a D' mode peak appearing at 1620 cm^{-1} related to the presence of defects within the graphene lattice [117].

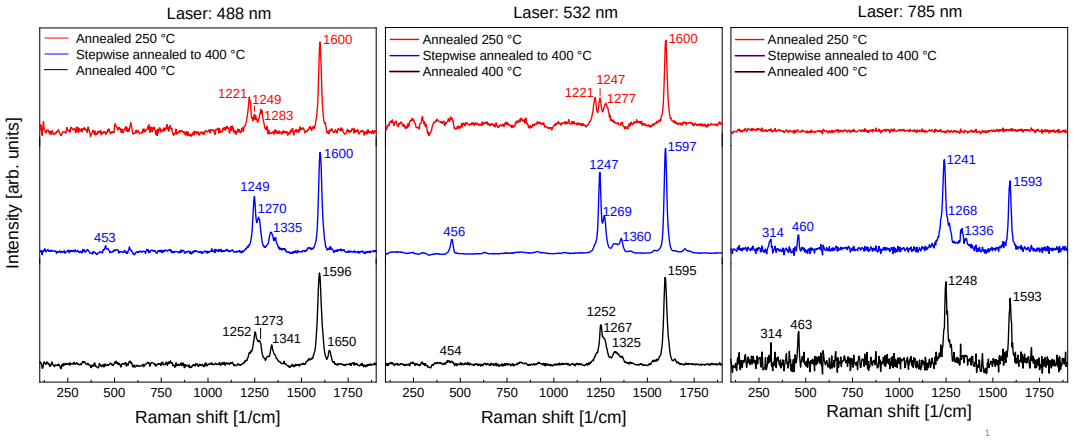

FIGURE 3.6: Raman of prepared high coverage PPP samples on Au(788). Three samples are shown: 1. High coverage PPP annealed at 250 $°C$. 2. High coverage PPP stepwise annealed to 400 $°C$. 3. High coverage PPP directly annealed to 400 $°C$.

The PPP annealed stepwise to 400 $°C$ shows a clear peak in the low wavenumber range at 456 cm^{-1} well visible with the 532 nm laser. This frequency is in accordance with experimental observation on the RBLM for 6-AGNRs around 460 cm^{-1}. [118] As previously discussed, the RBLM corresponds to a vibration of carbon atoms within the GNR perpendicular to the long axis of the ribbon. While the 9-AGNR shows a Raman shift located at 314 cm^{-1}, the RBLM for the narrower 6-AGNR is blueshifted, which is in agreement with other experiments on the RBLM shift towards higher wavenumbers with decreasing width of the GNR. [76] In contrast, the PPP annealed at 250 $°C$ show no corresponding peaks at lower wavenumbers. PPP directly annealed to 400 $°C$ shows a small-scaled peak almost diminished in the noise, pointing towards only a sparse formation of wider GNRs. This observation suggests that the stepwise annealing process of PPP to 400 $°C$ promotes the fusion of PPP to 6-AGNRs in higher amounts compared to PPP directly annealed to 400 $°C$. The main difference between the sample with PPP stepwise annealed to 400 $°C$ and PPP directly annealed to 400 $°C$ is the annealing time at temperatures above 250 $°C$ because of the intermediate annealing steps, while the final temperature is the same for both samples. Prolonged exposure of PPP to temperatures above 250 $°C$ appears to enhance the amount of fusion.
These observations go in-hand with the STM images shown in Figure 3.5 that indicated formation of wider GNRs for both PPP stepwise and directly annealed to 400 $°C$. The observations on the formation of GNRs on both PPP stepwise annealed to 400 $°C$ and PPP directly annealed at 400 $°C$ are underpinned by the data acquired with the 785 nm, showing RBLMs for 6-AGNRs around 460 cm^{-1} for both samples annealed at 400 $°C$. A second peak at 314 cm^{-1} appears for both PPP samples annealed at 400 $°C$, corresponding to the RBLM of 9-AGNRs. [43] With PPP directly annealed to 400 $°C$, the relative intensity between the RBLM of 9-AGNR and the RBLM of 6-AGNR is much lower compared to PPP stepwise annealed to 400 $°C$. Although the RBLM of 9-AGNR for PPP directly annealed to 400 $°C$ is hardly visible, the presence of 9-AGNRs is confirmed by the Raman data after transfer on the RO substrate in Section 3.1.3.
In addition, as previously concluded by the observations on the lack of signal with the 785 nm laser for PPP annealed at 250 $°C$, no RBLMs or other modes at lower wavenumbers appear for that sample. Supported by the STM data, these observations prove that the PPP does not fuse at 250 $°C$.
Figure A.2 in Appendix A.4 also shows the LCM, depending on the length of the GNRs, for all investigated samples around 107 cm^{-1}.

C-H and D modes between 1200 cm^{-1} and 1350 cm^{-1} are present in all samples measured with each laser. Since these modes arise due to the bending of the C-H bonds, they indicate that in both the PPP annealed at 250 $°C$ and PPP annealed at 400 $°C$ hydrogen-passivated edges are present.
Comparing the both samples with PPP annealed at 400 $°C$ with PPP annealed at 250 $°C$, we see that the C-H mode around 1250 cm^{-1} significantly increases in intensity relative to the D mode. This observation on the increase in C-H mode intensity with increased annealing temperature is in accordance with the previously reported observations by Basagni et al. [106]. As indicated by the STM images and the supporting Raman data on the fusion of PPP, it is however not possible without more elaborate experimental and theoretical investigation to make profound conclusion on the origin of the differences between these peaks.

Summarizing the above observations, the longer annealing time for the sample stepwise annealed to 400 $^{\circ}C$ indeed enhances the amount of fusion. The PPP can diffuse more on the surface and find other PPP wires (or wider GNRs) to fuse with. As seen by the peaks and supported by STM measurements of the samples seen in Figure 3.5, the higher temperature induces the formation of GNRs for both samples, even if to a varying extent.
Moreover, it is important to note that the G peak of all spectra of the discussed samples is very sharp. The lack of broadening indicates that structural integrity of the structures on the surface is preserved.

Raman study of low coverage PPP

The measurements and analysis of high coverage PPP on gold helped us to gain insights into the Raman peaks of sole PPP and the effect of annealing at 400 $^{\circ}C$ on the PPP, manifested by the RBLMs appearing for the samples annealed at higher temperatures.
It is however also necessary to analyse the spectra of low coverage PPP, as this will be the targeted coverage for the sample with both PPP and 9-AGNR gradually grown on the Au(788) surface. In this respect, the sample with one PPP per step coverage annealed at 400 $^{\circ}C$ was investigated, which corresponds to the same sample that was already prepared for measurements with STM (see Figure 3.3). Once we achieved understanding on the peaks of the PPP, the distinction between peaks of PPP and peaks of 9-AGNRs will more accessible for the combined PPP+9-AGNR sample.

Figure 3.7 shows a comparison between two high coverage PPP samples (PPP annealed at 250 $^{\circ}C$ and PPP directly annealed at 400 $^{\circ}C$ [2] from Section 3.1.2) and the low coverage PPP annealed at 400 $^{\circ}C$ [2]. The intensity of the low coverage PPP measured with the 488 *nm* laser is significantly weaker compared to the high coverage PPP samples. Comparing all samples with the 488 *nm* laser, we see that high coverage PPP annealed at 400 $^{\circ}C$ has the highest signal-to-noise ratio. As already concluded in Section 3.1.2, the high coverage PPP samples annealed at 400 $^{\circ}C$ show contributions of 6- or even 9-AGNRs, leading to further signal enhancement. The low coverage PPP annealed at 400 $^{\circ}C$ on the other hand did not yield any signal for the 785 *nm* laser, indicating that no detectable amount of GNRs are formed on the gold surface at low coverage. This is supported by the absence of RLBMs for this sample with both the 488 *nm* and 532 *nm* laser.
Due to the low coverage, the amount of fusion induced by annealing at higher temperatures is lowered. This is reasonable due to the decrease in probability that two segments of PPP wires meet and fuse at low coverage. The STM images of this sample (see Figure 3.4) suggest that some tiny ribbons might be formed on the surface. Although the absence of RBLMs for 6- or 9-AGNRs with the 785 *nm* laser show that the formation occurs in minor amounts.

Additionally, as already observed for the high coverage PPP samples, the spectra acquired with the 532 *nm* laser is more intense compared to the 488 *nm* laser for the low coverage PPP annealed at 400 $^{\circ}C$. Therefore, this shows that PPP is more in resonance with the 532 *nm* laser.

[2] A previously mentioned, the term directly annealed denotes that only one additional annealing step to reach 400 $^{\circ}C$ was used after initially annealing at 250 $^{\circ}C$ to synthesize the PPP. Therefore, the term directly annealed refers to two annealing steps: First at 250 $^{\circ}C$, followed by 400 $^{\circ}C$

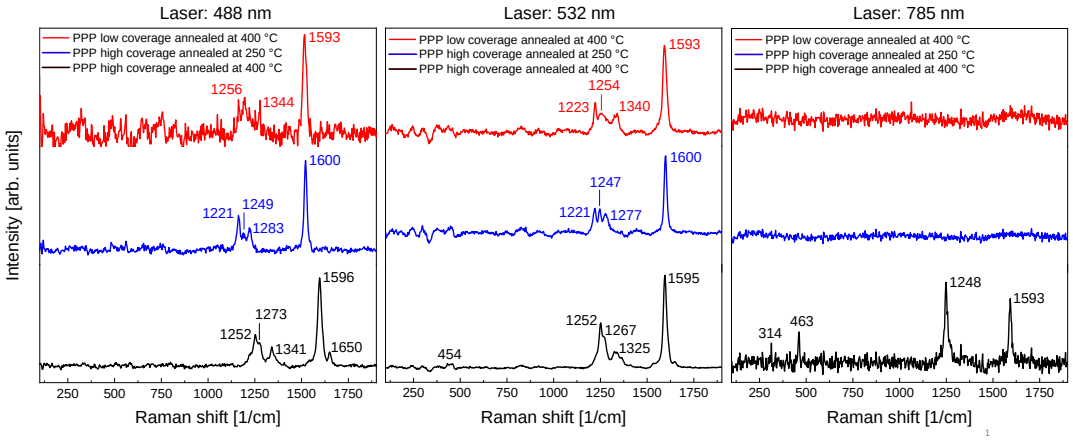

FIGURE 3.7: Raman spectra of low coverage PPP on Au(788) compared with high coverage PPP annealed at 250 °C and 400 °C on Au(788).

3.1.3 Raman spectroscopy of PPP transferred to Raman-optimized (RO) substrate

Raman study of high coverage PPP before and after substrate transfer

Two samples out of Figure 3.5 were selected to be transferred onto a Raman-optimized (RO) substrate. [88] As the targeted annealing process for the growth of 9-AGNR involves direct annealing to 400 °C in a single step after annealing at 200 °C, PPP directly annealed to 400 °C was chosen (see Section 3.1.2) because it also only involves one additional annealing step to 400 °C after the formation of PPP at 250 °C, therefore resembling the annealing protocol for the synthesis of 9-AGNRs. PPP annealed at 250 °C was used as a reference.

PPP annealed at 250 °C Figure 3.8 shows the Raman spectra of the high coverage PPP annealed at 250 °C. In Figure 3.6 and Figure 3.4 it was shown that no notable amounts of GNRs are present on the gold surface before the transfer. Since a Raman signal is obtained before and after transfer, it shows that sole PPP is transferable.
A convenient measure of the quality of the transfer is the evolution of peak width before and after transfer, as the change in width can be related to the presence of defects in the PPP (and in the fused PPP) or other intercalated molecules due to the transfer process. Table 3.1 shows the full width half maxima (FWHM) determined through a Lorentzian fit of the G peak on both substrates. In consideration of the FWHM of the G peak on Au(788) before transfer and after transfer on RO substrate shown in Table 3.1, the broadening is not significant since the values before and after transfer are comparable. Therefore, this points towards a successful transfer of PPP at high coverage as its structure appears to be widely conserved due to the absence of noticeable broadening.

	Au(788)	**RO Substrate**
488 nm	$(19.33 \pm 0.54)\ cm^{-1}$	$(19.60 \pm 0.81)\ cm^{-1}$
532 nm	$(17.90 \pm 0.41)\ cm^{-1}$	$(17.69 \pm 0.96)\ cm^{-1}$

TABLE 3.1: FWHM of the G peak obtained by a Lorentzian fit of the high coverage PPP sample annealed at 250 °C.

Because of the weak signal intensity on both substrates, no RBLM is seen even on the transferred sample, further supporting the claim that GNRs produced from the fusion of PPP are absent as PPP is only grown at 250 $°C$. Theoretical work on this subject predicted a value of around 720 cm^{-1} for the RBLM of PPP [119, 120]. We did however not detect any modes at this region for all investigated samples.

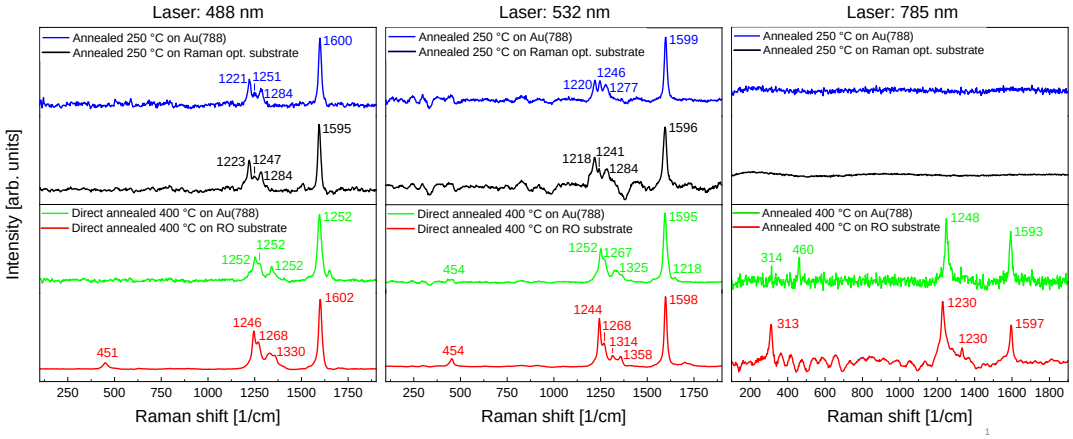

FIGURE 3.8: Raman spectra of high coverage PPP annealed at 250 $°C$ and 400 $°C$ on Au(788) before transfer and after transfer onto RO substrate.

PPP annealed at 400 $°C$ Figure 3.8 also shows the data acquired for high coverage PPP annealed at 400 $°C$ before and after substrate transfer. All Raman peaks are slightly blueshifted as a result of the change in interactions between the PPP and the RO substrate surface compared to the Au(788) surface. [76] Table 3.2 shows the FWHM of the G peak before and after substrate transfer for all employed lasers. With exception of the 785 nm laser, that shows similar FWHM before and after transfer, a remarkable decrease in peak width is observed. In regard to the maximal intensity of the G peak before and after transfer, the RO substrate significantly enhances the signal strength in the same manner the substrate has been shown to enhance the Raman intensity of GNRs. [88] These results demonstrate that the transfer of high coverage PPP annealed at 400 $°C$ is feasible and the transferred structures maintain their structural integrity.

	Au(788)	**RO Substrate**
488 nm	$(27.35 \pm 1.05)\ cm^{-1}$	$(20.69 \pm 0.59)\ cm^{-1}$
532 nm	$(22.74 \pm 1.09)\ cm^{-1}$	$(16.4 \pm 0.29)\ cm^{-1}$
785 nm	$(16.24 \pm 0.77)\ cm^{-1}$	$(16.84 \pm 1.29)\ cm^{-1}$

TABLE 3.2: FWHM of the G peak obtained by a Lorentzian fit of the high coverage PPP sample annealed at 400 $°C$.

A further observation for both the 488 nm and 532 nm laser is the appearance of the RBLM for 6-AGNR at 451 cm^{-1} (with 488 nm) and 454 cm^{-1} (for 532 nm) after transfer. Even though no RBLM is visible for the sample directly annealed to 400 $°C$ on Au(788) before the transfer (see Section 3.1.2), the data of the same sample after

transfer proves that 6-AGNRs are formed by the one-step annealing of PPP to 400 °C. Using the 785 *nm* laser is also possible to see the RBLM of the 9-AGNR after substrate transfer, showing that 9-AGNRs were also formed to some extent.
Due to the strong overlap of the modes within the region of the C-H and D peaks between 1200 cm^{-1} and 1400 cm^{-1}, individual peaks are difficult to detect. However, the individual C-H and D modes can be resolved better after the transfer due to the enhancement of the Raman signal by the RO substrate and the increased signal-to-noise ratio.

Raman study of low coverage PPP before and after transfer

Figure 3.9 shows the data acquired for the sample with PPP grown at low coverage annealed at 400 °C. Since this sample as shown in Figure 3.3 is grown with only one PPP ribbon per terrace, it is of special interest to analyse this sample in regard to the following experiments. Understanding the peak shapes and shifts of this sample might aid to make distinctions between the PPP signals and the signals of the 9-AGNR once they are both grown together.

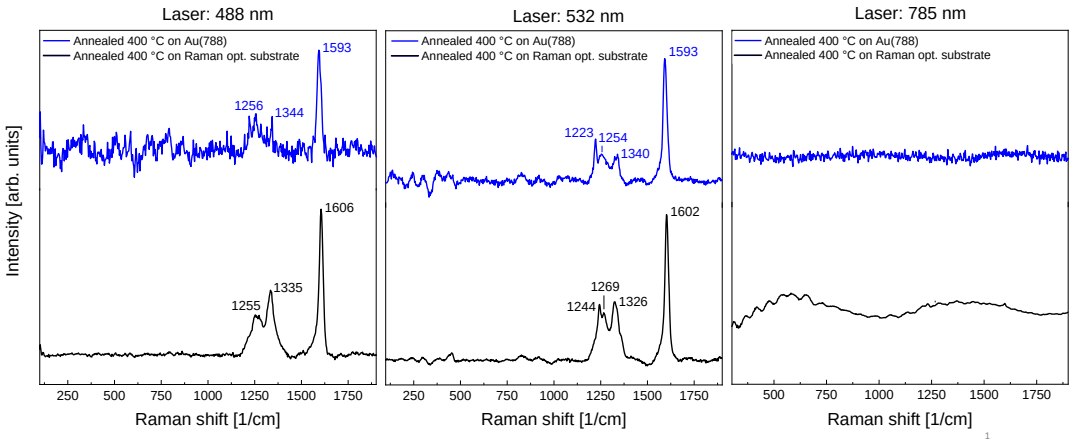

FIGURE 3.9: PPP at low coverage on Au(788) before transfer and after transfer onto RO substrate. The spectra for the 488 *nm* and the 532 *nm* laser are shown, while no signal was obtained with the 785 *nm* laser.

Similar to the observations on Au(788), no signal for the 785 *nm* laser was observed after transfer on the RO substrate because of the low amount of formed GNRs. The Raman spectra indicate an increase in signal intensity for the 488 *nm* laser after transfer to the RO substrate.

	Au(788)	**RO Substrate**
488 *nm*	$(30.46 \pm 3.30)\ cm^{-1}$	$(23.53 \pm 1.31)\ cm^{-1}$
532 *nm*	$(27.35 \pm 1.41)\ cm^{-1}$	$(23.47 \pm 0.89)\ cm^{-1}$

TABLE 3.3: FWHM of the G peak obtained by a Lorentzian fit of the low coverage PPP sample annealed at 400 °C.

The G peak is blueshifted for each laser after transfer due to the change in interaction between the PPP and the substrate on the RO substrate, as opposed to Au(788). Referring to the transfer of high coverage PPP, a blueshift was only observed for PPP

annealed at 400 °*C*, while PPP annealed at 250 °*C* showed a redshift. A blueshift is also observed for the low coverage PPP annealed at 400 °*C*, suggesting that the annealing at 400 °*C* could influence the observed Raman shift.
While the high coverage PPP annealed at 400 °*C* showed a higher relative intensity of the C-H relative to the D mode, the opposite is observed on the low coverage PPP annealed at 400 °*C* .

Comparison high and low coverage PPP annealed at 400 °C after transfer

Figure 3.10 shows a direct comparison between the high coverage and low coverage PPP annealed at 400 °*C* transferred to the RO substrate. This comparison emphasizes that no broadening of the G peak is observed, regardless of the coverage. The high coverage sample shows peaks in the C-H/D area more clearly, especially the modes at 1244 cm^{-1} and 1358 cm^{-1}. Upon closer inspection, these peaks however appear also on the low coverage PPP (slightly shifted). The main difference between for these two samples transferred to the RO substrate is the appearance of the RBLM of 9-AGNRs only for the high coverage PPP annealed at 400 °*C*.

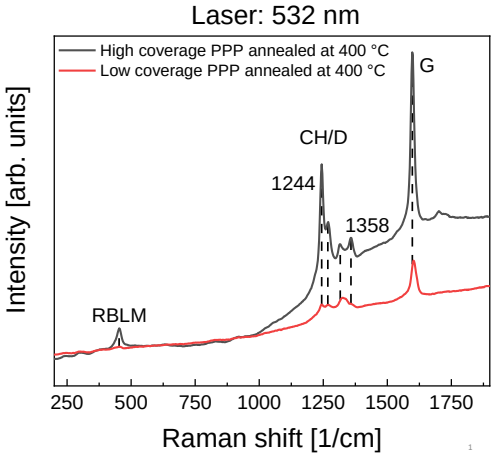

FIGURE 3.10: Comparison of the 532 *nm* laser Raman spectra of low coverage PPP annealed at 400 °*C* and high coverage PPP annealed directly to 400 °*C* both transferred to the RO substrate. To ensure that the peaks are not lost due to background subtraction, no background subtraction was done for these spectra.

Summarizing, we observed that even though diffusion occurs with low coverage PPP at 400 °*C* as shown by the STM measurements, significant amount of fusion only occurs on the high coverage sample. Moreover, we showed that PPP is transferred at high and low coverage.
The low coverage sample clearly shows high amounts of PPP present at the edges even after the annealing and thus could still prevent the growth of 9-AGNRs close to the edges.

3.2 9-Armchair Graphene Nanoribbons (9-AGNRs)

Following the analysis of the growth and effect of annealing at higher temperatures of the potential passivator PPP, it is worth examining the growth of 9-AGNR on Au(788) by itself. Since the properties of 9-AGNRs are well investigated, focus is laid primarily on the growth of the GNRs and the Raman spectroscopy at varying coverage. These preliminary investigations are necessary to ultimately understand the influence of the PPP once they are both grown together on the surface.

3.2.1 Growth of 9-Armchair Graphene Nanoribbons (9-AGNRs) on Au(788)

Figure 3.11 shows 9-AGNRs grown on Au(788) at low (**a**, **b**, **c**) and high (**d**) coverage. The 9-AGNRs were synthesized with a previously reported [80, 88, 121] two-step annealing process at 200 °C and 400 °C of the precursor DITP deposited at 67 °C (see Section 2.2.3). The annealing time for each step was 10 *min*. The deposition time was adjusted to optimize the coverage.
Figure 3.11 **a** depicts a sample with 9-AGNRs grown at coverage close to one 9-AGNR per step. To obtain this coverage, the precursor had to be deposited for 2.5 *min* at 67 °C prior to the annealing of the sample at 200 °C (for surface-assisted deiodization and polymerization) and 400 °C (for dehydrogenation and formation of the 9-AGNRs). On a first look, the 9-AGNRs not only seem to grow highly aligned with the step-edge of the Au(788) crystal, but also predominantly grow with a lateral separation between individual 9-AGNRs. Upon closer examination of the surface, Figure 3.11 **b** reveals that GNRs preferably grow along the step-edge first, while the terraces stay mostly unoccupied towards the center, which causes the inter-ribbon separation. This occurs due to the electronic structure of vicinal crystals facilitating adsorption of precursors at this location [122], likewise seen for the PPP as discussed in Section 3.1.1. The 9-AGNRs grown on the surface thus favourably stay close to the step-edge at low coverage.

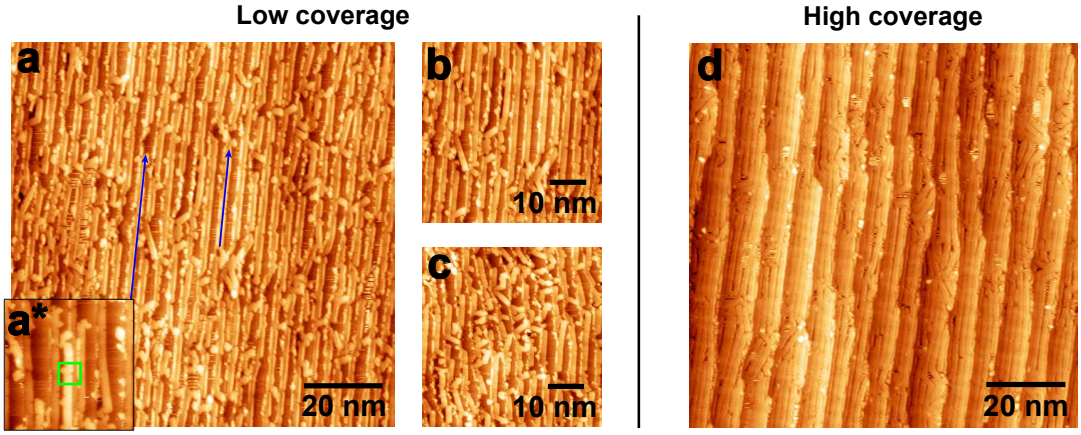

FIGURE 3.11: Growth of 9-AGNRs on Au(788) at high and low coverage. Measurement parameters for all shown images: Bias voltage: -1.5 *V*. 30 *pA*. **a**: Growth of 9-AGNRs on Au(788) at a low coverage of approximately one 9-AGNR per step. **a*** Close up image of 9-AGNRs grown on Au(788). A bite defect is highlighted found within a GNR, as highlighted by the green square. **b**: Close up of **a** with a majority of long GNRs, showing increased alignment. **c**: Close up of **a** with a majority of short GNRs, showing decreased alignment. **d** 9-AGNRs grown on Au(788) at high coverage.

As a consequence, the 9-AGNRs show a high degree of alignment along the direction of the steps. However, a minority of GNRs are observed that do not follow the step direction. The alignment of the GNRs strongly correlates with their length. Figures 3.11 **b** and **c** show close up images of the low coverage sample shown in Figure 3.11 **a**. In accordance to the observations on the PPP, the bulkiness of long GNRs prevents their rotation against the running direction of the terraces, while short GNRs may occasionally grow across the terrace. Note that the presence of such short ribbons is widespread, as shown by the GNRs growing out of alignment in the large area image Figure 3.11 **a**.
The growth of short GNRs significantly depends on the coverage. If only a low amount of precursor is deposited, the formation of long GNRs is prevented, hence leaving behind many short-grown ribbons. The same would happen if a slightly higher coverage than one GNR per step is found on the surface. Once the edges are occupied, the growth of the additional GNRs is initiated, which could be prematurely terminated if not enough precursors are present on the surface. This follows exactly the observations on the growth of PPP at varying coverage discussed in Section 3.1.1. The comparison of the step-edges between Figure 3.11 **b** and **c** indicates that areas with kinked terraces could influence the growth of the ribbons along the steps. The growth of ribbons in these areas may be hampered by the slight change of direction along the step-edge. Consequently, the growth of the GNRs might be prematurely terminated, resulting in the growth of numerous short ribbons around these areas.

Moreover, referring to the close up Figure 3.11 inset **a***, we see numerous indentations at the right side of the GNRs. These so-called *bite defects* [123] reflect a missing phenyl ring within the GNR. It is assumed these defects arise during the polymerization of the precursor due to an incomplete planarization of the phenyl rings on the gold surface. If one of the precursors is not completely planar with the gold surface, this misalignment may result in a desorption of one phenyl ring of the precursor during the polymerization, leading to the observed bite defects once the GNR is formed. In contrast, bite defects are entirely absent along the left side of the ribbons due to the step-edge of the gold burying the left edge of the GNRs as it reaches slightly over them.

Figure 3.11 **d** depicts the surface of Au(788) at high 9-AGNR coverage. Similar to the case of the PPP at high coverage, the surface is fully occupied with GNRs. The 9-AGNRs grow as close to each other as possible. However, in contrast to the PPP fusing at 400 $^{\circ}C$, the STM data suggests no fusion of 9-AGNRs at this temperature. This is further confirmed with the Raman study in Section 3.2.3. Although in the same way the alignment of the GNRs is largely increased due to increased abundance of precursors deposited on the Au(788) surface, there is still a minority of ribbons growing insufficiently long. The formation of short ribbons at high coverage could originate from a undesired dehalogenation of the precursor inside the crucible, mostly arising due to thermal stress. Thus, the deposited dehalogenated precursors cannot recombine with the intact precursors upon annealing, inducing an early termination of the growth of GNRs.

In summary, the growth of the 9-AGNRs highly resembles the growth of the PPP. At low coverage, the 9-AGNRs preferably grow along the step-edge and the length of the GNRs can be tuned by adapting the deposition time. The longer the GNRs grow, the higher the degree of alignment, which was equally observed with the PPP

samples. Additionally, at full coverage of the surface (1 monolayer) the alignment and length of the GNRs is optimized.
The similarities in the growth behaviour of PPP and 9-AGNRs is a promising indication that the edge-passivation of Au(788) with PPP is worth exploring because the passivator PPP needs to mimic the growth of the 9-AGNRs at low coverage. Since they share these properties, this might ultimately influence their growth and hence it remains exciting to explore.

3.2.2 Growth Statistics of 9-Armchair Graphene Nanoribbons (9-AGNRs) on Au(788)

Figure 3.12 **a** shows the sample prepared at the desired one 9-AGNR per step coverage. The sample was prepared by deposition of DITP at 67 $^{\circ}C$ for 3 *min* , followed by annealing a two-step annealing at 200 $^{\circ}C$ and 400 $^{\circ}C$ for 10 *min* each step.

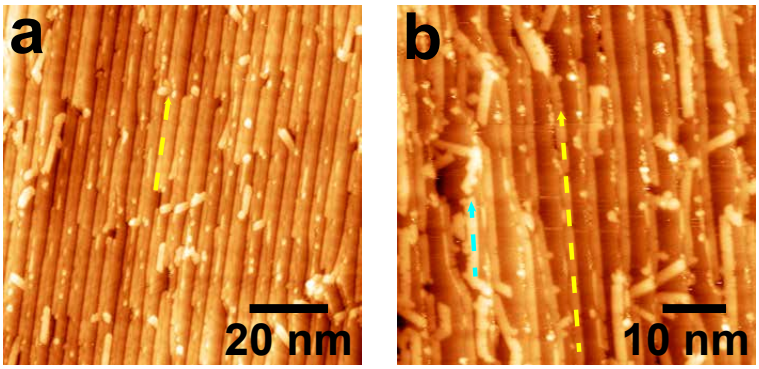

FIGURE 3.12: **a**: Image of the low coverage 9-AGNRs grown on Au(788) used for the growth statistics. A ribbon growing along the step-edge is highlighted with a yellow arrow. Bias voltage: -1.8 V. Current: 30 pA. **b**: Close up image of a similar sample at a slightly higher coverage. The two types of ribbons are highlighted: A GNR growing along the step-edge is highlighted in yellow and a GNR growing on top of the terrace is highlighted in blue. Bias voltage: -2.1 V. Current: 30 pA.

In comparison to Figure 3.11 the GNRs are less conspicuous because of an alteration in the tip. For that reason, a close up image of a similarly prepared sample is shown in Figure 3.12 **b**. As no close up images were taken for the sample in Figure 3.12 **a** used for the statistics, a previously prepared sample was taken as a reference. The deposition time for the preparation of this sample was slightly altered at 3 *min* 30 *sec* at a crucible temperature of 67 $^{\circ}C$. Figure 3.12 **b** shows the growth of long 9-AGNRs along the step-edge. Even though the difference in contrast between the GNRs located close to the edges and the Au(788) terraces is low, the presence of bite defects helps to make a distinction between the gold surface and the GNRs. Moreover, the zoom-in image (Figure 3.12 **b**) reveals that there is a tiny gap between the edges and the GNRs.
Note that GNRs growing along the edges can be easily distinguished from the GNRs on the terraces due to the difference in contrast. While the ribbons along the edges are darker, the ribbons on the terraces appear brighter. To facilitate accumulation of the data for the growth statistics, the GNRs are classified into two groups: First, the GNRs growing along the step-edge (dark contrast) and second the GNRs growing on

top of the terrace (bright contrast). This distinction will help to quantify the growth of the GNRs on the Au(788) surface. In Figure 3.12 **b**, the two types of GNRs are highlighted in different colors. The 9-AGNR growing along the step-edge is highlighted in yellow, while the 9-AGNR growing on top of the terrace is highlighted in blue.
In the following, the length of the ribbons for each group was counted from a set of 55 images. Note that the maximum length of the ribbons is restricted to the size of the image. Ribbons larger than 90 *nm* cannot fully be measured due to the size of the collected images scaled to 90 nm^2. GNRs growing out of the borders of the images were only considered if they exceed a length of 20 *nm*. GNRs growing out of the image range at a length below 20 *nm* were neglected.

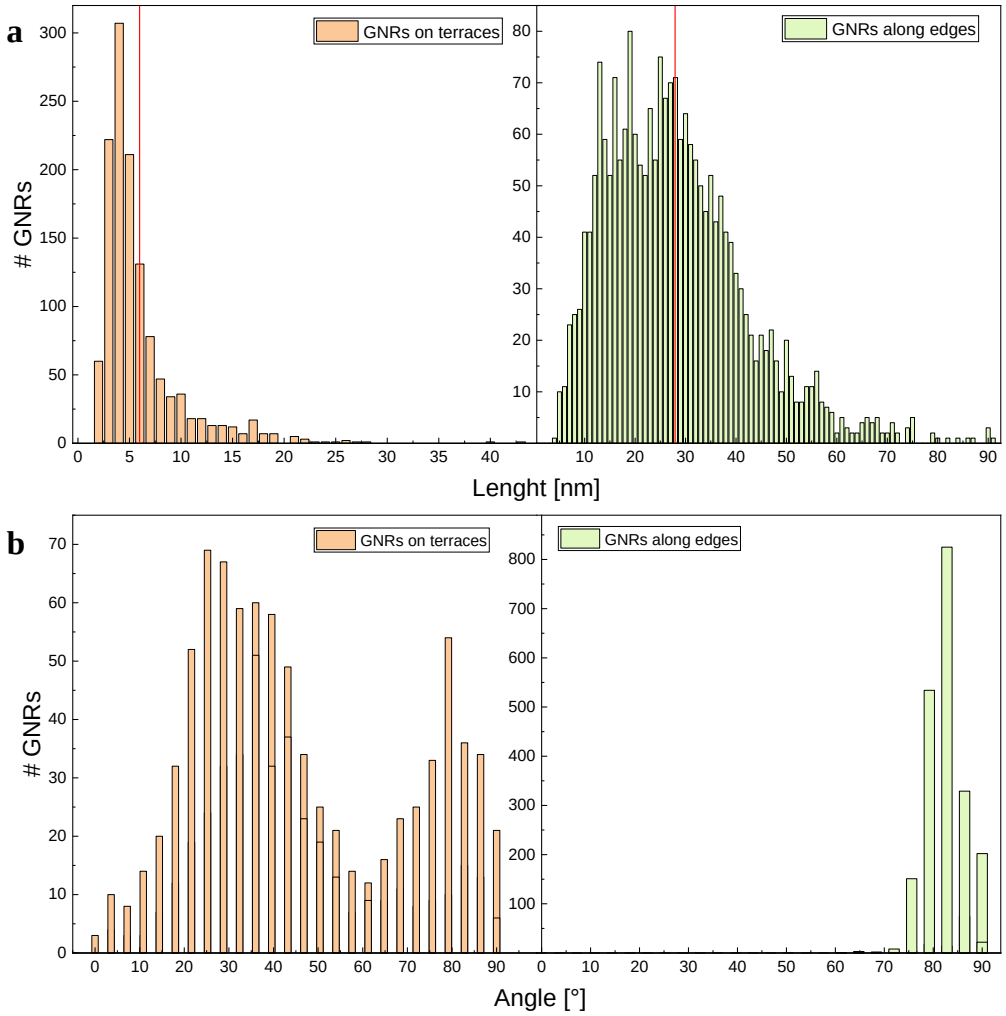

FIGURE 3.13: Growth statistics of 9-AGNR on Au(788) for a one 9-AGNR per step coverage. Row **a** Distribution of length of the ribbons either located towards the middle of the terraces or along the step-edge. The red line marks the average length of the GNRs of each group. Row **b** Angle distribution of the ribbons growing on the terraces compared to the ribbons growing along the edges.

The obtained statistics for the length distribution of the 9-AGNRs are shown in Figure 3.13 in Row **a**. At low coverage, the amount of GNRs growing along the steps is dominant. This is supported by the STM images as more ribbons with dark contrast

are present as opposed to ribbons with a bright contrast.
Additionally, the two groups show a significant difference in length. The histograms in Figure 3.13 **a** list the number of 9-AGNRs, for both grown on the steps and on the terraces, counted at a specific length. For GNRs growing on the terraces at this specific coverage, the distribution is leaning towards shorter length. Few GNRs are found to be as long as 42 *nm* and hence are growing along the direction of the terraces. The red bar in the histogram indicates the calculated average length of the 9-AGNRs, which is around 6 *nm*. Considering the device integration, in order to implement the GNRs into a device, the ribbons would have to be at least 20 *nm* long in order to bridge the device contacts. The data thus shows that these ribbons growing on top of the terrace are generally not able to bridge the contacts since only 1.4 % of all GNRs in this group are longer than 20 *nm* and consequently will not interfere the performance of the device.
The length distribution of the GNRs growing along the step-edge shifts towards a bimodal right skewed distribution with an average length of 28 *nm*. For this group of GNRs growing along the step-edge, GNRs with a length below 10 *nm* are quite seldom. Moreover, few GNRs span the whole image, reaching a length up to 90 *nm* (and would in reality be even longer). However, as highlighted by the histogram, the vast majority of GNRs are located in the regime from 10 *nm* to 60 *nm*. The statistics reveal that 68.8 % of all ribbons are reaching above 20 *nm*. Therefore, it is evident that the majority of GNRs growing along the step-edges at this coverage have sufficient length to bridge the source and drain channel as desired.
The bimodal shape with an indentation around 20 *nm* could originate from the assessment of the data because an artificial cut-off for the GNRs growing out of the border below 20 *nm* was introduced.

	GNRs along edges	**GNRs on terraces**
Total # GNRs	2184	1255
Avg. length [nm]	28	6
GNRs > 20 *nm* [%]	68.8	1.4
GNRs < 20 *nm* [%]	31.2	98.6

TABLE 3.4: Calculated values for the average length and amount of GNRs growing along the edges compared with the ones on the terraces. The values for the average length are rounded to the nearest whole number.

Figure 3.13 Row **b** lists the growth directions of the ribbons. As expected the angular distribution of the GNRs growing along the step-edges is very narrow. Since the terraces on the STM images are 90 ° rotated out of the x-axis, the data matches well with the STM images. It is evident that these long-grown ribbons cannot rotate away from the direction of the steps due to their bulkiness as argued with both the PPP and 9-AGNR STM observations. Few ribbons are rotated 70 °, managing to grow along the kinks of the terraces. Since only start and end points of ribbons are taken for the length measurements, the obtained value for the angle can sometimes be inaccurate. However, since no Raman polarization measurements were done of these samples, it is important to present this data because it helps us to gain further insights into the quantification of the STM measurements.
The GNRs growing on the terraces, on the other hand, show a far broader distribution of angles. Some ribbons are oriented perpendicular to the direction of the step-edge due to their short length. The distribution resembles a double Gaussian

distribution. Two local maxima are obtained at about 30 ° and 80 °. While most (short) ribbons are found to be oriented around 30 °, the ribbons growing at 80 ° can extend into longer ribbons since they are not influenced from the lack of space.
It is crucial to note that these directional statistics are not a direct measure of the overall alignment of the ribbons since these statistics ignore the length of the ribbons as a factor. As known from the length statistics, ribbons growing along the running direction of the terraces tend to extend further. This is also supported by the STM data for both the 9-AGNRs and the PPP. Although the collected data for the angular distribution of the GNRs located on the terrace scatters fairly randomly, in consideration of the length of the individual ribbons the alignment still shifts towards the direction of the step-edge.

The data provides evidence that the GNRs at low coverage preferentially grow along the steps with a high degree of alignment. Excess precursors form additional short ribbons located on top of the terrace. We observe the growth direction of short GNRs to be random, but once their length is increased they tend to follow the direction of the terrace.

3.2.3 Raman spectroscopy of 9-Armchair Graphene Nanoribbons (9-AGNRs) on Au(788)

Raman study of high coverage 9-Armchair Graphene Nanoribbons (9-AGNR) on Au(788)

To simplify the analysis of the samples with gradual growth of PPP and 9-AGNRs on Au(788) with Raman spectroscopy, it is valuable to first take a closer look at sole 9-AGNRs at high and low coverage with Raman spectroscopy. Since we already got a complete picture of the PPP annealed at varying temperatures, the following discussion will provide a good foundation to discuss the Raman analysis of the combined PPP + 9-AGNR samples.

Figure 3.14 depicts the Raman spectra collected for the high coverage sample shown in Figure 3.12 **d**. The spectra were acquired in vacuum with the 488 nm, 532 nm and 785 nm laser, as summarized in the figure.
The RBLM dependent on the GNR width appears with the 785 nm laser at 314 cm^{-1}. This matches with the expected Raman shift for the RBLM of 9-AGNRs. [76, 88] Moreover, as already observed for the RBLM of 9-AGNRs for the PPP samples annealed at 400 $°C$, this mode is only resonant with the 785 nm, while it is out of resonance with the 488 nm and 532 nm laser. A closer look at the regime of lower wavenumbers also reveals no other RBLMs for all lasers. Hence, the two step annealing at 200 $°C$ and 400 $°C$ of the precursor to grow 9-AGNRs does not cause the formation of other GNRs (i.e. through fusion). Under the assumption that fusion of 9-AGNRs would occur around the dehydrogenation temperature of 400 $°C$, 18-AGNRs would be formed, exhibiting a RBLM around 150 cm^{-1}. [86] Since this mode does not appear on the spectra, this indicates that fusion does not occur under these conditions, which is also underpinned by the STM data.

All lasers show a G peak located around 1595 cm^{-1} due to the sp^2-framework of the GNRs. However, in contrast to the PPP, we observe two G mode contributions for the 9-AGNRs using the 488 nm and 532 nm laser. In graphene, the splitting of the G peak is attributed to the longitudinal (LO) and transverse (TO) modes when

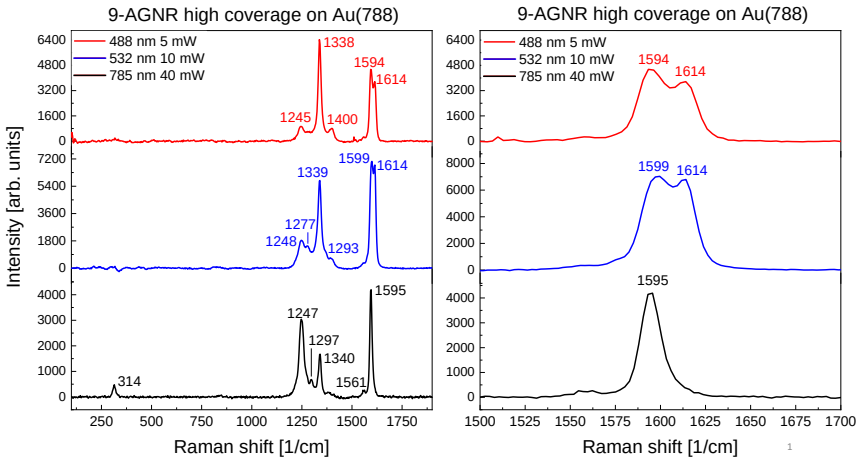

FIGURE 3.14: Left: Raman spectra of high coverage 9-AGNRs on Au(788) acquired with the 488 *nm*, 532 *nm* and 785 *nm* laser. Right: Close up of the G peak, resolving the LO and TO modes for the 488 *nm* and 532 *nm* laser. The 785 *nm* laser does not clearly resolve the separation between the LO and TO modes.

uniaxial strain is applied. [124] Due to the finite size and in-plane anisotropy of the 9-AGNRs, the splitting of the G peak is an intrinsic property. [43] As apparent by the Raman spectra, resolving the LO and TO modes is strongly dependent of the excitation energy. [43] While clear LO and TO modes are visible with 488 *nm* and 532 *nm*, only LO is observed with 785 *nm*.

Raman study of low coverage 9-Armchair Graphene Nanoribbons (9-AGNRs) on Au(788)

Since the targeted coverage of 9-AGNR for the growth and transfer together with PPP should be only one 9-AGNR per terrace on Au(788) (in order to reduce the lateral leakage current that would otherwise be present at high coverage GNRs upon device integration) we further investigated the Raman spectra of low coverage 9-AGNRs.
In this respect, Figure 3.15 shows a comparison between the high coverage and low coverage (one 9-AGNR per terrace) on Au(788) with Raman spectroscopy. The low coverage data shown is used under the permission of Rimah Darawish, as we did not manage to acquire a low coverage 9-AGNR spectrum in the given time frame.
No shift of the G peak located around 1600 cm^{-1} for all lasers is observed with low coverage. The LO and TO components are also observed at 1600 cm^{-1} and 1616 cm^{-1} using the 488 *nm* laser (only LO was resolved using 532 *nm* and 785 *nm*). The difference in experimentally resolving the G modes between high and low coverage can be a result of varying coverage, but also of a change in measurement parameters that were different for each sample. The RBLM for 9-AGNR at 314 cm^{-1} resonant with the 785 *nm* is also present at low coverage with no significant shift.

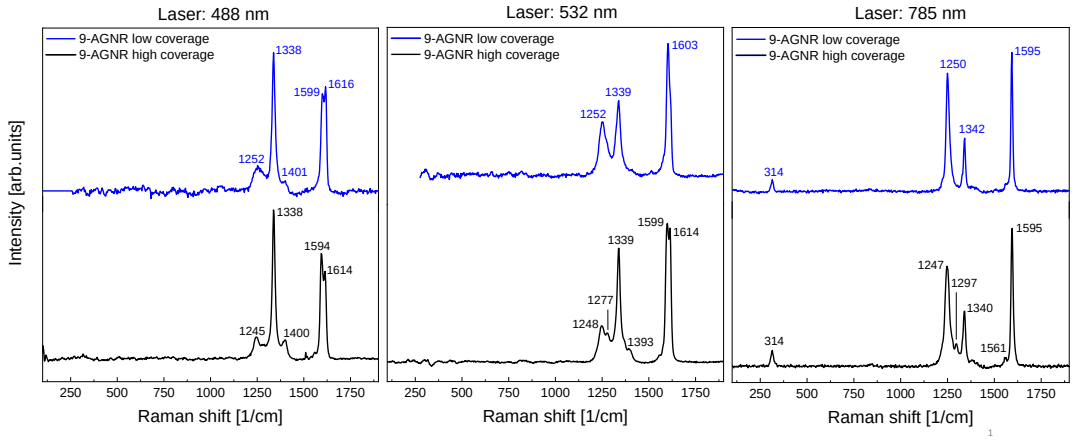

FIGURE 3.15: Raman spectra of high and low coverage 9-AGNR grown on Au(788) measured with the 488 *nm*, 532 *nm* and 785 *nm* laser.

3.2.4 Raman spectroscopy of low coverage 9-Armchair Graphene Nanoribbons (9-AGNRs) transferred to Raman-optimized (RO) substrate

Raman study of low coverage 9-Armchair Graphene Nanoribbons (9-AGNR) before and after transfer

Although the transfer of PPP to the RO substrate was successful at both high and low coverage, the feasibility of transferring 9-AGNRs has been shown (Darawish et al., in preparation, 2021) to depend strongly on the coverage. When transferring 9-AGNRs grown on Au(788) at a high coverage to the RO substrate, no significant broadening of the Raman peaks is observed. This is an indication that the 9-AGNRs are transferred uniformly at high coverage, which is the ultimate goal for device integration. The lack of broadening paired with the high yield of devices suggests that the 9-AGNRs at high coverage are transferred like a film and therefore are not as prone to get damaged during the transfer. [121]

It is however the aim to grow and transfer the 9-AGNRs on Au(788) at low coverage with a coverage of a single 9-AGNR per step as discussed in Section 3.2.2.
Previously, multiple transfers of 9-AGNRs at low coverage have been performed, the resulting Raman spectra on the RO substrate after the transfer have shown to exhibit significant broadening especially around the C-H/D peaks. Out of 21 low coverage 9-AGNR substrate transfers performed in 2019 only 7 spectra with good quality were obtained, resulting in a predicted yield of 33.3 % (statistics collected by Rimah Darawish over several transfers). This comprises the motivation to attempt the improvement of the transfer by investigating the growth of 9-AGNRs on Au(788) edge-passivated with PPP because the low yield of well transferred GNRs at low coverage is far from ideal to work reliably towards device integration.

A successfully transferred sample of 9-AGNRs grown at low coverage is shown in Figure 3.16. The data is used under the permission of Rimah Darawish.
Note that no noticeable shift and the same modes are observed after transfer to the RO substrate compared to Au(788) regardless of the laser employed for the measurement. Reflected by the increase in intensity and the increased signal-to-noise ratio for the 488 *nm* and 532 *nm* spectra, the transfer shown in Figure 3.16 indeed reflects

a successful transfer. For both the 488 nm and the 532 nm laser, the transferred 9-AGNRs show no significant broadening around the G peak or around the C-H/D peaks. However, while the LO and TO modes of the G peak are resolved using the 488 nm laser on Au(788) before the transfer, only the LO mode is observed on the RO substrate. Note however that the spectra shown before the transfer in Figure 3.16 do not correspond to the same sample shown after transfer, these changes could also be related to variations in the sample or the measurement parameters. Additionally, we see exclusively with the 785 nm the RBLM of 9-AGNR at 314 cm^{-1} both before and after transfer.

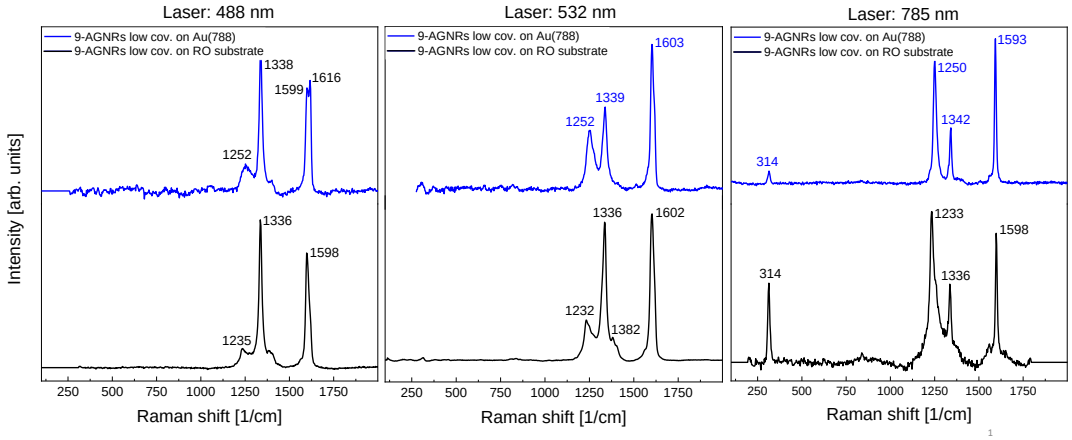

FIGURE 3.16: Raman spectra of low coverage 9-AGNRs on Au(788) before transfer and after transfer on RO substrate acquired with the 488 nm, 532 nm and 785 nm laser.

It is once again important to emphasize that the data shown in Figure 3.16 does not provide an accurate representation of the majority of low coverage 9-AGNR transfers. Figure 3.17 shows a comparison of a well and a poorly transferred sample with Raman spectroscopy. The poorly transferred sample shows significant broadening around the C-H/D peak, suggesting the induction of damage when transferring low coverage 9-AGNRs. It is therefore important to highlight that transfer quality of 9-AGNRs shows a strong coverage dependence, with improved transfer quality at high coverage. In comparison with the PPP samples, we did not observe such a trend. The spectra of low coverage PPP did not exhibit significant broadening after transfer. Note however that we did not have any statistical insights into the transfer quality of low coverage PPP, wherefore we can not directly conclude if a coverage dependence on the transfer quality is present or not.

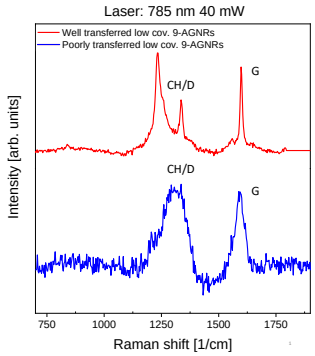

FIGURE 3.17: Comparison with Raman spectroscopy of one well and one poorly transferred low coverage 9-AGNR sample acquired with the 785 nm laser.

All observed modes of the 9-AGNRs strongly overlap with the modes of PPP. The main difference however between the PPP and the 9-AGNRs is that we sharp peaks are still observed with the 785 *nm*, whereas the PPP shows no signal with this laser. Therefore, the difference in the optical gap between the PPP and 9-AGNR can be advantageous to filter out the 9-AGNRs from the PPP, which is beneficial in regard to the measurements on the combined 9-AGNR + PPP sample that will be discussed in the following.

3.3 9-AGNR on Au(788) edge-passivated with PPP

3.3.1 Growth of 9-AGNR + PPP on Au(788)

All experiments conducted so far dealt with the growth of only a single molecular species at a time. Although we proved that the PPP at low coverage is largely resistant towards increased temperatures, it is yet to be investigated how the growth of PPP wires is influenced when it is annealed together with the precursors of the 9-AGNR. Due to the diffusion of PPP (see Figure 3.2), the 9-AGNR might replace or fuse with the PPP at the step-edges and prevent the passivation from happening. Thus, in the following the growth of low coverage 9-AGNR on the Au(788) with PPP is analysed.

Figure 3.18 shows the surface of Au(788) with one PPP wire grown per step (deposition of DBTP at 102 $°C$ for 2 *min* 35 *sec*, followed by a single annealing step at 250 $°C$), followed by the deposition of low coverage 9-AGNR (deposition of DITP on the same surface at 67 $°C$ for 3 *min* and subsequently annealed at 200 $°C$ and then 400 $°C$ for a 10 *min* holding time on each step). To facilitate the distinction between the PPP and 9-AGNR, the GNRs were grown at a coverage below one ribbon per step. The STM image reveals immediate differences for both the PPP and the 9-AGNR. In contrast to the low coverage PPP annealed to 400 $°C$, when grown together with 9-AGNR the PPP appears to stay intact over larger spread and the PPP diffusion from the step-edges is strongly reduced.

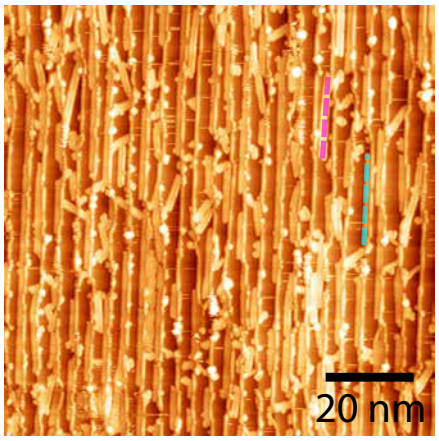

FIGURE 3.18: STM image of one PPP grown per step, followed by the growth of one 9-AGNR per step, on Au(788). Bias voltage: -1.8 V. Current: 30 pA. A ribbon growing along the step-edge is highlighted with blue and a ribbon growing on top of the terrace is highlighted in pink.

Adjacent to the PPP, we see growth of 9-AGNRs, providing a first indication that it is possible to grow 9-AGNRs with the presented protocol together with PPP on the same Au(788) surface. In Section 3.2.1 the contrast of the 9-AGNRs growing on top of the terrace was mentioned to be brighter as opposed to the ribbons located along the step-edge. The direct comparison of the two surfaces (see Figure 3.21 in Section 3.3.3) reveals a significant difference in the amount of ribbons with brighter contrast. To quantify this, growth statistics of a sample grown at an exact one per terrace coverage of both PPP and 9-AGNR are conducted in Section 3.3.2.

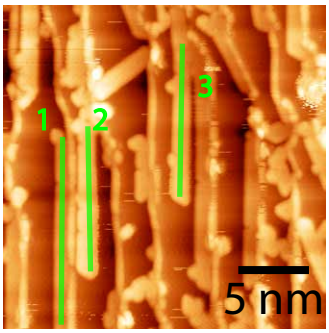

FIGURE 3.19: Close up STM image of one PPP per step grown on Au(788), followed by the growth of 9-AGNR slightly below a coverage of one 9-AGNR per step. The gaps suggest the absence of fusion. Bias voltage: -2.1 V. Current: 30 pA.

In Figure 3.19 9-AGNRs growing in a distinct fashion together with PPP [3] are highlighted. GNR **1** represents a ribbon growing close to the step-edge, distinguished by its dark contrast. As previously mentioned in Section 3.2.1, part of these GNRs are buried under the step-edge from the terrace above. Since the PPP is growing along the edge of the terrace above, it cannot prevent the growth of the GNRs along the edge at this location. GNR **2** on the other hand is growing on top of the terrace. It appears that the GNR grows directly adjacent to the PPP and it is apparent that no fusion occurs because the bite defects within the 9-AGNR are visible. GNR **2** shows brighter contrast as it grows on the terrace. GNR **3** shows a ribbon growing close to a second GNR (shown in the STM with darker contrast). The two GNRs are also not fused, noticeable by the gap between them. The ribbon **3** grows towards the center of the terrace since the step-edge is already occupied by another ribbon.

On closer examination of the STM images, PPP is promising to act as a passivator. Even when grown together with the 9-AGNRs, the PPP remain close to the step-edge and no fusion occurs at the cyclodehydrogenation temperature. This results on the growth of 9-AGNRs towards the center of the terrace which could ultimately influence the substrate transfer.

3.3.2 Growth statistics of 9-AGNR + PPP on Au(788)

In the following, the growth statistics of the GNRs on the PPP passivated surface of Au(788) is discussed. Similarly to Section 3.2.2 the GNRs are separated in two groups: the ribbons growing on top of the terrace and the ribbons growing along the step-edge. The data was collected from 58 distinct STM images. The images were taken at a scale of 90 nm^2. 9-AGNRs growing out of the image range were only considered if they exceed the length of 20 nm.

Figure 3.20 Row **a** right shows the length of the 9-AGNRs growing along the step-edge next to the PPP (generally dark contrast in the STM images). Table 3.5 shows a selection of values calculated from the data of the histogram being insightful for the discussion. The histogram resembles a Gaussian distribution with an elongated right tail. The average length of the 9-AGNRs in this group amounts to 22 nm, represented by the red line. Most GNRs are found to be in the range from 5 nm to 60 nm. The maximal length observed for a single ribbon is at 82 nm. Considering the aspect of device integration, only 52.3 % of all 9-AGNRs growing along the step-edge exceed the length of 20 nm and thus could bridge the contacts as desired. Similarly to the observations on the pure 9-AGNR growth statistics, the distribution adopts a bimodal shape. As the indentation is around 20 nm as previously observed, this supports the claim that this arises because 9-AGNRs that are growing out of the image

[3] To facilitate the distinction between the 9-AGNRs and the PPP, the coverage of 9-AGNRs was lowered slightly below a one ribbon per step coverage. The deposition time was lowered to 2 *min* 30 *sec* at 67 °C.

are only considered if they exceed a lenght of 20 *nm*, causing a shift in the distribution.

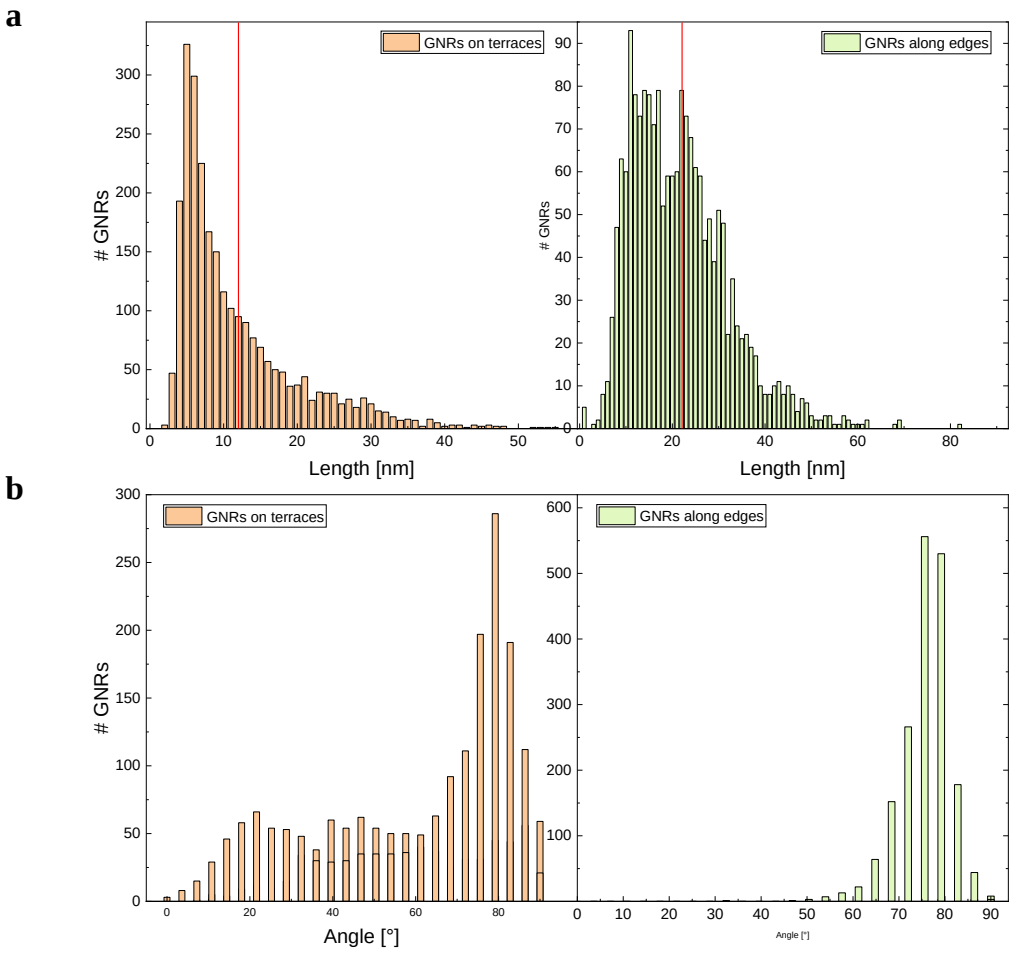

FIGURE 3.20: Growth statistics of 9-AGNR on Au(788) edge-passivated with PPP for a one 9-AGNR per step coverage. Row **a** Distribution of length of the ribbons either located towards the middle of the terraces or along step-edge. The red line highlights the average length for each group of ribbons. Row **b** Angle distribution of the ribbons growing on the terraces compared to the ribbons growing along the step-edges.

A histogram with the acquired growth data for the GNRs growing on the terrace is shown in Figure 3.20 Row **a** on the left. The distribution takes in a right-skewed shape. At a length of 5 *nm* the maximal amount of 9-AGNRs at a specific length is counted. The average length for the ribbon growing on the terraces is 12 *nm*. Although the ribbons on top of the terrace are shorter compared to the ribbons growing along the step-edge, which is in accordance with the previous considerations of both sole PPP and 9-AGNR, we observed few GNRs longer than 50 *nm*. In total only 16 % of all ribbons grow above the length of 20 *nm*, the vast majority of this group cannot be used for the implementation into device.
The angular distribution in Figure 3.20 Row **b** reveals a lot of similarities with the distribution for sole 9-AGNR. The angular distribution of GNRs growing along the

	GNRs along edges	**GNRs on terraces**
Total # GNRs	1854	2558
Avg. length [nm]	22	12
GNRs > 20 *nm* [%]	52.3	16.0
GNRs < 20 *nm* [%]	47.7	84.0

TABLE 3.5: Calculated values for the average length and amount of GNRs growing along the edges compared with the ones on the terraces. The values for the average length are rounded to the nearest whole number.

step-edge, as depicted in Figure 3.20 Row **b** (right-hand side), deviate further from the direction of the terrace as compared to the sole PPP sample. The maximum of this distribution is located at 80 °. This is however in accordance with the alignment of the terrace, as the data was accumulated over an area where most images were not directly perpendicular with the x-axis on the STM image. The increase in broadness of the distribution of the GNRs growing along the step-edge compared to sole 9-AGNRs could arise from both the presence of PPP and kinks within the terraces. While it is clear that kinks in the terrace cause the GNRs to grow tilted relative to the direction of the terraces, the interaction between the GNRs and the step-edge might be slightly altered due to the presence of PPP and the GNRs therefore would not necessarily grow directly aligned with the step-edge.

The angular distribution of the GNRs growing on top of the terraces seen in Figure 3.20 Row **b** (left-hand side) shows the GNRs are rotated in all possible directions, with a maximum at 80 °. Therefore, the majority of GNRs growing on top of the terraces still show a high degree of alignment of the step-edge. As discussed in the case of sole 9-AGNR (see Section 3.13) the broadness arises due to the short 9-AGNRs growing in arbitrary angles across the step-edges.

3.3.3 Comparison of growth statistics of 9-AGNR/9-AGNR + PPP on Au(788)

Figure 3.21 shows an STM comparison of low coverage 9-AGNR with low coverage 9-AGNR + PPP on Au(788). In the following, we discuss the direct comparison of the growth statistics of these samples, as summarized by the growth histograms of 9-AGNRs grown on the sole 9-AGNR sample and of 9-AGNRs grown on the 9-AGNR + PPP sample shown in Figure 3.22. Since the total number of ribbons counted varies between the two samples, the data was normalized [4] accordingly for each sample. This normalization facilitates the direct comparison of the magnitudes for the two resulting distributions.

Figure 3.22 top left depicts the GNRs growing along the edges on both samples. The two distributions for these GNRs have a very similar shape. Since the GNRs growing along the step-edge on the sole 9-AGNR sample has a higher magnitude compared to the 9-AGNR + PPP sample at every length, it suggests that sole 9-AGNRs promotes the growth of GNRs close to the step-edge. The PPP also directly affects the length of ribbons growing close to the step-edge. While GNRs extending over 90 *nm*

[4]The data was normalized dividing by the integral of the histogram of both GNR on terraces and GNRs along edges for one sample. As the width of one column in the histogram is 1 *nm*, the area is calculated by summation of all GNRs. Therefore, the normalization in this case was done by dividing the total number of ribbons.

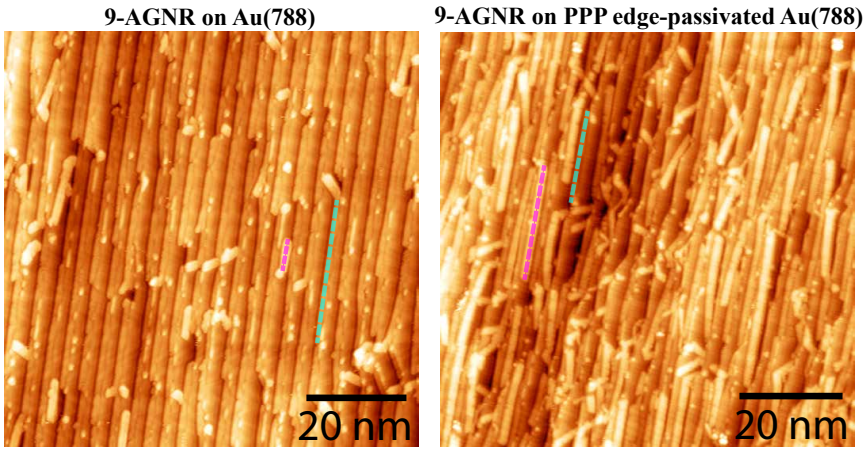

FIGURE 3.21: **Left**: 9-AGNRs grown on Au(788). A ribbon growing along the step-edge is highlighted in blue. Bias voltage: -1.5 V. Current: 30 pA. **Right**: 9-AGNRs grown with PPP on Au(788). A ribbon growing along the step-edge is highlighted in blue and a ribbon growing on top of the terrace is highlighted in pink. Bias voltage: -1.6 V. Current: 30 pA.

are found on the sole 9-AGNR sample, the 9-AGNR + PPP sample only shows few GNRs with a length over 50 nm.
Figure 3.22 top right shows the comparison for the growth of GNRs on top of the terraces for both samples. As expected by the observations on the previous graph, the GNRs growing on the terrace of the PPP passivated surface are present in significantly higher amounts than for the sole 9-AGNR sample. The average length of the GNRs growing on the terrace (12 nm) (see Figure 3.23) is significantly higher for the PPP-passivated sample compared to sole 9-AGNR (6 nm). As seen by the histogram, the sample shows a promising increase in the amount of ribbons longer than 20 nm as desired, while only few ribbons over 20 nm are present on the unpassivated sample.
The increased average length of the GNRs growing on top of the terrace also explains the occurrence of only one maximum on the angular distribution for the 9-AGNR + PPP sample (see Figure 3.20) compared to the bimodal angular distribution observed for the GNRs growing on top of the terrace of the sole 9-AGNR sample (see Figure 3.12). We observe a larger ratio of longer ribbons growing on top of the terrace which in consequence increases their growth orientation.

This data provides further insights on the effect of PPP on the growth of 9-AGNR on the surface. As already depicted by the STM image (Figure 3.21), the presence of the PPP at the step-edges significantly increases the relative amount of GNRs growing on top of the terrace with an increased length. The PPP seems to template the growth of GNRs both in alignment and length, leading to a significant decrease in the overall percentage of the ribbons above 20 nm and a slight decrease in alignment for the ribbons growing along the step-edge compared to the 9-AGNRs growing alone. Although the ribbons growing on top of the terrace grow longer in average compared to the sole 9-AGNR sample, they are still relatively short in comparison with the length of the ribbons growing along the step-edge with PPP. In this regard, direct comparison of the average length for the ribbons along the edges in Figure 3.23 visualizes that the PPP passivation also leads to a decrease in the average length of

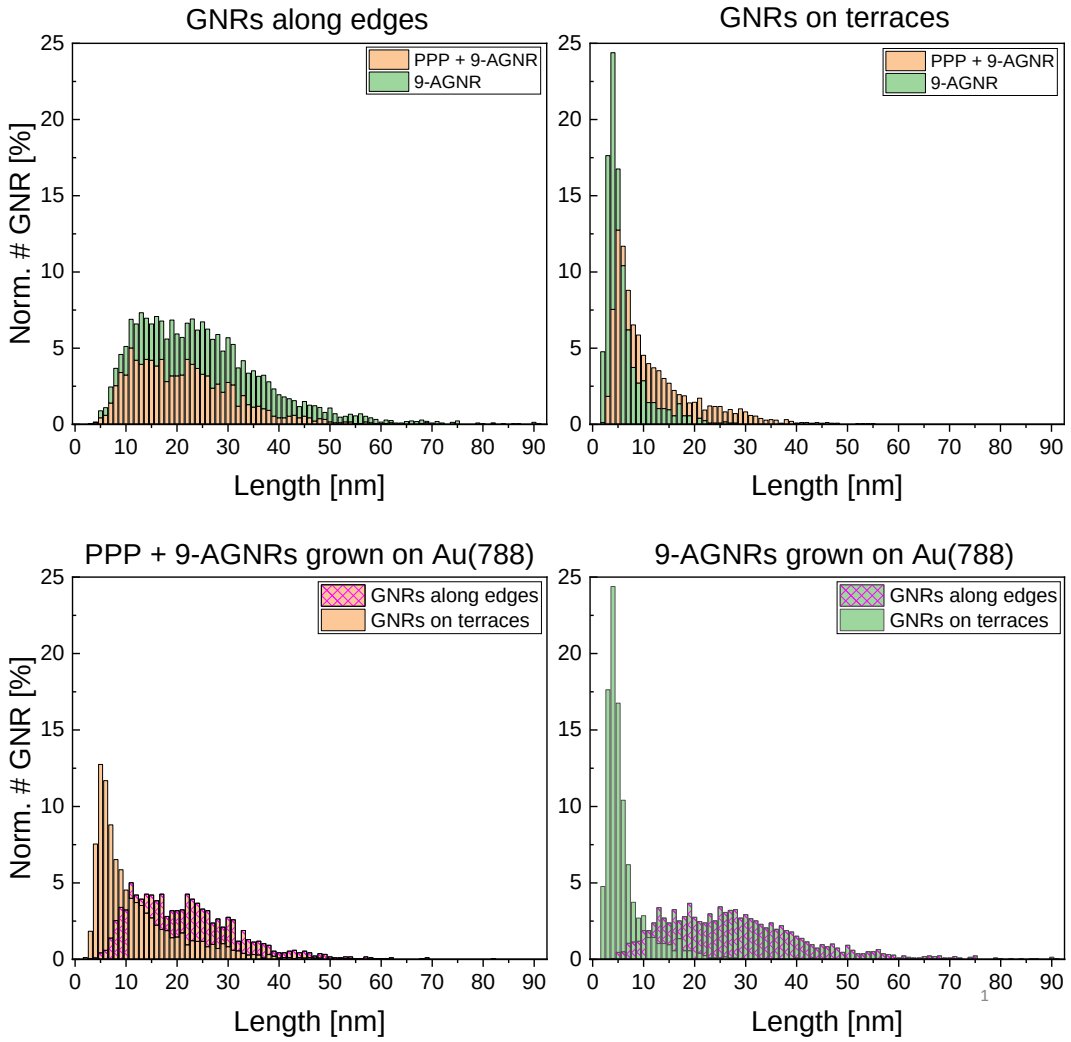

FIGURE 3.22: Comparison of 9-AGNRs growing along edges and GNRs growing on top of the terraces both with and without PPP.

the ribbons growing along the step-edge with PPP-passivation compared to sole 9-AGNRs.
The PPP however seems to be successful as an edge passivator since it promotes the growth of ribbons towards the center of the Au(788) terraces. Consequently, this could make the transfer of these ribbons more reproducible as the strong adhesion of the ribbons to the step-edge should be decreased by the presence of PPP.

Even though the relative amount of 9-AGNRs on top of the terrace spreading over 20 *nm* increases significantly on the PPP passivated surface, only 16.0 % reach this desired length. Therefore, an optimization of the length of the ribbons on the terrace would be required. Since the same coverage was used as for the sample grown with one 9-AGNR per terrace, an increase in coverage could aid to further elongate the ribbons on top of the terrace. On the other hand, an increase in coverage could lead to a decrease in device performance, requiring a compromise between length and density..

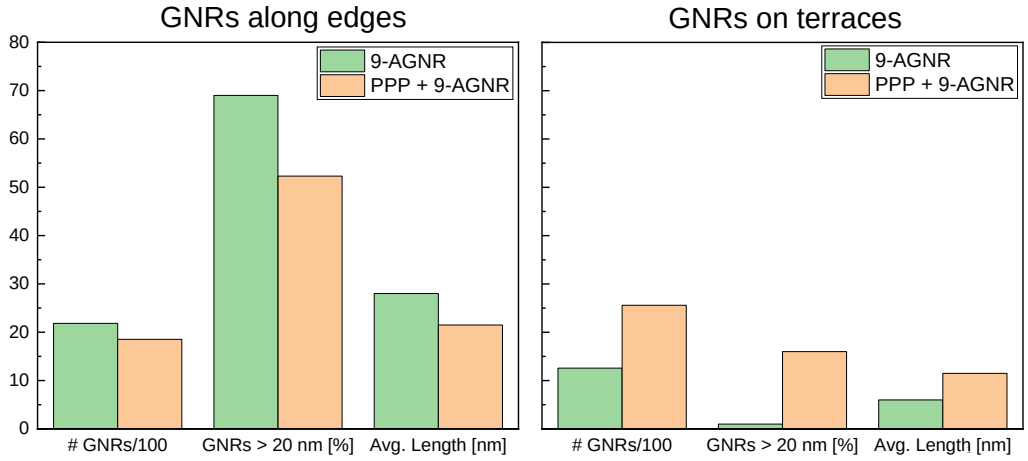

FIGURE 3.23: Comparison of useful values for the assessment of the 9-AGNR growth on both the PPP-passivated and unpassivated Au(788) surface.

3.3.4 Raman spectroscopy of 9-AGNR + PPP on Au(788)

Raman study of high coverage 9-AGNR + one PPP per step-edge

Figure 3.24 depicts high coverage 9-AGNR grown together with one PPP wire per step-edge on Au(788). In comparison to the Raman studies on the sole PPP and 9-AGNR samples, we now deal with samples that are intrinsically a mixture of PPP and 9-AGNR grown on the same sample. In the following, we therefore usually refer to the sole PPP and 9-AGNRs at the dedicated coverage. In this respect, Figure 3.24 also shows pure 9-AGNR grown at high coverage and PPP grown at low coverage accordingly, therefore facilitating the comparison with the combined 9-AGNR + PPP sample.

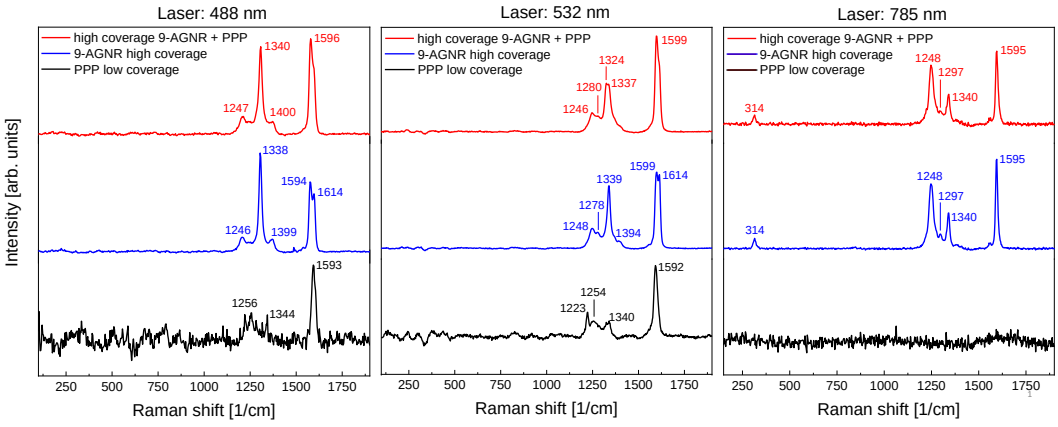

FIGURE 3.24: Raman spectra of high coverage 9-AGNR + PPP on Au(788) measured with the 488 *nm*, 532 *nm* and 785 *nm* laser. 9-AGNRs grown at high coverage and PPP grown at low coverage on Au(788) is used as a reference.

The Raman spectra of high coverage 9-AGNR + PPP look nearly identical to the high coverage 9-AGNR. Not only do we see a G peak at 1596 cm^{-1} indicating a comparable shift between the 9-AGNR + PPP and sole 9-AGNR sample established by the

sp^2-lattice of both the PPP and the 9-AGNRs, but we also obtain nearly identical peak shapes and shifts in the regime of C-H and D modes (between 1200 cm^{-1} and 1450 cm^{-1}). The increased amount of 9-AGNRs compared to PPP appears to overshadow the PPP that was only grown as a single wire along the step-edge. With the 785 *nm* laser, there are no deviations for the high coverage 9-AGNR + PPP sample and the high coverage 9-AGNR sample due to previous observations that the PPP is not resonant with this laser.
Additionally, as seen on the 9-AGNR samples and the PPP annealed at 400 $°C$, we see the GNR-width-dependent RBLM of 9-AGNRs at 314 cm^{-1} resonant exclusively with the 785 *nm* laser. The RBLM likewise does not show a shift on the combined 9-AGNR + PPP sample at high coverage relative to the sample with only 9-AGNR at high coverage.
With the 488 *nm* and 532 *nm* laser, the LO and TO phonon modes of the G peak on the 9-AGNR + PPP sample is not as pronounced compared to sole 9-AGNRs. This probably arises due to a difference in coverage between the 9-AGNR + PPP and only 9-AGNR sample because the occupation of the edges by PPP could lead to a decrease in space for the 9-AGNRs to grow at high coverage.

The high resemblance of the high coverage 9-AGNR + PPP sample with the high coverage 9-AGNR proves that it is possible to grow 9-AGNRs together with PPP on Au(788), as supported by the STM images of low coverage 9-AGNR + PPP [5] (see Figure 3.18). Moreover, fusion between the 9-AGNRs and the PPP along the edges when annealing at 400 $°C$ can be excluded because the RBLM for 12-AGNRs predicted around 260 cm^{-1} [86] is absent with all lasers. As the fusion would defeat the purpose of the passivator, the present Raman data shows that the growth of high coverage 9-AGNRs is not hindered by the presence of PPP.

Raman study of low coverage 9-AGNR + one PPP per step-edge

The observations on the high coverage 9-AGNR + PPP samples aided us to confirm that is it possible to grow 9-AGNRs gradually on the same Au(788) as the passivator PPP. Furthermore, the obtained Raman spectra showed that the PPP does not visibly interfere with the 9-AGNR grown at a high coverage.
As the potential coverage for improving device performance would ideally be a single GNR per step-edge, we further investigate the Raman spectra of low coverage 9-AGNRs + PPP, depicted in Figure 3.25. It is important to note that the coverage of 9-AGNRs on this sample is slightly lower than the sample with an optimized coverage that was used for the growth statistics (see Figure 3.18). For the 785 *nm* laser, as reflected by the low signal-to-noise ratio for the low coverage 9-AGNR + PPP sample, we did not manage to obtain a high quality spectrum due to issues with the laser settings. Nevertheless, according to the observations at high coverage, we expect the signal to strongly resemble the 9-AGNR spectrum at low coverage. The C-H and D modes of the low coverage 9-AGNR with the 532 *nm* laser differ from the shape usually observed, as the D mode should exhibit a higher intensity relative to the C-H mode (see high coverage 9-AGNR in Figure 3.24).

While we did not observe any shifts on the high coverage 9-AGNR + PPP sample, a slight redshift of the G peak at 1593 cm^{-1} relative to the low coverage 9-AGNR

[5] Due to an issue with the STM, there is a lack of STM images that can be shown for high coverage 9-AGNR + PPP. We do however not expect the growth of high coverage 9-AGNR with PPP on Au(788) to be significantly different compared to the growth of sole 9-AGNRs at high coverage.

+ PPP is apparent with the 488 nm and 532 nm laser. Comparison with the G peak of the low coverage PPP at 1592 cm^{-1} shows that the G peak of the 9-AGNR + PPP sample shifts more closely towards the G peak of PPP, opposed to the G peak of pure low coverage 9-AGNR at 1599 cm^{-1}. This shift disappears when measuring with the 785 nm laser because the laser is exclusively resonant with the 9-AGNRs and thus cannot be influenced by the PPP.

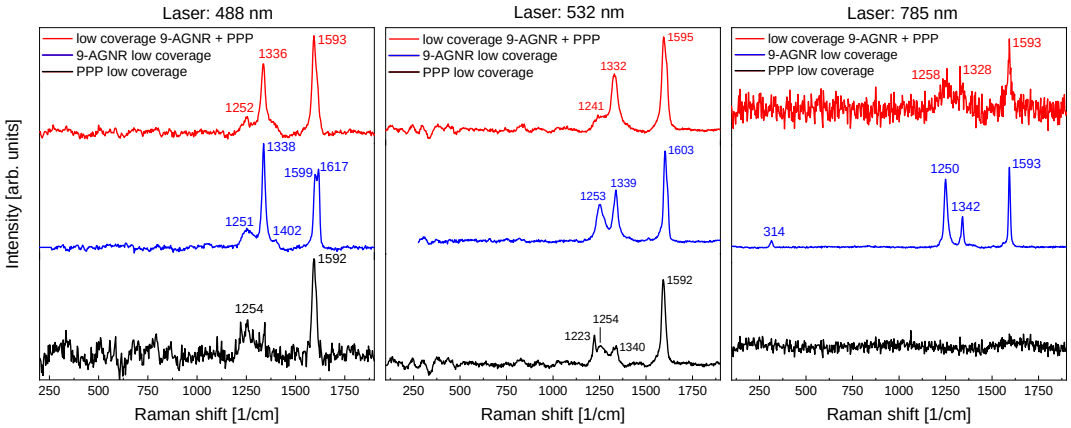

FIGURE 3.25: Raman spectra of low coverage 9-AGNR + PPP on Au(788) measured with the 488 nm, 532 nm and 785 nm laser. 9-AGNRs grown at low coverage and PPP grown at low coverage on Au(788) is used as a reference.

Due to the lowered amount of 9-AGNRs, we observe more overlap of the PPP C-H/D modes with the C-H/D modes of the 9-AGNR, which causes the base of the peaks around this area between 1200 cm^{-1} and 1300 cm^{-1} to broaden. Consequently, the low coverage 9-AGNR + PPP sample shows slight deviation in peak shape around the regime of C-H and D modes compared to the 9-AGNR and the high coverage 9-AGNR + PPP (see Figure A.3 in Section A.4).
Nevertheless, a sharp D mode appears at 1335 cm^{-1} on low coverage 9-AGNR + PPP sample, which likewise shows a slight redshift compared to the D mode of sole 9-AGNRs at low coverage. In contrast, no change in the Raman shift of highest C-H peak around 1251 cm^{-1} is observed on the combined sample relative to sole 9-AGNRs.

The above observations indicate that the low coverage 9-AGNR + PPP exhibits the modes familiar from pure 9-AGNR with only minor changes due to the PPP. All modes with exception of the C-H mode of highest intensity show a slight redshift on the combined sample. On this basis, we suggest that the presence of PPP could potentially change the interactions between the GNRs and the substrate at low coverage, leading to the observed shifts.

3.3.5 Raman spectroscopy of 9-AGNR + PPP transferred to Raman-optimized (RO) substrate

Raman study of high and low coverage 9-AGNR + PPP before and after transfer

By now, we laid out first insights into the influence of PPP on the 9-AGNR with Raman spectroscopy. As discussed for sole 9-AGNR in Section 3.2.3, the unreliable transfer of low coverage 9-AGNR lead to the idea of passivating the step-edge with

PPP. In this respect, we have yet to examine if PPP indeed influences the substrate transfer, analyzing the low coverage 9-AGNR + PPP sample transferred onto the RO substrate. Before the discussion, it however has to be emphasized that these are only preliminary measurements. As we only transferred two low coverage 9-AGNR samples (one as shown below and one for the polarized Raman measurements in Section 3.3.5), these measurements just provide a first insight into the transfer of the low coverage 9-AGNR + PPP. To make more fundamental statements about the yield and reliability of the transfer compared to sole 9-AGNR, further measurements have to be made.

Figure 3.26 shows a comparison of the low coverage 9-AGNR + PPP sample on Au(788) (before transfer) to the RO substrate (after transfer). For reference, we show pure 9-AGNR at low coverage on the RO substrate.

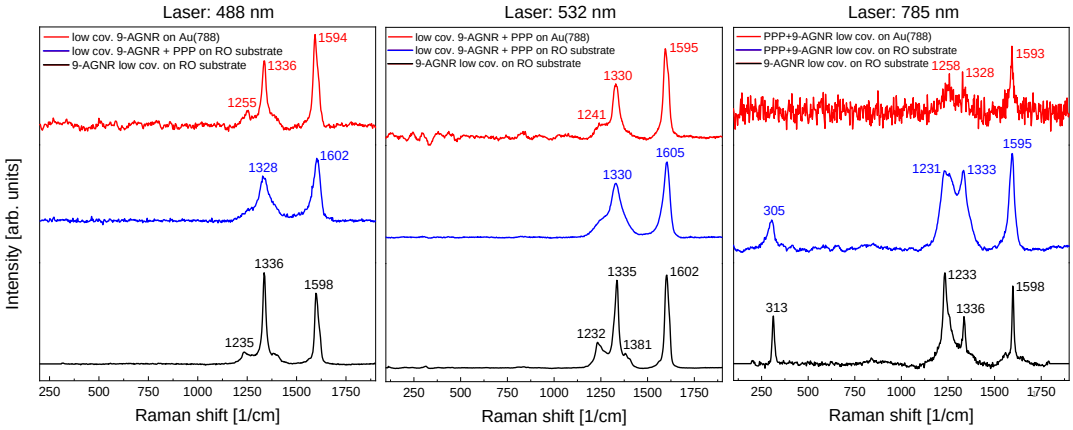

FIGURE 3.26: Raman spectra of low coverage 9-AGNR + PPP on Au(788) before transfer and after transfer on RO substrate measured with the 488 *nm*, 532 *nm* and 785 *nm* laser. 9-AGNRs grown at low coverage transferred to the RO substrate is used as a reference.

Table 3.6 displays the fitted FWHM of the G peak for all employed lasers before and after transfer. With exception of the 785 *nm* laser that did not provide a processable spectrum before the transfer [6], a broadening of the G peak and D modes is observed for all lasers. We previously claimed that broadening around these areas could be a well-accessible measure of non-uniform transfers. The defective structures exhibit significant alterations around the edges, causing broadening of C-H/D modes, and alterations in the periodicity of the sp^2-lattice, causing broadening of G modes, respectively.
Consequently, the transfer of the investigated low coverage 9-AGNR sample with only a single PPP per step-edge appears not to have been transferred reliably. Although direct comparison with poorly transferred sole 9-AGNRs (see Figure 3.17 and Section 3.3.5) indicates a slight improvement around the C-H and D modes, since there is a slight separation between the two modes on the low coverage 9-AGNR + PPP. As observed on the transfers of pure low coverage 9-AGNRs, a single

[6] Note however that the 785 *nm* spectrum after the transfer shows the peaks more clearly that could not be resolved due to the laser issue before the transfer. This is additional prove that there was indeed an issue with the 785 *nm* laser before the transfer instead of the sample.

transfer cannot provide a profound assessment of the transfer quality of low coverage 9-AGNR on a PPP-passivated Au(788) surface.

	Au(788)	**RO substrate**
488 nm	$(31.03 \pm 1.53)\ cm^{-1}$	$(44.43 \pm 2.46)\ cm^{-1}$
532 nm	$(33.66 \pm 1.13)\ cm^{-1}$	$(42.75 \pm 1.80)\ cm^{-1}$

TABLE 3.6: FWHM of the G peak obtained by a Lorentzian fit of the G peak on Au(788) before transfer and after transfer on RO substrate.

While the C-H/D and G modes show a blueshift due to the interactions of the 9-AGNRs and the PPP with the surface of the RO substrate compared to Au(788) for all lasers, we observe a distinct redshift of the RBLM located at 305 cm^{-1} emphasized on the 785 nm laser spectrum.
Note that we thus far never observed a shift with the RBLM before and after transfer. As the 785 nm laser has been shown to only be resonant with the 9-AGNRs, an signal contribution of PPP can be excluded. The presence of PPP could however lead to a change in interaction of the 9-AGNRs with the substrate after transfer, causing a shift. The observed RBLM is also broadened significantly. Consequently, this broadening could go in hand with defects, leading to an alteration of the width-related vibrations. The overlap of the entirety of these modes exhibiting a slight deviation in Raman shifts ultimately could result in the observed RBLM peak.

These preliminary investigations on the transfer of low coverage 9-AGNR + PPP show that there is interesting potential in improving the transfer by passivating the step-edge of Au(788) with PPP. Although the present data does not point towards a uniform transfer, we see a slight separation between the C-H and D modes, while the poorly transferred sole 9-AGNR at low coverage only showed one broad peak at this region. However, comparison to the well transferred 9-AGNR at low coverage indicates that the transfer of the low coverage 9-AGNR + PPP lead to a significant broadening of the G, C-H/D mode and even the RBLM. Therefore, further Raman studies of the transfer of low coverage 9-AGNRs grown on PPP passivated vicinal gold surfaces have to be conducted in order to fully understand the whole of PPP upon 9-AGNR transfer.

Raman study of low coverage 9-AGNR and 9-AGNR + PPP alignment after transfer

Although the broadening of the G peak is a first indication on the transfer uniformity, more information is needed to provide a complete understanding of the quality of the substrate transfer. In terms of device yield, besides staying intact after transfer, the 9-AGNRs have to preserve the high degree of alignment that was obtained by the growth on a vicinal gold surface (see Section 3.2.2).

The alignment of the 9-AGNR and 9-AGNR + PPP grown at low coverage [7] transferred onto the RO substrate was measured with polarized Raman spectroscopy. [8] The polarization was varied from -90 ° to 90 ° rotated relative to the direction of the terraces. The polar plot depicted in Figure **??** shows the G mode intensity extracted by a Lorentzian fit of the G peak for each angle. The G intensity follows $\cos^4(\theta)$, where θ denotes the angle between light polarization and the GNR alignment axis. [76, 125]

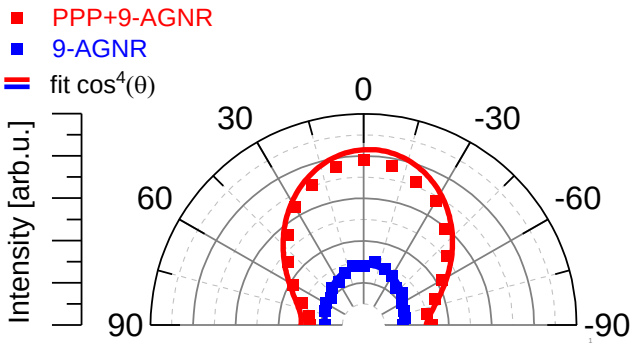

FIGURE 3.27: Polarization plots obtained by Raman polarized Raman spectroscopy on transferred low coverage 9-AGNR and low coverage 9-AGNR + PPP.

The Raman polarization anisotropy P [125] is used for a quantitative description of the alignment. It is defined as

$$P = \frac{I_{\parallel} - I_{\perp}}{I_{\parallel} + I_{\perp}} \ , \tag{3.1}$$

where $I_{\parallel}$ and $I_{\perp}$ denote the Raman spectra measured for the incident and scattered light polarized along and perpendicular to the step-edges of Au(788). P yields a value between 0 and 1, where an increase in alignment along the direction of the terraces is reflected in an increase in P. $P = 1$ thus means perfect alignment with the direction of the terraces, while $P = 0$ denotes no degree of alignment. [125]

We obtain $P = 0.25$ for low coverage 9-AGNR and $P = 0.47$ for low coverage 9-AGNR+PPP measured on the RO substrate after transfer. Even though the obtained Raman plots (see Figure A.4 in Section A.4) do not highlight significant differences with exception of the increased signal-to-noise ratio of the transferred low coverage 9-AGNR + PPP sample, we see a notable increase in P for the 9-AGNR + PPP compared to sole 9-AGNR on the RO substrate. The present data suggests that the alignment of the low coverage 9-AGNR + PPP sample is slightly improved in regard to sole 9-AGNR grown at this coverage. Moreover, note that even the best transfers of low coverage 9-AGNRs (as seen in Section 3.2.3) showed a Raman polarization

[7] The parameters for the deposition of the 9-AGNR precursor and the annealing steps to grow the GNRs were equal on both samples, granting equal coverage. As previously discussed, low coverage denotes 9-AGNRs grown at a one GNR per step coverage, while the low coverage 9-AGNR + PPP contains one ribbon each of PPP and 9-AGNR.

[8] Note that the Raman spectra (see Figure A.4 in Section A.4) showed significant broadening for both low coverage 9-AGNR and low coverage 9-AGNR + PPP, especially around the C-H/D modes. However, since the G peaks were narrow enough to be used for the analysis, we decided to make a preliminary comment on the observed alignment, although we have to keep in mind that both transfers do not point towards a high quality transfer on these samples.

anisotropy of $P = 0.58$. Therefore, no significant decrease of the Raman polarization anisotropy is observed on the low coverage 9-AGNR + PPP sample, even though the Raman spectra point towards a poorly transferred sample.
Even though we see a relative improvement on the PPP passivated sample, Raman polarization anisotropy of $P = 0.47$ is still far away from the desired value. A highly aligned sample, as it is observed for low coverage 9-AGNR grown on Au(788), yield a Raman polarization anisotropy up to $P = 0.95$. Consequently, the alignment of the low coverage 9-AGNR + PPP samples as presented here need to be further optimized.

To finalize this discussion, it is once again important to note that we can not reach definitive conclusions without a systematic study on identically prepared samples. According to the observations on the transfer of low coverage 9-AGNRs, the transfer does not always yield the same result due to the fact that the transfer process is dependent on the interplay of many different factors to work towards a successful transfer.
Nevertheless, the present data gives first insights into the effects of PPP passivation on the transfer of low coverage 9-AGNRs grown on Au(788). We showed that we obtain an increased value of the Raman polarization anisotropy P for low coverage 9-AGNRs grown on Au(788) passivated with PPP.

Chapter 4

Conclusion and Outlook

4.1 Conclusion

This thesis allowed us to gain insights into the properties of PPP and explore the effect of PPP as a step-edge passivator for the growth of 9-AGNR on vicinal surfaces. Growing low coverage PPP on Au(788), PPP shows a high affinity to grow along the step-edge, similar to 9-AGNRs. Similarities are further observed at increased PPP density on Au(788), as PPP shows increase in length and alignment. We observed lateral fusion of PPP at 400 $^{\circ}C$, supported by the RBLMs for wider GNRs observed with Raman spectroscopy. The Raman spectra point towards a more reliable formation of 6- and 9-AGNRs when PPP is annealed gradually to 400 $^{\circ}C$, compared to direct annealing to 400 $^{\circ}C$, suggesting that fusion is facilitated due to the prolonged exposure to higher annealing temperatures. The transfer spectra of PPP moreover indicate that PPP is transferred well to the RO substrate both at high and low coverage.
We proved that it is possible to grow 9-AGNRs on Au(788) edge-passivated with PPP by gradual deposition and annealing both STM imaging and Raman spectroscopy, which did not show a difference between the spectra of high coverage 9-AGNR + PPP and sole 9-AGNR. We also concluded that the PPP does not fuse with the 9-AGNRs at 400 $^{\circ}C$ (i.e. the peak annealing temperature for the preparation of the sample) . We established growth statistics to compare the growth of the GNRs on both PPP-passivated and unpassivated Au(788) surfaces, pointing towards a decrease in length and alignment of the GNRs growing along the step-edge when PPP is present at the step-edge. The 9-AGNR + PPP sample furthermore showed a higher ratio of GNRs growing on top of the terrace with an increased average length (12 nm) in respect to sole 9-AGNRs (6 nm), owed to the occupation of the step-edge by PPP. Raman spectroscopy of low coverage 9-AGNR + PPP after substrate transfer showed increased broadening, as generally also observed for pure low coverage 9-AGNR, pointing towards a non-uniform transfer for 9-AGNR grown together with the passivator PPP on Au(788). Preliminary measurements on the alignment of transferred low coverage 9-AGNR + PPP compared to low coverage 9-AGNR suggest an increase in alignment, reflected by the Raman polarization anisotropy increase from $P = 0.25$ (for sole 9-AGNR) to $P = 0.47$ (for 9-AGNR + PPP).
Even though this increase is promising in terms of further investigations of the edge-passivation of vicinal surfaces with PPP, the yet insufficient value of P combined with the observed broadening after transfer at low coverage indicate that the discussed protocol of growth of PPP together with 9-AGNRs needs further optimization.

4.2 Outlook

In a further step, statistical evaluations of the transfer would be necessary to make a better judgement of the influence of PPP on the transfer quality of 9-AGNRs at low coverage. The Raman studies on the 9-AGNR + PPP samples conducted so far represent preliminary measurements that are required to be repeated with identically prepared samples to make a more complete assessment of the yield.
The presented preliminary transfer data however suggests that the PPP-passivation has to be optimized moving forward. A good starting point would be to explore an increased coverage of PPP towards the growth of two wires of PPP growing side-by-side along the step-edge. Since the growth statistics indicate that a large amount of GNRs grows along the step-edge even though it is already occupied by PPP, the growth of two wires might help the GNRs to grow closer towards the center of the terrace, which could in return influence the transfer efficiency.
Another gateway could be to sandwich the deposited 9-AGNRs between PPP by a subsequent deposition of PPP at high coverage on the 9-AGNR + PPP sample. This might allow to transfer 9-AGNR together with PPP in a film-like behaviour, further increasing the yield of the transfer. Preliminary STM investigations of GNRs sandwiched between PPP have showed that GNRs can be sandwiched between PPP wires with no significant amount of fusion (see Figure 4.1). Raman spectroscopy measurements need to be done to confirm these results.

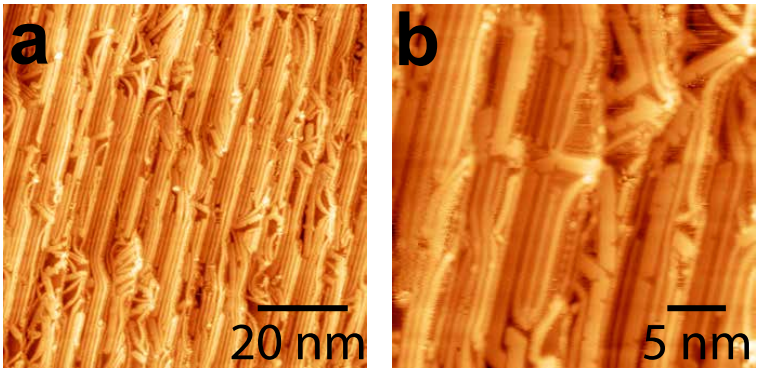

FIGURE 4.1: STM images of a prepared [1] trial sample PPP + 9-AGNR + PPP sample. Note that the coverage of 9-AGNR is slightly below one ribbon per step. **a**: Overview image of the PPP + 9-AGNR + PPP sample. Bias voltage: -1.5 V. Current: 30 pA. **b**: Close-up image of the PPP + 9-AGNR + PPP sample. We see both 9-AGNRs and PPP, suggesting that it is potentially possible to sandwich 9-AGNRs with PPP without fusion. Bias voltage: -1.6 V. Current: 30 pA.

Concerning the passivator, other GNRs or nanowires with a similar growth behaviour could be explored. For example, chevron GNRs have shown to grow close to the step-edge in a similar fashion, representing a promising material to test the transfer efficiency of 9-AGNRs grown together with chevron GNRs on vicinal surfaces.

[1] The sample was prepared by deposition of the PPP precursor at 102 °C for 2 *min* 35 *sec* and subsequent annealing at 250 °C to grow low coverage (one wire per step) PPP. Afterwards, the 9-AGNR precursor was deposited at 67 °C for 2 *min* 30 *sec*, followed by annealing at 200 °C and 400 °C. Finally, a second dose of PPP precursor was deposited at 102 °C for 10 *min* with subsequent annealing at 200 °C to grow high coverage PPP. 10 *min* annealing time for each step.

Appendix A

Appendix

A.1 Introduction

..

A.1.1 Origin of Stokes- and Anti-Stokes scattering

To understand the origin of Raman scattering more in detail, one has to refer to the dipole moment of a molecule in an electric field $\overrightarrow{E}$. Irradiating the molecule with a laser (i.e. electromagnetic radiation) leads to an oscillating disturbance in the electric field over time. Therefore, the dipole moment is given by

$$\mu(t) = \overrightarrow{\alpha} \cdot \overrightarrow{E}(t) = \overrightarrow{\alpha} \cdot \overrightarrow{E_0} \cdot cos(\omega_0 t) \ , \tag{A.1}$$

where $\overrightarrow{\alpha}$ is the polarizability of the molecule. As previously stated, Raman scattering occurs due to a change in polarization of the molecule. This however only occurs if the molecule is disturbed out of its equilibrium position Q_0. The emitted phonon of a normal-mode vibration along a coordinate q as a result of the displacement around Q_0 follows

$$q = q_0 \cdot cos(\omega_p t) \ . \tag{A.2}$$

By Taylor expansion [1] of the polarizability around Q_0 and combining the equation with A.2 and A.1, one obtains a modified expression of $\mu(t)$ involving both angular frequencies of the phononic osciallation and the photonic osciallation.

$$\begin{aligned}\mu(t) = \ & \overrightarrow{\alpha_0} \cdot \overrightarrow{E_0} \cdot cos(\omega_0 t) \\ & + \frac{1}{2}(\frac{\partial \overrightarrow{\alpha}}{\partial q})_{q_0} \cdot q_0 \cdot \overrightarrow{E_0} \cdot cos[(\omega_0 - \omega_q)t] \\ & + \frac{1}{2}(\frac{\partial \overrightarrow{\alpha}}{\partial q})_{q_0} \cdot q_0 \cdot \overrightarrow{E_0} \cdot cos[(\omega_0 + \omega_q)t]\end{aligned}$$

The time-dependence of the dipole moment of the molecule is the source of Raman scattering. It is composed of a sum of three terms, all involving different oscillation frequencies. Hereby, the oscillation frequency ω_0 corresponds to Rayleigh scattering (no exchange of energy), $(\omega_0 - \omega_q)$ corresponds to Stokes scattering (molecule absorbs energy [2]) and $(\omega_0 + \omega_q)$ corresponds to anti-Stokes scattering (molecule loses energy [2]). [103]

[1] Second order or higher terms are dropped from this equation

[2] The difference in energy always corresponds to exactly one phonon.

A.2 Materials and Methods

A.2.1 Ultra-high vacuum (UHV) Technology

Theoretical aspects

Why Ultra-High Vacuum? Characterization of surfaces portrays a significant challenge due to the requirement that the surface composition remains vastly unaltered over the duration of the experiment. This eliminates the possibility to conduct experiments at atmospheric pressures, since atoms and molecules from the atmosphere are adsorbed on the surface at high rates. The rate of impingement of particles on a surface is described over the flux I as

$$I = \frac{p}{\sqrt{2\pi m k_B T}} \tag{A.3}$$

where p is the pressure, m is the mass of the particle, k_B is Boltzmann's constant and T is the temperature. Consequently, under the assumption of a sticking coefficient of 1 [3] the rate of adsorption of a molecule on a crystal surfaces is directly proportional to the pressure. It is therefore essential to conduct these experiments under conditions with a minimal external pressure. In fact, the number of atoms or molecules adsorbed on the surface should not exceed a few percent of a monolayer per hour, which equals to a pressure in the order of 10^{-9} *mbar* at least. Systems which satisfy this criterion are called Ultra-High Vacuum (UHV) systems. Additionally, note that Equation A.3 indicates a decrease in the rate of adsorption towards higher temperatures. This is supplemental parameter altered by the experimental setup. [126]

How is Ultra-High Vacuum achieved? Contrary to the implication of the term "vacuum", it is impossible to achieve perfect vacuum experimentally or even theoretically. However, with UHV it is possible to reach the pressures where the number of molecules in the chamber a merely insignificant in terms of contamination of the investigated surfaces in the time frame of the experiment. [4] A simple UHV system consists of a vacuum chamber connected to a pump. Pumping of the system results in a gas flow from the chamber to the pump, due to the pressure difference between the two. When a system is pumped, it will eventually reach a steady state. The resulting *base pressure* p_B obeys the relation

$$p_B = \frac{Q_T}{S} \tag{A.4}$$

with S the pumping speed and Q_T the total gas load. Hence, to get an optimal base pressure the total gas load should be minimized, while the pumping speed should be maximized.
Leaks in the system, either due to gases diffusing from the atmosphere outside into the system or due to the slow liberation of gases that are trapped inside the system, cause a the total gas load to increase. An additional factor is the desorption of gases from surfaces inside the system. This process is called *degassing*. Higher temperatures cause an increase in desorption. This is called *bakeout* of the system, which is the process of heating of the system after venting in order to enhance the pumping of internal gas molecules and decrease the base pressure to a minimum.

[3] Although not valid for all surfaces, all surfaces investigated here come close to that assumption.

[4] If the experiment spans over multiple days an observable amount of contamination may occur, even though the atoms or molecules only are present in spare amounts.

The pumping speed can be improved by employing an appropriate pumping system consisting of *rotary pumps*, *ion pumps*, and *titanium sublimation pumps*. A UHV system always consists of multiple pumps that work in different pressure ranges because a single pump would not come close to reaching the desired pressures. Details about the employed pumps and other materials in the UHV system will be addressed in A.2.1. [126]

Instrumentation

Reaching UHV requires special instrumentation, incorporating materials with minimal gas leak with valves, gauges and pumps. In the following, a more detailed look at the experimental setup of a UHV system is provided.

UHV Materials The most common material used in the majority of UHV systems is stainless steel. It fulfills certain criteria such as low gas permeability, resistance to corrosion and the desire to be non-magnetic, making it an ideal candidate. Other materials are used inside the chambers, among them copper and aluminium. Fortunately, glass also has beneficial properties and can be used to incorporate windows on the walls of the chamber. [126] This is essential because it allows to see inside the chamber when manipulating the sample. A further advantage of these materials is their tolerance towards higher temperatures required when performing a bakeout of the system.

Pumping to UHV The main components of a pumping system are pumps, gauges and valves.
To reach and maintain UHV, a series of pumps working in different pressure ranges is needed. To reach a pressure in the order of 10^{-3} *mbar*, pre-vacuum pumps such as *rotary valve pumps* are used, responsible for maintaining sufficient backing vacuum for the high-vacuum as well as the exhaustion of gases into the atmosphere. A rotary valve pump consists of an eccentrically mounted rotor inside a cylindrical housing. Movable blades are mounted on the rotor, which expand upon rotation of the rotor due to centrifugal forces. As gas flows from the inlet port into the compressor chamber, the rotation causes the air to get trapped between the two blades. The air further expands to a maximum volume, preventing undesired condensation. Further rotation causes compression of the air and the pressure is high enough so that it can be expelled to the atmosphere by the unidirectional outlet valve. [127, 128] The pre-vacuum pump is placed in front of the turbomolecular pump of the PC and FEL. Below 10^{-3} *mbar turbomolecular* and *ion pumps* operate in order to pump the system down to the range of 10^{-11} *mbar*. An ion pump incorporates short stainless steel tubes (representing the anode) sandwiched between two titanium plates (representing the cathode). A strong magnetic field is applied parallel to the contact. As electrons are emitted an accelerated towards the anode, ionization gas molecules occur. In the applied electric field, the ionized gas molecule subsequently is accelerated towards the cathode, causing a release of titanium particles. The sputtered titanium coats the surface of the tubes and pump walls and can react chemically with the surrounding gas molecules and thus remove them from the atmosphere. [129] A feature of ion pumps is the ability to read out the pressure inside the chamber over the value of the pump current. Ion pumps are employed in both the PC and the AC.
Turbomolecular pumps convoy the ion pumps to improve the pumping efficiency in the low pressure range up to UHV. The structure and function of a turbomolecular pump resembles a jet-engine. It consists of a rotating central shaft with slotted disks.

They are intertwined with static discs, mounted to the walls of the pump. As gas flows into the pumping chamber, the rotation of the central shaft causes the gas to flow towards the outer walls of the pump. The gas then is directed towards the prevacuum pump and exits the system. [130] Because of the high noise and vibration the pump is placed outside of the analysis chamber at the end of the PC. A second turbomolecular pump is used to pump the FEL.
The removal of active gases like H_2 or O_2 is achieved with *titanium sublimation pumps*. Through heating of a Ti-covered filament through application of a current, titanium is sublimated. The resulting Ti-film reacts with the active gases, making them non-volatile, similar to the working principle of ion pumps.
An accurate reading of the pressure is provided by *ionization gauges*, operating at pressures below 10^{-3} mbar. Due to termionic emission of electrons from a hot filament, atoms and molecules from the system gas are ionized. They are subsequently attracted towards a collector, converting the resulting current to a pressure indication. [126]
Valves are used to isolate one chamber from the rest of the system. This is primarily necessary for introducing a sample into the system and is however also advantageous as a safety precaution. Usually, copper is used as a sealing material.

A.3 Supplemental STM data

A.3.1 Annealing of Poly(para-phenylene) (PPP)

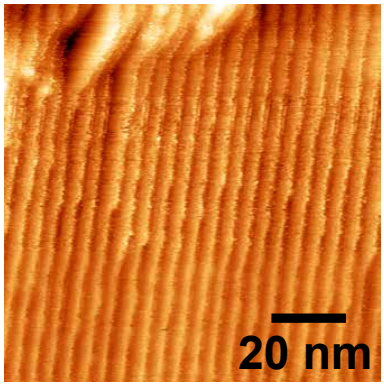

FIGURE A.1: STM image of high coverage PPP precursor on Au(788) annealed at 200 $^{\circ}C$. The tip is dragging molecules on the surface, which indicates that no PPP is formed at this temperature. Bias voltage: 2 V. Current: 30 pA.

A.4 Supplemental Raman data

A.4.1 Raman spectroscopy of Poly(para-phenylene) (PPP)

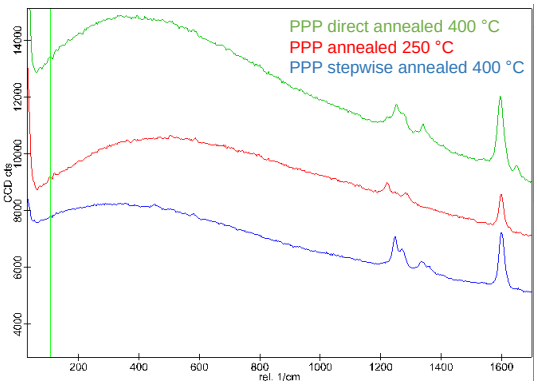

FIGURE A.2: LCM appearing at 107 cm^{-1} for PPP annealed at 250 °C and PPP annealed at 400 °C. No background subtraction was performed on the plots shown here.

A.4.2 Raman spectroscopy of 9-armchair graphene nanoribbons (9-AGNRs) + Poly(para-phenylene) (PPP)

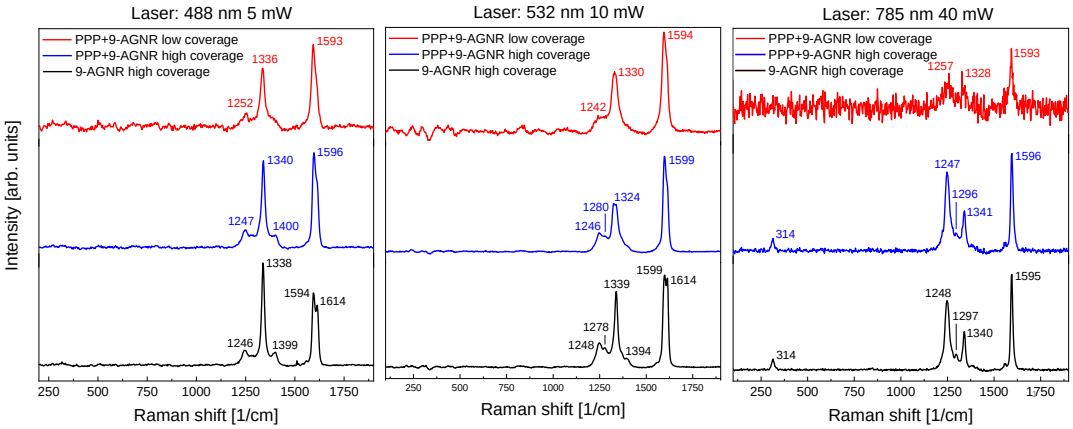

FIGURE A.3: Comparison of the high and low coverage 9-AGNR + PPP and pure 9-AGNR with Raman spectroscopy. The side-by-side view reveals that high coverage 9-AGNR + PPP more closely resembles the pure 9-AGNR at high coverage, as expected by the difference in relative amount.

A.4.3 Raman spectra of low coverage 9-AGNR and 9-AGNR + PPP used for polarized Raman spectroscopy

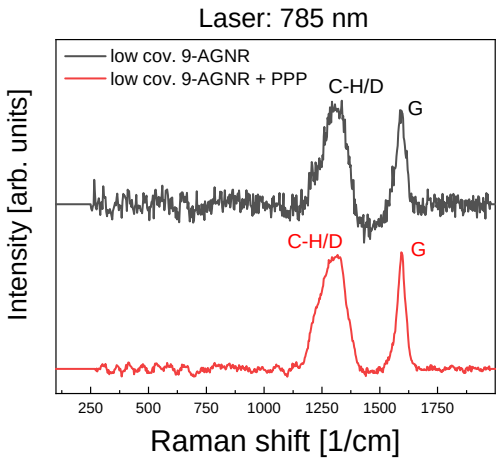

FIGURE A.4: 785 *nm* laser Raman spectra of low coverage 9-AGNR and low coverage 9-AGNR + PPP with $\theta = 0$ (aligned with terraces). We see significant broadening of the C-H/D modes.

Bibliography

[1] Andre K Geim and Konstantin S Novoselov. "The rise of graphene". In: *Nanoscience and technology: a collection of reviews from nature journals*. World Scientific, 2010, pp. 11–19.

[2] Kostya S Novoselov et al. "Electric field effect in atomically thin carbon films". In: *science* 306.5696 (2004), pp. 666–669.

[3] Tsuneya Ando, Alan B Fowler, and Frank Stern. "Electronic properties of two-dimensional systems". In: *Reviews of Modern Physics* 54.2 (1982), p. 437.

[4] Rahul Raveendran Nair et al. "Fine structure constant defines visual transparency of graphene". In: *Science* 320.5881 (2008), pp. 1308–1308.

[5] Madhusree Kole and TK Dey. "Investigation of thermal conductivity, viscosity, and electrical conductivity of graphene based nanofluids". In: *Journal of Applied Physics* 113.8 (2013), p. 084307.

[6] Dimitar Dimov et al. "Ultrahigh performance nanoengineered graphene–concrete composites for multifunctional applications". In: *Advanced functional materials* 28.23 (2018), p. 1705183.

[7] SC Devi and RA Khan. "Effect of graphene oxide on mechanical and durability performance of concrete". In: *Journal of Building Engineering* 27 (2020), p. 101007.

[8] Wenbo Zeng et al. "The utilization of graphene oxide in traditional construction materials: Asphalt". In: *Materials* 10.1 (2017), p. 48.

[9] Kostya S Novoselov et al. "Two-dimensional atomic crystals". In: *Proceedings of the National Academy of Sciences* 102.30 (2005), pp. 10451–10453.

[10] Jian Ru Gong. *Graphene: Synthesis, Characterization, Properties and Applications*. BoD–Books on Demand, 2011, pp. 172–172.

[11] Kazuyuki Takai et al. *Graphene: Preparations, Properties, Applications, and Prospects*. Elsevier, 2019, pp. 176–178.

[12] Philip Richard Wallace. "The band theory of graphite". In: *Physical review* 71.9 (1947), p. 622.

[13] Viktor Ariel and Amir Natan. "Electron effective mass in graphene". In: *2013 International Conference on Electromagnetics in Advanced Applications (ICEAA)*. IEEE. 2013, pp. 696–698.

[14] Alfonso Reina et al. "Large area, few-layer graphene films on arbitrary substrates by chemical vapor deposition". In: *Nano letters* 9.1 (2009), pp. 30–35.

[15] Francesco Bonaccorso et al. "Graphene photonics and optoelectronics". In: *Nature photonics* 4.9 (2010), pp. 611–622.

[16] Krishna Shenai. "Future prospects of widebandgap (WBG) semiconductor power switching devices". In: *IEEE Transactions on Electron Devices* 62.2 (2014), pp. 248–257.

[17] Sudipta Dutta and Swapan K Pati. "Novel properties of graphene nanoribbons: a review". In: *Journal of Materials Chemistry* 20.38 (2010), pp. 8207–8223.

[18] Pascal Ruffieux et al. "Electronic structure of atomically precise graphene nanoribbons". In: *Acs Nano* 6.8 (2012), pp. 6930–6935.

[19] Simon M Sze, Yiming Li, and Kwok K Ng. *Physics of semiconductor devices*. John wiley & sons, 2021.

[20] Anurag Srivastava et al. "Width dependent electronic properties of graphene nanoribbons: an ab-initio study". In: *Journal of Computational and Theoretical Nanoscience* 9.7 (2012), pp. 1008–1013.

[21] Steffen Linden et al. "Electronic structure of spatially aligned graphene nanoribbons on Au (788)". In: *Physical review letters* 108.21 (2012), p. 216801.

[22] Li Yang et al. "Quasiparticle energies and band gaps in graphene nanoribbons". In: *Physical Review Letters* 99.18 (2007), p. 186801.

[23] Young-Woo Son, Marvin L Cohen, and Steven G Louie. "Energy gaps in graphene nanoribbons". In: *Physical review letters* 97.21 (2006), p. 216803.

[24] Philip Shemella et al. "Energy gaps in zero-dimensional graphene nanoribbons". In: *Applied Physics Letters* 91.4 (2007), p. 042101.

[25] Young-Woo Son, Marvin L Cohen, and Steven G Louie. "Erratum: energy gaps in graphene nanoribbons [Phys. Rev. Lett. 97, 216803 (2006)]". In: *Physical Review Letters* 98.8 (2007), p. 089901.

[26] Zongping Chen, Akimitsu Narita, and Klaus Müllen. "Graphene Nanoribbons: On-Surface Synthesis and Integration into Electronic Devices". In: *Advanced Materials* 32.45 (2020), p. 2001893.

[27] T Ihn et al. "Graphene single-electron transistors". In: *Materials today* 13.3 (2010), pp. 44–50.

[28] Vivek Saraswat, Robert M Jacobberger, and Michael S Arnold. "Materials Science Challenges to Graphene Nanoribbon Electronics". In: *ACS nano* 15.3 (2021), pp. 3674–3708.

[29] Max C Lemme et al. "Etching of graphene devices with a helium ion beam". In: *ACS nano* 3.9 (2009), pp. 2674–2676.

[30] Vera Abramova, Alexander S Slesarev, and James M Tour. "Meniscus-mask lithography for narrow graphene nanoribbons". In: *ACS nano* 7.8 (2013), pp. 6894–6898.

[31] Jeong Gon Son et al. "Sub-10 nm Graphene Nanoribbon Array Field-Effect Transistors Fabricated by Block Copolymer Lithography". In: *Advanced Materials* 25.34 (2013), pp. 4723–4728.

[32] Guibai Xie et al. "Graphene edge lithography". In: *Nano letters* 12.9 (2012), pp. 4642–4646.

[33] Levente Tapasztó et al. "Tailoring the atomic structure of graphene nanoribbons by scanning tunnelling microscope lithography". In: *Nature nanotechnology* 3.7 (2008), pp. 397–401.

[34] Hiroki Ago et al. "Synthesis of high-density arrays of graphene nanoribbons by anisotropic metal-assisted etching". In: *Carbon* 78 (2014), pp. 339–346.

[35] Xinran Wang et al. "Room-temperature all-semiconducting sub-10-nm graphene nanoribbon field-effect transistors". In: *Physical review letters* 100.20 (2008), p. 206803.

[36] Dmitry V Kosynkin et al. "Longitudinal unzipping of carbon nanotubes to form graphene nanoribbons". In: *Nature* 458.7240 (2009), pp. 872–876.

[37] Yuuta Yano et al. "Living annulative pi-extension polymerization for graphene nanoribbon synthesis (Jun, 10.1038/s41586-019-1331-z, 2020)". In: *Nature* 586.7828 (2020), E13–E13.

[38] Timothy H Vo et al. "Large-scale solution synthesis of narrow graphene nanoribbons". In: *Nature communications* 5.1 (2014), pp. 1–8.

[39] Mikhail Shekhirev et al. "Aggregation of atomically precise graphene nanoribbons". In: *Rsc Advances* 7.86 (2017), pp. 54491–54499.

[40] Mikhail Shekhirev et al. "Interfacial self-assembly of atomically precise graphene nanoribbons into uniform thin films for electronics applications". In: *ACS applied materials & interfaces* 9.1 (2017), pp. 693–700.

[41] Jinming Cai et al. "Atomically precise bottom-up fabrication of graphene nanoribbons". In: *Nature* 466.7305 (2010), pp. 470–473.

[42] Leopold Talirz, Pascal Ruffieux, and Roman Fasel. "On-surface synthesis of atomically precise graphene nanoribbons". In: *Advanced materials* 28.29 (2016), pp. 6222–6231.

[43] Leopold Talirz et al. "On-surface synthesis and characterization of 9-atom wide armchair graphene nanoribbons". In: *ACS nano* 11.2 (2017), pp. 1380–1388.

[44] Martina Corso et al. "Chapter Bottom-Up Fabrication of Atomically Precise Graphene Nanoribbons". In: *On-Surface Synthesis II*. Springer Nature, 2018.

[45] Christopher Bronner et al. "Aligning the band gap of graphene nanoribbons by monomer doping". In: *Angewandte Chemie* 125.16 (2013), pp. 4518–4521.

[46] Ryan R Cloke et al. "Site-specific substitutional boron doping of semiconducting armchair graphene nanoribbons". In: *Journal of the American Chemical Society* 137.28 (2015), pp. 8872–8875.

[47] Jonas Bjork, Felix Hanke, and Sven Stafstrom. "Mechanisms of halogen-based covalent self-assembly on metal surfaces". In: *Journal of the American Chemical Society* 135.15 (2013), pp. 5768–5775.

[48] Marco Di Giovannantonio et al. "On-surface growth dynamics of graphene nanoribbons: the role of halogen functionalization". In: *ACS nano* 12.1 (2018), pp. 74–81.

[49] Arunabh Batra et al. "Probing the mechanism for graphene nanoribbon formation on gold surfaces through X-ray spectroscopy". In: *Chemical Science* 5.11 (2014), pp. 4419–4423.

[50] Rico Gutzler et al. "Ullmann-type coupling of brominated tetrathienoanthracene on copper and silver". In: *Nanoscale* 6.5 (2014), pp. 2660–2668.

[51] Manh-Thuong Nguyen, Carlo A Pignedoli, and Daniele Passerone. "An ab initio insight into the Cu (111)-mediated Ullmann reaction". In: *Physical Chemistry Chemical Physics* 13.1 (2011), pp. 154–160.

[52] Konstantin A Simonov et al. "From graphene nanoribbons on Cu (111) to nanographene on Cu (110): critical role of substrate structure in the bottom-up fabrication strategy". In: *ACS nano* 9.9 (2015), pp. 8997–9011.

[53] Jinming Cai et al. "Graphene nanoribbon heterojunctions". In: *Nature nanotechnology* 9.11 (2014), pp. 896–900.

[54] Leopold Talirz et al. "Termini of bottom-up fabricated graphene nanoribbons". In: *Journal of the American Chemical Society* 135.6 (2013), pp. 2060–2063.

[55] Stephan Blankenburg et al. "Intraribbon heterojunction formation in ultranarrow graphene nanoribbons". In: *Acs Nano* 6.3 (2012), pp. 2020–2025.

[56] Konstantin A Simonov et al. "Effect of substrate chemistry on the bottom-up fabrication of graphene nanoribbons: combined core-level spectroscopy and STM study". In: *The Journal of Physical Chemistry C* 118.23 (2014), pp. 12532–12540.

[57] Lawrence A Bottomley, Joseph E Coury, and Phillip N First. "Scanning probe microscopy". In: *Analytical Chemistry* 68.12 (1996), pp. 185–230.

[58] Gerd Binnig and Heinrich Rohrer. "Scanning tunneling microscopy". In: *Surface science* 126.1-3 (1983), pp. 236–244.

[59] Ernst Meyer, Hans Josef Hug, Roland Bennewitz, et al. *Scanning probe microscopy*. Vol. 4. Springer, 2003.

[60] Harold JW Zandvliet and Arie van Houselt. "Scanning tunneling spectroscopy". In: *Annual review of analytical chemistry* 2 (2009), pp. 37–55.

[61] PRGDJ Graves and D Gardiner. "Practical raman spectroscopy". In: *Springer* (1989).

[62] Chandrasekhara Venkata Raman and Kariamanikkam Srinivasa Krishnan. "A new type of secondary radiation". In: *Nature* 121.3048 (1928), pp. 501–502.

[63] Rajinder Singh and Falk Riess. "Sir CV Raman and the story of the Nobel prize". In: *Current Science* 75.9 (1998), pp. 965–971.

[64] Ewen Smith and Geoffrey Dent. *Modern Raman spectroscopy: a practical approach*. John Wiley & Sons, 2019.

[65] Manfred Hesse, Herbert Meier, and Bernd Zeeh. *Spektroskopische Methoden in der organischen Chemie*. Georg Thieme Verlag, 2005, pp. 69–71.

[66] Mettler-Toledo International Inc. *Raman-Spektrometer*. 2021. URL: https://www.mt.com/ch/de/home/products/L1-AutochemProducts/raman-spectrometer.html.

[67] Manfred Hesse, Herbert Meier, and Bernd Zeeh. *Spektroskopische Methoden in der organischen Chemie*. Georg Thieme Verlag, 2005, pp. 34–35.

[68] Jiali Wan et al. "Surface chemistry but not aspect ratio mediates the biological toxicity of gold nanorods in vitro and in vivo". In: *Scientific reports* 5.1 (2015), pp. 1–16.

[69] Xiaoting Jia et al. "Graphene edges: a review of their fabrication and characterization". In: *Nanoscale* 3.1 (2011), pp. 86–95.

[70] Heinz-Helmut Perkampus. *UV-VIS Spectroscopy and its Applications*. Springer Science & Business Media, 2013.

[71] Joost Van Der Lit et al. "Suppression of electron–vibron coupling in graphene nanoribbons contacted via a single atom". In: *Nature communications* 4.1 (2013), pp. 1–6.

[72] Saw-Wai Hla and Karl-Heinz Rieder. "STM control of chemical reactions: Single-molecule synthesis". In: *Annual review of physical chemistry* 54.1 (2003), pp. 307–330.

[73] Randall M Feenstra. "Scanning tunneling spectroscopy". In: *Surface science* 299 (1994), pp. 965–979.

[74] Baiqing Lv, Tian Qian, and Hong Ding. "Angle-resolved photoemission spectroscopy and its application to topological materials". In: *Nature Reviews Physics* 1.10 (2019), pp. 609–626.

[75] Jerry Tersoff and Donald R Hamann. "Theory of the scanning tunneling microscope". In: *Physical Review B* 31.2 (1985), p. 805.

[76] Jan Overbeck et al. "A universal length-dependent vibrational mode in graphene nanoribbons". In: *ACS nano* 13.11 (2019), pp. 13083–13091.

[77] Ali Maghsoumi et al. "Overtone and combination features of G and D peaks in resonance Raman spectroscopy of the C78H26 polycyclic aromatic hydrocarbon". In: *Journal of Raman Spectroscopy* 46.9 (2015), pp. 757–764.

[78] Roland Gillen et al. "Vibrational properties of graphene nanoribbons by first-principles calculations". In: *Physical Review B* 80.15 (2009), p. 155418.

[79] Roland Gillen, Marcel Mohr, and Janina Maultzsch. "Symmetry properties of vibrational modes in graphene nanoribbons". In: *Physical Review B* 81.20 (2010), p. 205426.

[80] Gabriela Borin Barin et al. "Surface-synthesized graphene nanoribbons for room temperature switching devices: substrate transfer and ex situ characterization". In: *ACS applied nano materials* 2.4 (2019), pp. 2184–2192.

[81] M Tommasini, Chiara Castiglioni, and Giuseppe Zerbi. "Raman scattering of molecular graphenes". In: *Physical Chemistry Chemical Physics* 11.43 (2009), pp. 10185–10194.

[82] R Saito et al. "Raman spectra of graphene ribbons". In: *Journal of Physics: Condensed Matter* 22.33 (2010), p. 334203.

[83] Chunxiao Cong, Ting Yu, and Haomin Wang. "Raman study on the G mode of graphene for determination of edge orientation". In: *ACS nano* 4.6 (2010), pp. 3175–3180.

[84] Matthieu Vandescuren et al. "Theoretical study of the vibrational edge modes in graphene nanoribbons". In: *Physical Review B* 78.19 (2008), p. 195401.

[85] Jian Zhou and Jinming Dong. "Vibrational property and Raman spectrum of carbon nanoribbon". In: *Applied Physics Letters* 91.17 (2007), p. 173108.

[86] Chuanxu Ma et al. "Seamless staircase electrical contact to semiconducting graphene nanoribbons". In: *Nano letters* 17.10 (2017), pp. 6241–6247.

[87] Patrick B Bennett et al. "Bottom-up graphene nanoribbon field-effect transistors". In: *Applied Physics Letters* 103.25 (2013), p. 253114.

[88] Jan Overbeck et al. "Optimized substrates and measurement approaches for Raman spectroscopy of graphene nanoribbons". In: *physica status solidi (b)* 256.12 (2019), p. 1900343.

[89] Juan Pablo Llinas et al. "Short-channel field-effect transistors with 9-atom and 13-atom wide graphene nanoribbons". In: *Nature communications* 8.1 (2017), pp. 1–6.

[90] Manabu Ohtomo et al. "Graphene nanoribbon field-effect transistors fabricated by etchant-free transfer from Au (788)". In: *Applied Physics Letters* 112.2 (2018), p. 021602.

[91] Roland Wiesendanger and Hans-Joachim Güntherodt. *Scanning tunneling microscopy I: General Principles and Applications to Clean and Adsorbate-Covered Surfaces*. Vol. 20. Springer Science & Business Media, 1992.

[92] M Okano et al. "Vibration isolation for scanning tunneling microscopy". In: *Journal of Vacuum Science & Technology A: Vacuum, Surfaces, and Films* 5.6 (1987), pp. 3313–3320.

[93] *Acitve vibration control: Principles of operation*. 2016. URL: http://www.herzan.com/resources/technology/active-vibration-control.html.

[94] David P DeWitt and Gene D Nutter. *Theory and practice of radiation thermometry*. John Wiley & Sons, 1988.

[95] Hwaiyu Geng and PE CMfgE. *Semiconductor manufacturing handbook*. McGraw-Hill Education, 2018. Chap. 21, p. 21.

[96] Douglas A Skoog, F James Holler, and Stanley R Crouch. *Principles of instrumental analysis*. Cengage learning, 2017, p. 9.

[97] William H King. "Piezoelectric sorption detector." In: *Analytical Chemistry* 36.9 (1964), pp. 1735–1739.

[98] H. W. Kim et al. "One-dimensional molecular zippers." In: *Journal of the American Chemical Society* 133 24 (2011), pp. 9236–8.

[99] Andrew Zangwill. *Physics at surfaces*. Cambridge university press, 1988.

[100] Teng Ma, Svetlozar Surnev, and Falko P Netzer. "Growth of ceria nano-islands on a stepped Au (788) surface". In: *Materials* 8.8 (2015), pp. 5205–5215.

[101] Frederick John Humphreys and Max Hatherly. *Recrystallization and related annealing phenomena*. Elsevier, 2012.

[102] Junmo Kang et al. "Graphene transfer: key for applications". In: *Nanoscale* 4.18 (2012), pp. 5527–5537.

[103] Jan Wolfgang Overbeck. "Nanojunctions from molecules to graphene nanoribbons: optical characterization and transport properties". PhD thesis. University of Basel, 2019.

[104] Douglas L Gin and Vincent P Conticello. "Poly (p-phenylene): new directions in synthesis and application". In: *Trends in Polymer Science* 7.4 (1996), pp. 217–223.

[105] Néstor Merino-Díez et al. "Width-dependent band gap in armchair graphene nanoribbons reveals Fermi level pinning on Au (111)". In: *ACS nano* 11.11 (2017), pp. 11661–11668.

[106] Andrea Basagni et al. "Molecules–oligomers–nanowires–graphene nanoribbons: a bottom-up stepwise on-surface covalent synthesis preserving long-range order". In: *Journal of the American Chemical Society* 137.5 (2015), pp. 1802–1808.

[107] Francesco De Boni et al. "Templating Effect of Different Low-Miller-Index Gold Surfaces on the Bottom-Up Growth of Graphene Nanoribbons". In: *ACS Applied Nano Materials* 3.11 (2020), pp. 11497–11509.

[108] Andrea Basagni et al. "Tunable band alignment with unperturbed carrier mobility of on-surface synthesized organic semiconducting wires". In: *Acs Nano* 10.2 (2016), pp. 2644–2651.

[109] Elsa Thune et al. "Understanding of one dimensional ordering mechanisms at the (001) sapphire vicinal surface". In: *Journal of Applied Physics* 121.1 (2017), p. 015301.

[110] S Paulin et al. "Unstable step meandering with elastic interactions". In: *Physical review letters* 86.24 (2001), p. 5538.

[111] Katsumichi Yagi, Hiroki Minoda, and Masashi Degawa. "Step bunching, step wandering and faceting: self-organization at Si surfaces". In: *Surface science reports* 43.2-4 (2001), pp. 45–126.

[112] Alberto Pimpinelli et al. "Equilibrium step dynamics on vicinal surfaces". In: *Surface Science* 295.1-2 (1993), pp. 143–153.

[113] Sunmin Ryu et al. "Raman spectroscopy of lithographically patterned graphene nanoribbons". In: *ACS nano* 5.5 (2011), pp. 4123–4130.

[114] Liming Xie et al. "Graphene nanoribbons from unzipped carbon nanotubes: atomic structures, Raman spectroscopy, and electrical properties". In: *Journal of the American Chemical Society* 133.27 (2011), pp. 10394–10397.

[115] Andre Leitao Botelho et al. "Structure and optical bandgap relationship of π-conjugated systems". In: *PloS one* 9.1 (2014), e86370.

[116] Sihan Zhao et al. "Optical imaging and spectroscopy of atomically precise armchair graphene nanoribbons". In: *Nano letters* 20.2 (2020), pp. 1124–1130.

[117] Isaac Childres et al. "Raman spectroscopy of graphene and related materials". In: *New developments in photon and materials research* 1 (2013), pp. 1–20.

[118] Hans Kuzmany et al. "Well-defined sub-nanometer graphene ribbons synthesized inside carbon nanotubes". In: *Carbon* 171 (2021), pp. 221–229.

[119] Dan Liu et al. "In-plane breathing and shear modes in low-dimensional nanostructures". In: *Carbon* 157 (2020), pp. 364–370.

[120] David Tománek. *Guide through the nanocarbon jungle*. 2014.

[121] Oliver Braun et al. "Optimized Graphene Electrodes for contacting Graphene Nanoribbons". In: *arXiv preprint arXiv:2102.13033* (2021).

[122] Clement Didiot et al. "Nanopatterning the electronic properties of gold surfaces with self-organized superlattices of metallic nanostructures". In: *Nature nanotechnology* 2.10 (2007), pp. 617–621.

[123] Michele Pizzochero et al. "Quantum electronic transport across 'bite'defects in graphene nanoribbons". In: *2D Materials* 8.3 (2021), p. 035025.

[124] TMG Mohiuddin et al. "Uniaxial strain in graphene by Raman spectroscopy: G peak splitting, Grüneisen parameters, and sample orientation". In: *Physical Review B* 79.20 (2009), p. 205433.

[125] BV Senkovskiy et al. "Making graphene nanoribbons photoluminescent". In: *Nano letters* 17.7 (2017), pp. 4029–4037.

[126] Kenjiro Oura et al. *Surface science: an introduction*. Springer Science & Business Media, 2013.

[127] JKN Sharma and PK Dutta. "Aspects of noise in rotary vacuum pumps". In: *Applied Acoustics* 13.6 (1980), pp. 425–432.

[128] *An introduction to rotary vane vacuum pumps*. 2021. URL: https://www.gardnerdenver.com/en-hu/knowledge-hub/articles/an-introduction-to-rotary-vane-vacuum-pumps.

[129] Lewis D Hall. “Ionic vacuum pumps”. In: *Science* 128.3319 (1958), pp. 279–285.

[130] W Becker. “The turbomolecular pump, its design, operation and theory; calculation of the pumping speed for various gases and their dependence on the forepump”. In: *Vacuum* 16.11 (1966), pp. 625–632.

Universität Basel

Philosophisch-Naturwissenschaftliche Fakultät

Erklärung zur wissenschaftlichen Redlichkeit und Veröffentlichung der Arbeit (beinhaltet Erklärung zu Plagiat und Betrug)

Titel der Arbeit: Edge passivation of vicinal surfaces for controlled growth and substrate transfer of graphene nanoribbons

Name Beurteiler*in: Jung Thomas

Name Student*in: Lüthi Dominik

Matrikelnummer: 15-103-365

Mit meiner Unterschrift erkläre ich, dass mir bei der Abfassung dieser Arbeit nur die darin angegebene Hilfe zuteil wurde und dass ich sie nur mit den in der Arbeit angegebenen Hilfsmitteln verfasst habe. Ich habe sämtliche verwendeten Quellen erwähnt und gemäss anerkannten wissenschaftlichen Regeln zitiert.

Ort, Datum: Dübendorf, 23.11.2021 Student*in: Lüthi Dominik

Wird diese Arbeit veröffentlicht?

☒ Nein

☐ Ja. Mit meiner Unterschrift bestätige ich, dass ich mit einer Veröffentlichung der Arbeit (print/digital) in der Bibliothek, auf der Forschungsdatenbank der Universität Basel und/oder auf dem Dokumentenserver des Departements / des Fachbereichs einverstanden bin. Ebenso bin ich mit dem bibliographischen Nachweis im Katalog SLSP (Swiss Library Service Platform) einverstanden. (nicht Zutreffendes streichen)

Veröffentlichung ab: _____

Ort, Datum: Dübendorf, 23.11.2021 Student*in: ~~Lüthi Dominik~~

Ort, Datum: D'dorf 23.11.2021 Beurteiler*in:

Diese Erklärung ist in die Bachelor-, resp. Masterarbeit einzufügen.